DEPARTMENT OF TRANSPORTATION

Experimental and Computational Investigations of High-Density Asphalt Mixtures

Mihai Marasteanu, Principal Investigator
Civil, Environmental, and Geo- Engineering
University of Minnesota

October 2019

2019-41
Final Report

LRRB
LOCAL ROAD RESEARCH BOARD

To request this document in an alternative format, such as braille or large print, call 651-366-4718 or 1-800-657-3774 (Greater Minnesota) or email your request to ADArequest.dot@state.mn.us. Please request at least one week in advance.

Technical Report Documentation Page

1. Report No.	2.	3. Recipients Accession No.
MN/RC 2019-41		

4. Title and Subtitle	5. Report Date
Experimental and Computational Investigations of High-Density Asphalt Mixtures	October 2019
	6.

7. Author(s)	8. Performing Organization Report No.
Mihai Marasteanu, Jia-Liang Le, Kimberly Hill, Tianhao Yan, Teng Man, Mugurel Turos, Manik Barman, Uma Maheswar Arepalli, Jared Munch	

9. Performing Organization Name and Address	10. Project/Task/Work Unit No.
Civil, Environmental, and Geo- Engineering University of Minnesota - Twin Cities 500 Pillsbury Drive SE, Minneapolis, MN 55455 Civil Engineering University of Minnesota-Duluth 1405 University Dr, Dulth, MN 55812	CTS #2018008
	11. Contract (C) or Grant (G) No. (c) 1003325 (wo) 20

12. Sponsoring Organization Name and Address	13. Type of Report and Period Covered
Local Road Research Board and Minnesota Department of Transportation Office of Research & Innovation 395 John Ireland Boulevard, MS 330 St. Paul, Minnesota 55155-1899	Final Report
	14. Sponsoring Agency Code

15. Supplementary Notes

http:// mndot.gov/research/reports/2019/201941.pdf

16. Abstract (Limit: 250 words)

Compaction of asphalt mixtures represents a critical step in the construction process that significantly affects the performance and durability of asphalt pavements. In this research effort, the compaction process of asphalt mixtures was investigated using a combined experimental and computational approach. The primary goal was to understand the main factors responsible for achieving good density and was triggered by the success of a recently proposed Superpave 5 mix design method. First, a two-scale discrete element method (DEM) model was developed to simulate the compaction process of asphalt mixtures. The computational model was anchored by a fluid dynamics-discrete element model, which is capable of capturing the motion of aggregates in the viscous binder. The model was then calibrated and validated by a series of experiments, which included rheological tests of the binder and a compaction test of the mixture. It was concluded that the compaction process was significantly influenced by the rheological properties of the fine aggregate matrix and by the sphericity of the coarse aggregates. Finally, the mechanical properties of two high-density mixtures were determined and compared with mechanical properties of mixtures used for MnROAD 2017 National road Research Alliance (NRRA) test sections. It was found that the properties of high-density mixtures as a group were not significantly different compared to the properties of conventional mixtures.

17. Document Analysis/Descriptors	18. Availability Statement
Compaction, Asphalt pavements, Asphalt mixtures, Asphalt tests, Superpave	No restrictions. Document available from: National Technical Information Services, Alexandria, Virginia 22312

19. Security Class (this report)	20. Security Class (this page)	21. No. of Pages	22. Price
Unclassified	Unclassified	104	

EXPERIMENTAL AND COMPUTATIONAL INVESTIGATIONS OF HIGH-DENSITY ASPHALT MIXTURES

FINAL REPORT

Prepared by:

Mihai Marasteanu
Jia-Liang Le
Kimberly Hill
Tianhao Yan
Teng Man
Mugurel Turos,
Department of Civil, Environmental, and Geo- Engineering
University of Minnesota Twin Cities

Manik Barman
Uma Maheswar Arepalli
Jared Munch
Department of Civil Engineering
University of Minnesota Duluth

October 2019

Published by:

Minnesota Department of Transportation
Office of Research and Innovation
395 John Ireland Boulevard, MS 330
St. Paul, Minnesota 55155-1899

ACKNOWLEDGMENTS

The authors gratefully acknowledge the financial support provided by the Minnesota Department of Transportation.

The guidance provided by the project's technical advisory panel and, in particular, the technical support provided by project champion Eddie Johnson and the logistical support provided by project coordinator Elizabeth Klemann are acknowledged.

Also acknowledged is Dr. Rebecca S. McDaniel, technical director of the North Central Superpave Center, for sharing the compaction curves for some of the Superpave 5 mixtures used in this study.

TABLE OF CONTENTS

LIST OF FIGURES

LIST OF TABLES

EXECUTIVE SUMMARY

In this research effort, the compaction process of asphalt mixtures was investigated using a combined experimental and computational approach. The main goal was to understand the main factors responsible for achieving good density and was triggered by the success of a recently proposed Superpave 5 asphalt mix design method.

First, a comprehensive literature review was conducted to document previous research efforts on compaction and on numerical modelling of the compaction process. It was found that the current Superpave mix design relies on the assumption that traffic loading provides the final densification to the design air voids and N_{design} should be directly related to expected traffic level. This approach results in asphalt mixtures that have less workability and for which the as-constructed air voids content can exceed 7%, significantly different from the design value of 4%. A number of researchers proposed an in-depth analysis of the compaction curve and suggested other parameters for the mix design process such as the "locking point." However, numerous factors affect the "locking point," such as gradation, type of binder, aggregate type, and size, which makes its use more difficult. It was also found that only a limited number of researchers used discrete element method (DEM) to simulate the compaction process. In all cases, the models used were rather simplistic and the contact laws between particles were not realistic, which resulted in significant deviations of simulation results from experimental data.

In Chapter 3, a two-scale DEM model was developed to simulate the compaction process of asphalt mixtures using a new framework, which only models the coarse aggregates explicitly, while the effect of the fine aggregate matrix (FAM) was modelled by the inter-particle interaction law. In the DEM, the inter-particle contact law followed the Hertzian-Mindlin contact model, and the inter-particle non-contact law was derived from granular physics. Using a preliminary set of compaction experiments, it was shown that the initial model could capture reasonably well the overall compaction process.

In Chapter 4, the model was improved by simulating the behavior of a fine aggregate matrix using the rheology of granular-fluid systems, while simulating the motion of coarse aggregate explicitly using non-spherical composite particles. The fine-scale DEM model was calibrated using the angle of repose experiment, and the model was subsequently used to determine the rheology of FAM. The improved model was then validated by simulating the compaction of three Superpave 5 asphalt mixtures for which experimental data was available. The comparison between experiments and simulations showed that the current DEM simulation with a composite particle model could capture the overall effect of gradation of aggregates on the bulk part of the compaction curves. The deviations observed for the initial portion of the compaction curve were attributed to the interlock between composite particles, which hinders the particle rearrangement. By considering different levels of non-sphericity, it is expected that the simulation results can be improved.

In Chapter 5, asphalt mixture specimens were prepared from loose mix and a number of experiments were conducted to determine if there were significant differences between mechanical properties of high-density mixtures and the corresponding properties of other mixtures. The following experiments were performed: Bending Beam Rheometer (BBR) Creep and Strength, Indirect Tensile (IDT) Creep,

Diametral Dynamic Modulus (E*), Semi-Circular Bending (SCB), Uniaxial Dynamic Modulus (E*), and Flow Number (FN). From the ANOVA and Tukey analysis, no consistent trends in mixture properties were observed. Therefore, it was concluded that the properties of high-density mixtures as a group were not significantly different than the properties of conventional mixtures.

The current research effort indicates that the two-scale DEM model can provide reasonable simulations of asphalt mixture compaction in a gyratory compactor. In particular, the FAM rheology and the level of non-sphericity of the coarse aggregates have a significant effect. However, DEM simulations require significant computational time. Therefore, it appears to be more feasible to perform an extensive experimental campaign on a large set of materials to develop relationships between commonly measured properties and FAM rheology and the shape of coarse aggregates. These relationships can then be used to select the materials and proportions required to develop mix designs for high-density asphalt mixtures.

The link between laboratory compaction and field compaction needs to be further investigated. For example, it is not clear if the field compaction properties of Superpave 5 asphalt mixtures are directly related to the increase in design air voids from the traditional 4% to 5%, the significant reduction in the design number of gyrations, or a combination of both.

CHAPTER 1: INTRODUCTION

1.1 BACKGROUND

Recent studies have shown that the air void content of asphalt mixtures has a significant effect on the durability and long-term performance of asphalt pavements. Asphalt pavements are typically constructed with 7% air voids in the mat and often exceed 10% in longitudinal construction joints. Recent efforts in Indiana have shown that a new mix design method, called Superpave 5, can be used to design mixtures at 5% air voids and to successfully compact them in the field at the same 5% air voids, a significant decrease compared to current practice. At this time, it is unclear why this new method works, and if it is a result of the small increase in design air voids, or of the reduction in the design number of gyrations.

1.2 OBJECTIVE

The objective of this work is to build on the preliminary results of the recently proposed Superpave 5 method and investigate the compaction process of asphalt mixtures through a combined experimental and computational approach. The computational model will be anchored by a fluid dynamics-discrete element model, which is capable of capturing the motion of aggregates in the viscous binder. The model will be calibrated and validated by a series of experiments, which include a rheological test of the binder and a compaction test of the mixture. The experiments will involve typical Superpave mix designs used in Minnesota and modified mix designs that follow the Superpave 5 approach.

1.3 ORGANIZATION OF THE REPORT

First, a comprehensive literature review is conducted in Chapter 2 to summarize the previous research efforts on the compaction of asphalt mixtures and on the numerical modelling of the compaction process. In Chapter 3, a two-scale discrete element method (DEM) model is developed to simulate the compaction process of asphalt mixtures using a new framework, which only models the coarse aggregates explicitly, while the effect of the fine aggregate matrix (FAM) is modelled by the inter-particle interaction law. The proposed computational model is then calibrated and validated using laboratory compaction results of Superpave 5 asphalt mixtures (Chapter 4). Finally, in Chapter 5, the mechanical properties of high-density mixtures are tested and compared with corresponding properties of other mixtures used to construct the MnROAD 2017 NRRA test sections. Chapter 6 consists of a summary of the work followed by conclusions and recommendations.

CHAPTER 2: LITERATURE REVIEW

In this chapter, a comprehensive review of the development of the design process of asphalt mixtures and of field and laboratory compaction is performed. Past research documenting the effect of air voids on properties of asphalt mixtures and numerical simulation of asphalt mixture compaction is also included in this literature review.

2.1 HISTORY OF LABORATORY COMPACTION

The aim of laboratory compaction methods is to simulate the field compaction conditions. Methods that produce laboratory specimens similar to field compacted samples are desired. Throughout the asphalt mixture design history, a variety of compaction methods were developed and used in different mix design methods, including impact hammer, kneading, gyratory shear, simulated rolling and vibration etc. Kneading compaction was used for the Hveem design method, which was developed to more closely simulate the compaction produced by rollers in the field (Vallerga & Lovering, 1985). Impact compaction method was used in the Marshall Mixture design method to prepare samples. Certain numbers (35, 50 and 75) of blows on each face are required for impact compaction to match the different traffic compaction levels (White 1985). During the 1980s, rutting became more prevalent in United States. Many engineers attributed this to the impact compaction used in Marshall Mixture design method, due to the fact that impact compaction could not satisfactorily reproduce the density in the field (Harman et al., 2002). This issue was later addressed as part of the Strategic Highway Research Program (SHRP). This unique research program started in 1987 and was completed in 1992 and had a budget of $150 million. Its main objectives were to identify and define properties of asphalt binders, aggregate, and hot mix asphalt that influence pavement performance and to develop test methods for performance-based specifications. The Superpave mixture design method was one of the products of SHRP.

Just before the start of the SHRP program, the National Cooperative Highway Research Program (NCHRP) initiated a study called the Asphalt-Aggregate Mixture Analysis System (AAMAS). The main objective of this research was to evaluate different laboratory compaction methods and to make recommendation to SHRP research team. The methods investigated included:

- Marshall compaction (mechanical, static-base, flat face)
- Marshall compaction (mechanical, rotating base, slanted face)
- Marshall compaction (hand compaction)
- Kneading compactor
- Vibratory hammer
- Simulated rolling wheel (quarter circle)
- Vibrating, kneading compactor

• Gyratory compactor (Texas 4-inch gyratory)

The results showed that gyratory compaction mimics field compaction best among all methods investigated, because it achieved the densities encountered in the field, and produce samples with similar mechanical properties as field samples (McDaniel et al., 2011). At that time, several types of gyratory compactors (Texas gyratory compactor, Corps of Engineers gyratory test machine and French Gyratory Compactor) were available. The question was which gyratory compactor to specify.

The development of gyration compaction method can be traced back to 1939, when the Texas Department of Highways initiated a study on the design and control of asphalt mixtures. The main task of this study was to make a selection from different laboratory compaction methods. Two criteria were used: "first, the compactor should achieve the final density of the pavement after being subjected to traffic, and second, aggregate break down should approximate the break down in the field" (McDaniel et al., 2011). In the end, the Manual Texas Gyratory Compactor was selected.

Several years later, in 1950s, a mechanized compactor replaced the old manual one and Texas Highway Department standardized its use in specifications. In the late 1950s, John McRae of the U.S. Army Corps of Engineers developed the Corps of Engineers gyratory test machine (GTM), based on the principle of gyratory compaction. Different from Texas Gyratory Compactor, GTM only held two points across the diameter of the specimen which allowed for the angle of gyration to vary during compaction, and GTM could measure mixture response (compaction pressure and specimen height) during compaction.

Another type of gyratory compactor is the French Gyratory Compactor (FGC). It was developed based on Texas Gyratory Compactor and GTM, by the Laboratoire Central des Ponts et Chausées (LCPC) in France. By monitoring specimen height, density was tracked during compaction. The relationship of density to the log of the gyrations number was found to be nearly linear. (Moutier, 1974)

In 1991, after comparing and contrasting different gyratory compactors, SHRP decided to use the principles of operation of the LCPC compactor, but needed to evaluate and make changes to it. After many discussions, the following changes were made to the LCPC gyratory compactor:

• Vertical consolidation pressure of 600 KPa

• Fixed angle of gyration of 1.25°,

• Speed of gyration of 30 rpm

During the SHRP research program, whether the Rolling Wheel Compaction was better than the Superpave gyratory compactor was intensively debated. Professor Carl Monismith advocated for the adoption of the Rolling Wheel Compaction over the gyratory. He pointed out that specimens from gyratory compactor were non-uniform in both radial and vertical direction. However, the Rolling Wheel Compactor was considered impractical as a means of laboratory compaction method (equipment is large and expensive), and further evaluation showed that the gyratory compactor was better than the

Rolling Wheel Compactor in terms of producing laboratory specimens similar to field samples. (McDaniel et al., 2011)

After SHRP program, many follow-up studies were performed to investigate the effects of the internal variables of SGC (gyration angle, pressure and specimen height). It was found that gyration angle had a significant influence on the percentage of air voids: a change in the gyration angle of 0.02 degree caused a change in air void ratio of approximately 0.8% (Harman et al., 2002). It was also found that the internal gyration angle of different SGC were not uniform even though they had the same external gyration angle (Harman et al., 2002). Some efforts were made to address this issue, using e.g., the dynamic angle validation (DAV) and the rapid angle measurement (RAM) devices (Anderson et al., 2006).

A number of studies showed that for the same percentage of air voids, mechanical properties of asphalt mixtures are significantly affected by the air voids distribution. Tashman et al. (2000) recommended changing the gyration angle to 1.5 degree and the specimen height to 50 ~ 75mm. Peterson et al. (2003) argued that current SGC protocol (gyration angle = 1.25 degree, specimen height = 135mm) produced specimens greatly different from field cores in mechanical properties, and by changing the gyration angle to 1.5 degree and the specimen height to 50 ~ 75mm, the specimens simulated better the mechanical properties of pavement cores. However, data in these studies was limited to certain types of asphalt mixtures and mechanical properties. More validation work was recommended by the authors. Recently, Georgiou et al. (2016) recommended changing the gyration angle to 1.45 degree to better simulate the internal structure of field cores.

2.2 EMERGENCE OF N_{DESIGN}

According to Blankenship et.al. (1994), “Pavements are compacted in two stages: during construction and as they are trafficked. Asphalt mixtures are initially compacted to about 8% air voids during construction. After construction, traffic loads densify the asphalt layer, especially during hot months, until it reaches ultimate density. The properties of the asphalt and aggregate based on long-term densification of a pavement must be taken into account”. Thus, traffic compaction should be considered in laboratory compaction. It should be able to simulate final density at the design traffic level compaction.

In Marshall mix design, the number of compaction blows reflect the traffic level: 35, 50 and 75 represent low, medium and high traffic level, respectively. In Superpave mix design, the concept of N_{design} was first proposed to relate the traffic level to the number of gyrations in gyratory compaction (Blankenship, 1993). It is defined as the number of gyrations (at a specific pressure) at which the compacted sample can mimic the two levels of compaction: (a) construction compaction and (b) traffic compaction. The volumetric design is conducted at N_{design} gyrations.

Studies performed by LCPC using FGC showed that density is proportional to the logarithm of the number of gyrations (Moutier, 1974). Other studies also showed that the asphalt layer under traffic increases in density linearly with the logarithm of the number of traffic passes until it reaches its

ultimate density (Blankenship et al., 1994). Therefore, a linear relation was hypothesized between the logarithm of gyration and the logarithm of traffic level (represented by ESALs) (Blankenship et al., 1994).

To obtain values for N_{design}, a study called "Gyratory Compaction Characteristics: Relation to Service Densities of Asphalt Mixtures" was conducted (Blankenship, 1993). Fifteen pavement sites were chosen, that included 3 traffic levels and three climatic regions. The selected pavements were more than 12 years old, so that they were more likely to be densified to ultimate density. The density after construction (when ESALs=0) was assumed to be 92% of maximum theoretical specific gravity ($\%G_{mm}$). In the experiment, the density of the cores were measured. Then aged asphalt was extracted and salvaged aggregate was remixed with AC-20 grade asphalt cement and compacted. Finally, the compaction curves were achieved. The number of gyrations that matched the in-place density was back-calculated. Based on the experiment, the first version of N_{design} table for three climates and seven traffic levels was developed. Later on, the SHRP researchers expanded this table to four climates.

2.3 VALIDATION AND MODIFICATION OF N_{DESIGN}

After SHRP, a number of studies were conducted to further validation and modify N_{design} table. NCHRP Project 9-9, conducted by NCAT, aimed to develop guidelines for gyratory compaction. Experimental results showed that optimum asphalt content, VMA, and VFA all decreased with increasing N_{design}, and that coarse-graded mixtures were more sensitive than the fine-graded mixtures (Brown et al., 1998). The authors also noted that compacting samples to $N_{maximum}$ and back-calculating the volumetric properties at N_{design} could results in errors of up to 0.8 percent air voids. Therefore, the report recommended that, to obtain the volumetric properties, the samples should be compacted to N_{design} rather than to $N_{maximum}$. In addition, the effect of the climate could be taken into account by simply using different performance grades of binder for the corresponding climate temperatures, so N_{design} table was reduced to be only related to traffic level. The revised table is shown in Table 2.1 (Brown and Buchanan, 1999)

Table 2.1 Revised N_{design} table proposed by NCHRP Project 9-9 (Brown and Buchanan, 1999)

Design Traffic level (million ESALs)	Gyration Levels			% G_{mm} at $N_{initial}$	% G_{mm} at $N_{maximum}$
	$N_{initial}$	N_{design}	$N_{maximum}$		
<0.1	6	50	74	<91.5	<98.0
0.1 to <1.0	7	70	107	<90.5	
1.0 to <30.0	8	100	158	<89.0	
>30.0	9	130	212	<89.0	

The N_{design} II experiment was another major effort to verify N_{design} (Anderson et.al, 2000). In this investigation, N_{design} was evaluated based on the sensitivity of mixture stiffness to the change in N_{design}. Results showed that the stiffness decreased with the N_{design}, especially when the air void ratio ranged from 3 to 6%, with an increase in air void ratio from 4 to 5% resulting in a 20% decrease in stiffness. Based on these results, a new table was recommended, as shown in Table 2.2. This new table was also adopted by AASHTO.

Table 2.2 Superpave compaction effort (AASHTO, 2005)

Design Traffic level (million ESALs)	Compaction Parameter		
	$N_{initial}$	N_{design}	$N_{maximum}$
<0.3	6	50	75
0.3 to <3.0	7	75	115
3.0 to <30.0	8	100	160
>30.0	9	125	205

In 2007, a research project called "Verification of Gyration Levels in the N_{design} Table" was conducted to verify the N_{design} levels in the field (Prowell & Brown, 2007). Samples were chosen from 40 field projects in 16 different states, which included a wide range of traffic levels, binder grades, aggregate type and gradation. The results showed that the majority of the 40 projects (55%) had insufficient as-constructed densities (less than 92% of G_{mm}), and the N_{design} levels in AASHTO (see Table 2.2) were higher than needed to match the in-place density, so they recommended to reduce the N-design level in AASHTO. The recommended N_{design} are shown in Table 2.3. Also, it was recommended to remove $N_{initial}$ and $N_{maximum}$ from the AASHTO table based on the fact that all 40 field project samples had excellent resistance to rutting based on evaluation of the original mix design data (Prowell & Brown, 2007).

Table 2.3 Proposed N_{design} table by Prowell & Brown (2007)

20-Year Design Traffic level (million ESALs)	2-Year Design Traffic level (million ESALs)	N_{design} for binders <PG 76-XX	N_{design} for binders <PG 76-XX or mixes >100 mm from surface
<0.3	<0.03	50	NA
0.3 to <3.0	0.03 to <0.23	65	50
3.0 to <10.0	0.23 to <0.925	80	65
10 to <30.0	0.925 to <2.5	80	65
>30	>2.5	100	80

Although N_{design} is an important parameter in Superpave Mixture design, the validity of the assumption used has been widely debated. The assumed linear relationship between density and the log of traffic level was questioned by a number of researchers. Stroup-Gardiner et al. (1997) found that the relationship was much more complex than the hypothesized linear relation. They noted that the lower lifts were less compacted by the traffic after construction than the upper lifts. Also, they pointed out that, for high traffic volume roads, the air void ratio in the upper lifts of pavement shows an upwards trend with the increase of ESALs. Moisture damage was considered as a possible reason since moisture damage can cause material loss in the upper lifts. The study showed that traffic compacted different lifts differently, and it could even reduce the density of upper lifts at high traffic levels. Other authors found that the effect of traffic densification was limited (Harmelink et al. 2007, Brown et al., 1996).

The assumption that the density of samples increases linearly with the log of the number of gyration in the SGC was also questioned. Vavrik and Carpenter (1998) pointed out that the linear relationship holds true in the initial part of the densification curve, but error develops as the material densifies. They believed that the "Locking Point" is the upper boundary for the linear relationship; after that excessive aggregate break down happens and the relationship becomes nonlinear. Thus, they concluded that using the data beyond "Locking Point" will cause higher error in determining the N_{design}.

The "locking point" is defined as the number of gyration at which the aggregate skeleton locks together and further compaction results in aggregate degradation, and it is determined as "the first gyration in the first occurrence of three gyrations of the same height preceded by two sets of two gyrations with the same height" (Pine, 1997, Vavrik & Carpenter, 1998). For some mixtures, such as Stone Matrix Asphalt (SMA), the "locking point" gyration number is recommended instead of N_{design} (Xie et al., 2005, West et al., 2001). "Locking Point" is also considered as an index indicating how compactable the material is (Leiva & West, 2008). Different materials have different compactability levels, and therefore, the "Locking Point" can be used to determine the maximum roller passes before the material breaks down (Prowell, 2007). The advantage of "Locking point" over N_{design} is that it considers the difference between materials: different types of mixtures have different "Locking Point" gyration numbers. However, numerous factors affect the "locking point", such as gradation, type of binder, aggregate type and size, which makes its use more difficult.

2.4 EFFECT OF AIR-VOID RATIO ON PROPERTIES OF HMA

The aim of compaction is to transform the mixture from its very loose state into a more coherent mass, so that it can carry traffic loads. Another reason for compaction is to reduce the air voids in the mixture to make it watertight and impermeable to air. If the air void ratio is too low the pavement will tend to bleed or rut. If it is too high, the pavement will tend to have poor durability. According to Prowell & Brown (2007), there should be an optimum air void ratio that correlates with the best combination of strength and durability.

An experimental study on the effects of density (air void ratio) on the performance of HMA was conducted by Del and Haddock (2006) at Purdue University. The results showed that, in terms of permeability, the critical value of air void ratio is 7%. Below it, the mixtures have low permeability, but above it, permeability increases exponentially with air void ratio. Dynamic modulus and initial stiffness decrease with air void ratio, which predicts high rutting resistance of high-density mixture. Air void ratio was also shown to have an indirect negative effect on fatigue property through the moisture content of the mixture, because higher air void ratio can greatly increase the moisture content that has a significant negative effect on fatigue resistance. According to the researchers, all mixture tests appeared to benefit from higher density, so they recommended that mixtures should be designed and constructed to a lower air void content.

Washington State Department of Transportation (MSDOT) studied the effect of air void on pavements performance in Washington State (Willoughby and Mahoney, 2007). The study included a literature review, a questionnaire survey and data analysis of the Washington State Pavement Management

System (WSPMS). All three sources of information confirmed that the air void content significantly affects pavement performance. From experience, each 1% increase in air void (over the base of 7% of air voids ratio) results in about 10% loss in pavement service life.

The relationship between air voids, lift thickness, and permeability in HMA pavement was investigated in NCHRP report 531 (Brown et al., 2004). The authors showed that permeability was not only influenced by in-place void content but also by coarse aggregate ratio. Coarse-graded Superpave mixes can be excessively permeable even when in-place air voids are less than 8%. Gap-graded mixtures, such as SMA, tend to become highly permeable when air voids are above approximately 6%. High in-place voids are generally caused by inadequate compaction, so more emphasis must be placed on obtaining adequate in-place density. In addition, higher lift thickness/NMAS ratios was found beneficial for in-place compaction and reducing air void levels, because thinner layers cools more rapidly than thicker layers. As a result, it was recommended that lift thickness/NMAS ratio should be at least three for fine-graded mixes and at least four for coarse-graded and SMA mixes.

In a study performed in Indiana, the risk of low air voids in asphalt mixture was evaluated (McDaniel and Levenberg, 2013). Excessive binder and fines content were found as the main reasons causing low air void content. These mixtures experienced significant rutting in both surface and intermediate layers. Mixtures with excessive binder content rutted faster than those with excessive fines. The research suggested that removal should be considered for mixtures with air voids below 2.75%.

Recently, X-ray Computed Tomography (XCT) and Digital Image Processing (DIP) methods were used to investigate the effect of air void distribution on mechanical properties of HMA. Using these methods, Kassem et.al (2011) studied the effect of air voids distribution on fatigue cracking resistance of HMA. They found that specimens with more uniform air void distribution had less variability in terms of fatigue cracking resistance; specimens with high air void ratio were sensitive to the moisture damage. Using XCT and DIP methods, Hu et.al (2016) investigated the fatigue damage of HMA with different air void distributions. It was found that the air-void ratio of asphalt mixtures increased after fatigue damage; decreasing the complexity (Fractal dimension) of air-voids can effectively reduce the fatigue damage of asphalt mixture.

2.5 LOW-AIR-VOID MIXTURE DESIGN

Since the SHRP program, rutting distress has been reduced to a large degree. However, durability has remained the main issue which affects the service life of asphalt pavement. The decreased durability is mainly a result of the relatively high as-constructed air void ratio (8%~10%). Thus, controlling the air void ratio to improve durability represents the main concern of mixture design.

Low air void ratio is often related to poor rutting resistance. However, efforts are being made to find out possible ways to reduce the air void ratio, while keeping the rutting resistance unaffected. A project called “Superpave 5” was proposed in Indiana in which the mixtures are designed at an air void ratio of 5% and are expected to be compacted to the same air void level in the field. The increase in the as-constructed density can greatly improve the durability of the pavements. The 5% as-constructed air void

ratio was achieved by adjusting the gradation, without changing the effective binder content. In this study, standard mixtures were designed with N_{design}=100, target air void ratio = 4% and target as-constructed air void ratio = 7%. Then, the mixtures were redesigned with the target as-constructed air void ratio = 5% and the gyration numbers were reduced to 30, 50 and 70, respectively, to only simulate the construction compaction. Dynamic modulus and flow number of the standard and the redesigned mixtures were compared. Results showed that the redesigned mixtures had similar dynamic modulus and flow number values as standard mixtures. Since low as-constructed air void improves the durability, redesigned mixtures were believed to outperform the standard mixture when constructed in the field.

Another method to improve durability was proposed by Wisconsin DOT (WisDOT). The method called "regressed air voids" starts with designing a mix for 4.0% air voids, which is the current WisDOT practice, and then predicts the amount of additional virgin asphalt binder needed to obtain 3.5% or 3.0% air voids" (WHRP, 2016). The binder content increases approximately by 0.4% from original mix design. Experiments will be conducted to verify the effects of this method on pavement performance.

2.6 CONTINUUM MODEL FOR THE COMPACTION OF ASPHALT MIXTURE

H. L. ter Huerne (2000; 2004) used critical state model from soil mechanics to simulate the field compaction process of the asphalt mixture. To consider both the large deformation during compaction process which comes from the fluid-like properties of hot mix asphalt, and the solid properties of the asphalt mixture, the arbitrary Lagrangian Eulerian (ALE) formulation was used. The contact law between a roller and the asphalt mixture was simulated in both normal direction and tangential direction of the pavement surface. In normal direction, the contact was represented as a spring and a dashpot in parallel, while in tangential direction, the contact was simulated only using a spring. The model can give plausible stress, strain and deformation patterns, and reasonable compaction curve of the compaction process. Since this model was derived from soil mechanics, it can capture the slippage between particles during the compaction process. However, based on the critical state theory, only elastic and plastic deformation were taken into consideration. The viscous effect of the asphalt binder was neglected.

Guler et al. (Guler, Bosscher, and Plesha 2004) employed a porous elasto-plastic compaction model to simulate the laboratory gyratory compaction process using a finite element software. A pressure dependent porous material with elastoplastic matrix was assumed to contract under a prescribed compaction pressure induced by the gyratory compactor. Plastic strains were integrated from an incremental elastoplastic constitutive equation by forward difference method. The constant parameters of the model were calibrated using Levenberg-Marquardt nonlinear parameter estimation algorithm. This model can predict well the gyratory compaction process, but neglecting the viscous effect makes this model questionable. Also, treating the mixture as a solid body neglects the fluid effect brought by the asphalt binder. Thus, this model is a rate independent model, which is different from the real compaction process which is dependent on the rate of loading. Wang et al. (2006) used the same model to simulate the field compaction process. Their research showed that this model could also qualitatively simulate the field compaction process, since no model calibration was conducted. However, no comparisons between field compactions and simulations were investigated.

Xia and Chi (Xia and Chi 2008) tried to predict the asphalt pavement compaction during field compaction process using a viscoplastic foam model. They extended the rate-independent crushable foam plasticity model to a viscoplastic model with volumetric hardening, so that the viscous effect could be taken into consideration. Large deformation theory was also used in this process, which can, as the author mentioned, be used in predicting the spatial density distribution induced by the compactor.

Koneru, Masad and colleagues (Koneru 2006; Koneru 2010; Masad et al. 2010) developed a thermodynamics-based compressible viscoelastic model to simulate the compaction process. The model was changed and developed from models they originally developed to simulate the permanent deformation during the service time of asphalt pavement. Both field compaction and laboratory compaction were simulated using this model. Several constants in this model, which are related to the shear properties and viscous properties, were given as the key parameter being fitted in the experiments. In this model, no anisotropic constitutive relationships were considered.

2.7 DISCRETE ELEMENT MODEL (DEM) FOR THE COMPACTION OF ASPHALT MIXTURE

Wang et al. (Wang et al. 2006) qualitatively simulated the field compaction using DEM in PFC3D. A simple contact model was used to represent the inter-particle contacts and particle-roller contacts. The effect given by different shapes of particles and particle contact properties were studied qualitatively. The temperature effect was also taken into consideration by changing the stiffness of the inter-particle contact model. Overall, this model is a simple DEM, which cannot predict the compaction curve during compaction process. The contact laws between particles and between particles and the roller are Hertzian contact law, which are not realistic for the case of asphalt mixture. Also, no experiments were performed for considering the temperature effects.

Chen and his colleagues (Chen 2011; Chen, Huang, and Shu 2012; Chen et al. 2015) developed a more realistic DEM model to simulate both the field compaction and gyratory compaction. The contact law was set to be Burgers' model, which contains a Maxwell section and a Kelvin section connected in series. The model was simulated using YADE DEM code. In this model, only coarse aggregates were considered. The effects of fine aggregates and binder was represented by the contact law between coarse aggregates. Real aggregates gradation was used, but all the aggregates were considered as spheres. The contact law was calibrated using experiments on the mastic. However, the predictions for gyratory compaction and vibration compaction differed significantly from the experimental data. Their simulation for asphalt pavement analyzer (APA) linear kneading compaction looked slightly better, but still, the compaction rate and ultimate air void ratio cannot be captured. The deviations of simulations from experimental data came from the unrealistic contact law which is derived from solid experiments of mastic. Also, the volume of fine aggregates and the asphalt binder was not taken into consideration, thus, the ultimate air void ratio from the experiments cannot be captured from these simulations.

2.8 GRANULAR COMPACTION DUE TO SHEARING

Researchers in physics communities have also investigated the compaction behavior of granular assemblies. In the last decades, a number of studies investigated the compaction behavior of granular

assemblies under tapping or shaking excitation, vibration or cyclic shearing. The microscopic analyses of granular materials during compaction induced by tapping and shearing have been studied (Anita Mehta and Barker 1994; Knight et al. 1995; Nicolas, Duru, and Pouliquen 2000). The relationship between collective microscopic structure and the compaction dynamics has been explained (A Mehta, Barker, and Luck 2004; Pouliquen, Belzons, and Nicolas 2003). Several equations describing the compaction behavior were developed based on multiple time scale assumption (Barker and Mehta 1993; Philippe and Bideau 2002; Knight et al. 1995). Most of the researches focused on the compaction induced by tapping excitation, while some other researches focused on the compaction due to shearing excitation. Both types of experiments were conducted carefully to measure the evolution of solid volume fraction (the ratio between solid volume and the total volume of the granular material) during experiments and track the motion of certain particles. Furthermore, experiments related to the compaction of wet granular assemblies (Fiscina et al. 2010) were also investigated.

However, based on our own interest, only the compaction due to shearing might be helpful to our research on the compaction of asphalt mixture, since during compaction, the asphalt mixture is subjected to constant pressure and most importantly shear stresses. The shearing granular compaction investigated by physicists is cyclic shearing. Not many researchers investigated this topic. Nicolas et al. in France performed compaction tests using cyclic shearing (Nicolas, Duru, and Pouliquen 2000; Luding, Nicolas, and Pouliquen 2000). A sketch of the experiment setup is shown in Figure 2.1. In this experiment, beads of diameter 2.97 ± 0.06 mm were put into a parallelepiped shear cell. The granular packing was confined by the top plate connected to a vertical displacement rail with position sensor to measure the current height of the packing. During the experiments, the bottom plate was moved horizontally to give the granular packing cyclic shearing excitation. In the experiments, all the beads were coated with silicon oil to prevent them from surface deterioration during long-time experiments. The authors stated that the same quantitative results were observed with and without lubrication, but no proof was given to verify their statement. In the other experiment, based on the same experiment setup, all the beads were immersed in a mixture of turpentine and methylnaphthalene so that the packing was transparent and the colored beads could be tracked during compaction process. Yet, no experiments were given to show the influence of adding lubrication or other types of liquids.

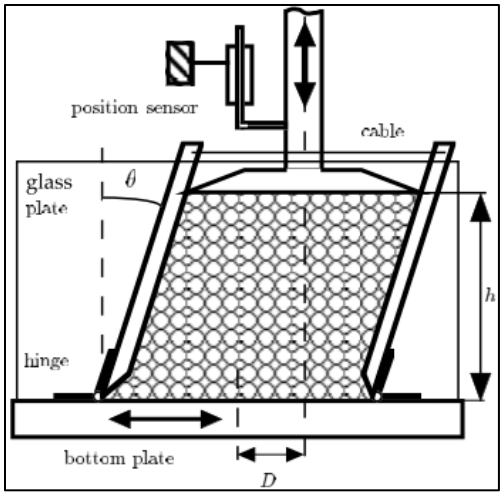

Figure 2.1 Schematic of the shear cell and position sensor. *D* is the maximum horizontal displacement of the bottom plate. *h* is the height of the packing tracked by the position sensor.

During the experiment, the inclination angle ϑ was tracked and considered as important as the tapping intensity in the compaction due to tapping or shaking. Different inclination angles were tested in the experiments. The authors also stated that changing the velocity of bottom plate and changing the pressure did not affect any of the measurement, but no experimental results were given to prove this. They ran the test for different shearing amplitudes: 2.7 degree, 5.4 degree, and 10.7 degree, and obtained the compaction results. First, they ran the same experiment several times, and found that the final volume fraction for different realization can vary significantly (about 10%). Secondly, by comparing with classical fittings for granular compaction due to tapping or shaking, no reasonable agreement with both the short and long-term behavior could be found. Besides, Mehta and Barker's two exponential function and the stretched exponential function also do not offer more convincing agreements. Also, cyclic shearing can achieve larger volume fraction than tapping excitation.

The effects of a sudden change of shearing amplitude were also studied in the experiments (Nicolas, Duru, and Pouliquen 2000). In the experiment, the shearing inclination angle was first set at 2.7 degree, then was changed to 10.7 degree suddenly at 5000 cycles, and then was changed to 2.7 degree again at 10000 cycles. They found that when the angle was changed suddenly from 2.7 degree to 10.7 degree, there was a sudden decrease of solid volume fraction on the compaction curve. Then the solid volume fraction increased steadily. This shows the memory effect during compaction, and knowing the solid volume fraction of the packing is not enough to predict the evolution of the system because the loading history of the granular packing is also important for telling the compaction behavior. Furthermore, when they suddenly decreased the inclination angle from 10.7 degree to 2.7 degree, there was also a "jump" in the compaction curve. They also stated that the magnitude of the discontinuity during the sudden change of inclination angle (the "jump") is influenced by the history of packing, as well as the amount of angle has been changed. The jump of volume fraction usually decreases with the increase of the age of packing. More importantly, the jump of volume fraction is simply proportional and opposite to the amount of angle change.

The authors also studied the irreversible and reversible part of the compaction process continuously changing inclination angle during compaction. They showed that the reversible part is a straight line parallel to $-\alpha\vartheta$. The authors also tend to believe that the shearing compaction contains two parts: one is a slow and continuous compaction when the shear amplitude is constant, and the other is a rapid response when a change in shear amplitude is imposed.

However, these studies mainly focus on the compaction behavior for different shearing amplitude, and shear rate and shear stress, which are important to the compaction of asphalt mixture, were not considered in these studies. Besides, the microscopic behavior, statistical mechanics of complex system, and the analogues between the thermodynamics of granular compaction and the thermodynamics of other non-equilibrium system, such as glasses, are the main topics in the studies of granular assemblies.

2.9 WET GRANULAR COMPACTION

Researchers at the University of Liege also studied the compaction behavior of wet granular assemblies, during which the influence of viscosity and particle-particle interactions were investigated (Fiscina et al. 2010; Vandewalle et al. 2012; Lumay et al. 2013). The existence of liquid bridges did not influence the qualitative behavior of the compaction process, but a decrease of both initial volume fraction and final volume fraction was observed as a function of surface tension of different liquids used during the experiments. This was due to the increase of capillary force when surface tension, γ, was increased. The initial volume fraction was obtained as a function of surface tension as follows

$$\eta_0 = \frac{\eta_*}{1 + a\left[1 - \exp\left(-\gamma/\gamma_0\right)\right]}$$

where η_0 is the initial volume fraction, η_* is the packing fraction, a and γ_0 are fitting parameters. Also the relation between relaxation time scale and the surface tension were analyzed, and a model developed from energetic approach was proposed to fit this relation.

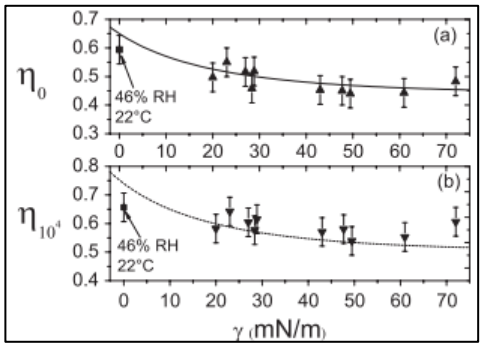

Figure 2.2 Initial volume fraction and final volume fraction plotted against the surface tension of the interstitial liquid in the granular system. (Fiscina et al. 2010)

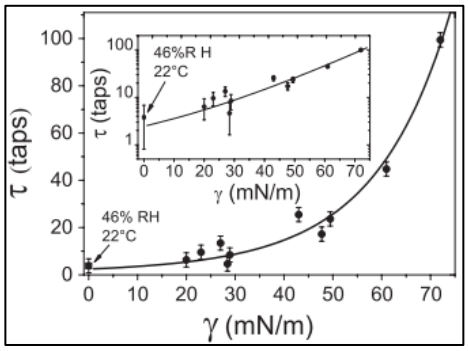

Figure 2.3 Relation between relaxation time scale in inverse logarithmic model and the surface tension of the liquid in the experiment. (Fiscina et al. 2010)

Another research related to the influence of humidity on the behavior of granular compaction was also conducted (Vandewalle et al. 2012). During this experiment, the humidity was controlled for different experiments. The relationship between the relative humidity (RH) and volume fraction was analyzed. The compaction curve looked similar to the phenomenological Kohlrausch-Williams-Watts (KWW) law.

$$\frac{\eta-\eta_0}{\eta_\infty-\eta_0}=1-\exp\left[-\left(t/\tau\right)^{\delta}\right]$$

where τ is fitting parameter which can be seen as the relaxation time scale, δ is the stretching exponents which was fitted according to the experiments.

The authors used energetic approach to analyze the compaction process. They believed that for dry granular packing, friction can introduce attractive forces between particles, and the electrical charges represented a barrier for local reorganizations. For wet granular assemblies, the bridges formed by the liquid between particles can also been regarded as an energetic barrier for local reorganizations. Further, as the moisture content increases, the electrical charges between particles disappear exponentially and liquid bridges can form by capillary condensation (Vandewalle et al. 2012). Therefore, both triboelectric and capillary effects influenced the granular assemblies.

The effect of grain sizes was also investigated (Lumay et al. 2013). It was found that when the grain size is getting larger, the ratio between weight and the cohesive forces increases. Therefore, the cohesive forces could be unable to stabilize a loose packing (Lumay et al. 2013). They showed that the cohesive forces play an important role for grain size below 50 μm.

Li et al. (2014) studied the structural evolution of wet granular compaction using X-ray. Distribution of free volume, contact number, pair correlation and high-order angular distribution functions were analyzed based on the experimental data. A large amount of locally favored structures with fivefold symmetry were observed when the packing is wet and short range attractive interactions exist. The similarity between wet granular packing and colloidal gels was proposed, while dry granular compaction showed no such similarity.

Vibration induced compaction of granular suspensions was studied by Kiesgen de Richter et al. (2015). Experiments, similar to the classical experiments conducted at the University of Chicago by Knight et al (Knight et al. 1995), were conducted and the images of compaction were captured during compaction processes. The experimental results showed that the whole compaction process could be divided into two stages: one is a fast stage corresponding to a rising compaction front propagated through the granular suspension, the other is a slow stage where the packing compacts slowly and homogeneously. The compaction curve was modelled using stretched exponential law, where stretching exponential for two stages were roughly 2 and 0.45, respectively. The influence of interstitial fluid was also analyzed. The authors assumed that the compaction of granular suspension is governed by the competition between the granular pressure of the packing, $P = \Delta\rho g\phi(t)h(t)$, and the lubrication stress, $\sigma_{lub} \propto \eta_f A\omega/D$. Here, Δρ is the density ratio between beads and fluid, η_f is the viscosity of the fluid, and $A\omega$ is the vibration liftoff velocity. The relation between relaxation time and the lubrication Peclet number Pe_{lub} =

σ_{lub}/P was investigated. They found that neither the tapping intensity Γ nor the vibration liftoff velocity were the appropriate parameters which control the relaxation time scale, while the relaxation time can be written as a function of Pe_{lub}. Also, the volume fraction at the transition point, φ_c, increased linearly with the relaxation time. Proportional relation can be constructed between φ_c and $\tau_c P/\eta_f$ (Kiesgen de Richter et al., 2015).

CHAPTER 3: DEVELOPMENT OF DISCRETE COMPUTATIONAL MODEL

3.1 INTRODUCTION

The mechanical properties and durability of asphalt mixture are an important area of research in civil engineering as an understanding to how to maximize compaction efficiency would result in significant cost reduction in related areas of infrastructure development and maintenance. While substantial progress has been made in the last few decades in building effective and realistic models for simulating the mechanical properties of asphalt mixture, little is known about the physics behind the compaction process of asphalt mixture. The compaction process, which can dramatically influence the porosity of the compacted asphalt mixture, is crucial to the mechanical behavior and durability of the asphalt mixture in service. Under-compaction of asphalt mixture is linked to poor cracking resistance to traffic and environmental stresses, and reduced durability due to increased aging and moisture susceptibility. Freeze-thaw cycles in cracked asphalt pavements accelerate this deterioration process. Thus, predicting the compaction behavior represents a critical element in improving asphalt mixtures design.

To predict the compaction behavior of hot asphalt mixtures, both continuum models and discrete element models (DEM) have been used. Guler et al. (2004) used a modified continuum porous media model to simulate the deformation of hot asphalt mixture during compaction. Koneru *et al*. (Koneru 2010; Koneru 2006; Masad et al. 2010) derived a visco-plastic model from the basic of thermodynamics, which can give relatively accurate prediction of the compaction process of the asphalt mixture. However, continuum models cannot capture the mechanism by which air void content decreased during the compaction process. In addition, in continuum model it is difficult to model explicitly the influence of the size distribution and shape of aggregates as well as the rheological properties of the binder and mastic.

To overcome these difficulties, Discrete Element Models (DEM) were proposed to predict the compaction behavior of asphalt mixtures. The main advantage of DEM is that it can explicitly model the microstructural features of the asphalt mixtures, which allows us to capture the physical mechanisms of the compaction process. Wang *et al*. (Wang et al. 2006) simulated the field compaction process by using Hertzian contact law in a commercially available DEM software (PFC3D). Different inter-particle collisional stiffnesses, particle sizes, and particle shapes, were considered. However, without model calibration and comparison with the experiments, only qualitative results were possible. Chen *et al*. (Chen 2011; Chen et al. 2015) simulated the compaction processes of Superpave gyratory compactor and a vibratory compactor using DEM by using Burger's contact law in an open-source DEM code (YADE), and through the comparison with experimental results it was demonstrated that the DEM is capable of simulating the compaction behavior of asphalt mixtures.

Explicit modeling of microstructural features of asphalt mixtures leads to high computational demand of DEM, especially when one wants to model the fine particles. The inter-particle interaction law is usually determined by optimum fitting of the experimental results, where the fitting procedure involves a

nonlinear optimization process. This optimization process could be challenging given the high computation effort required for each trial DEM simulation.

To address these issues, we developed a two-scale DEM model for simulating the compaction process of asphalt mixtures based on the concept of fine aggregate mixtures (FAM). In the DEM, only the coarse aggregates are explicitly modeled, and the inter-particle interaction is characterized by a subscale DEM simulation of the FAM. Preliminary compaction experiments on graphite nano-platelets (GNP) modified asphalt mixtures are performed to examine the performance of the proposed DEM framework.

3.2 FORMULATION OF A SIMPLE INTER-PARTICLE CONTACT LAW

The key ingredient of the DEM is the inter-particle contact law. For DEM simulations of the compaction process of asphalt mixtures, we consider two types of interactions, namely the inter-particle contact force, and the lubrication force. The formulation of the constitutive behavior of these two types of interactions is described in Figure 3.1.

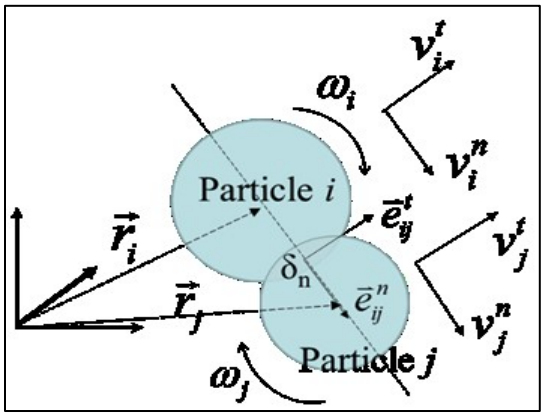

Figure 3.1 Kinematics of two adjacent particles.

The inter-particle contact force describes the force generated when two adjacent particles contact each other. In this study, this contact force is represented by using the Hertzian-Mindlin contact model. The normal contact force contains a nonlinear elastic term and a rate dependent dissipative term, and the tangential contact force contains a linear elastic term and a rate dependent dissipative term. The contact model can be written

$$F_{ij}^{c,n} = -k_n \delta_n^{1.5} - \eta_n \delta_n^{0.25} v_n \qquad [3.1]$$

$$F_{ij}^{c,t} = \min\left(-k_t \delta_n^{0.5} \delta_t - \eta_t \delta_n^{0.25} v_t, \mu F_{ij}^{c,n}\right) \qquad [3.2]$$

where $F_{ij}^{c,n}$ and $F_{ij}^{c,t}$ are normal and tangential contact forces between particle *i* and particle *j*. δ_n is the overlap in normal direction between particles in DEM simulations, which is given by $\delta_n = R_i + R_j - \left|\vec{r}_i - \vec{r}_j\right|$ (Figure 3.1). δ_t is the tangential relative displacement between two contacting points on two contacting particles. v_n and v_t are relative normal velocity and relative tangential velocity, respectively. k_n, k_t, η_n, and η_t are normal stiffness, tangential stiffness, normal damping coefficient, and tangential

damping coefficient, respectively, derived from material properties of grains. In the simulation, particle density is 2650 kg/m^3, elastic modulus is 29 GPa, and the Poisson's ratio is 0.20. In order to calculate the dissipative term, coefficient of restitution is set to be around 0.2. According to Foerster et al., the coefficient of friction is 0.1.

The second interaction force involves a so-called "lubrication" or "viscous" force associated with the interstitial fluid. We use formulas for both normal and tangential viscous force proposed by Pitois *et al*. (Pitois *et al*., 2000; Liu *et al*., 2013). These can be expressed as follows:

$$F_{\mathrm{ij}}^{\mathrm{visc,n}} = 6\pi\eta_{\mathrm{f}}R_{\mathrm{eff}}^2\frac{v_n}{h}\left(1 - 1/\sqrt{1 + V/(\pi R_{\mathrm{eff}}h^2)}\right) \quad [3.3]$$

$$F_{\mathrm{ij}}^{\mathrm{visc,t}} = 6\pi\eta_{\mathrm{f}}R_{\mathrm{eff}}v_t\left[\frac{8}{15}\ln\left(\frac{R_{\mathrm{eff}}}{h}\right) + 0.9588\right] \quad [3.4]$$

where $F_{\mathrm{ij}}^{\mathrm{visc,n}}$ and $F_{\mathrm{ij}}^{\mathrm{visc,t}}$ are normal and tangential viscous forces between particle *i* and particle *j*. R_{eff} is the effective radius calculated based on the radius of two contacting objects. *V* is the volume of fluid between two particles, which can be calculated based on the radius of particles, fluid properties, and the surface properties of particles, and *h* is the gap between two particles (Figure 3.2a). When calculating lubrication forces, we consider the particle roughness, t, and maximum lubrication length, Hmax. When the gap between two particles is larger than 2Hmax, the viscous force is decreased to 0. When the gap between two particles is less than 2t, the viscous force becomes independent of the gap distance. Figure 3.2b depicts a qualitative relationship between the viscous force and the particle gap under the condition that the relative velocity is constant.

A concise expression for the governing equations (listed below, where m_i is the mass of particle *i*, J_i is the moment of inertia of particle *i*, $\vec{r}_i$ is the position vector, and $\vec{\theta}_i$ is the rotation vector of particle *i*) may be written:

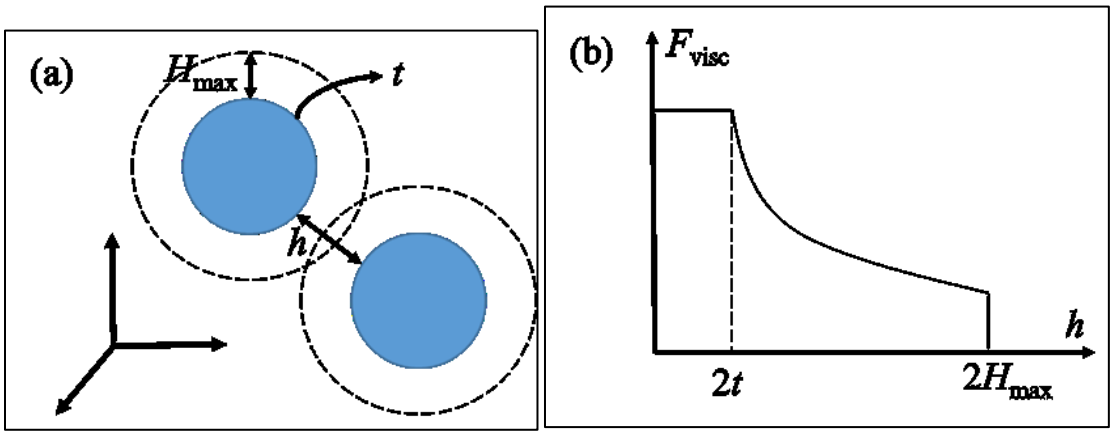

Figure 3.2 (a) Schematic of viscous force interaction of two adjacent particles, in which H_{max} is the maximum lubrication length, and *t* is the surface roughness of particles. (b) A sketch of the relationship between particle gap and viscous force for a constant relative velocity.

$$m_i\frac{d^2\vec{r}_i}{dt^2} = \sum_j\left(\vec{F}_{ij}^{c,n} + \vec{F}_{ij}^{c,t} + \vec{F}_{\mathrm{ij}}^{\mathrm{visc,n}} + \vec{F}_{\mathrm{ij}}^{\mathrm{visc,t}}\right) \quad [3.5]$$

$$J_i \frac{d^2\vec{\theta}_i}{dt^2} = \sum_j \left[\left(\vec{F}_{ij}^{c,t} + \vec{F}_{\mathrm{ij}}^{\mathrm{visc,t}} \right) \times \vec{n}_{ij} \right] \qquad [3.6]$$

We solve Equation 3.5 and 3.6 for particle rotational and translational positions and velocities by using the 4th order Runge-Kutta method.

The aforementioned DEM is used for some trial simulations of the compaction process in a Superpave gyratory compactor. The main purpose of the simulations is to examine the qualitative behavior of the compaction process. For this purpose, here we consider a simple viscous interstitial fluid with a uniformly particle size distributions (r = 1.0 mm ± 0.2 mm, where r is the radius of aggregates). Figure 3.3(a) shows a schematic of the imposed boundary condition of the simulation, and Figure 3.3b and c show the placement of particles in a cylindrical chamber.

In these trial simulations, we first investigate the influence of the chamber size on the simulation results. Here we consider three different chamber sizes D, i.e.: $D = 7.07d_{max}$, $D = 10.0d_{max}$, $D = 14.1d_{max}$, $D = 20d_{max}$, where d_{max} = the maximum aggregate diameter. Figure 3.4 shows the evolution of air void ratio versus the number of gyrations for different chamber sizes. It is clear that the chamber size has an influence on the simulated compaction behavior when the size is not too large compared to the aggregate size. However, when the chamber size becomes sufficiently large, the simulation results essentially converge. This indicates that, for the actual simulation of the gyratory compaction process, it is not necessary to simulate the actual size of the chamber. We can find a minimum representative chamber size, which can essentially yield the same compaction behavior as the actual process. This will significantly reduce the required computational time for the DEM simulation of gyratory compaction.

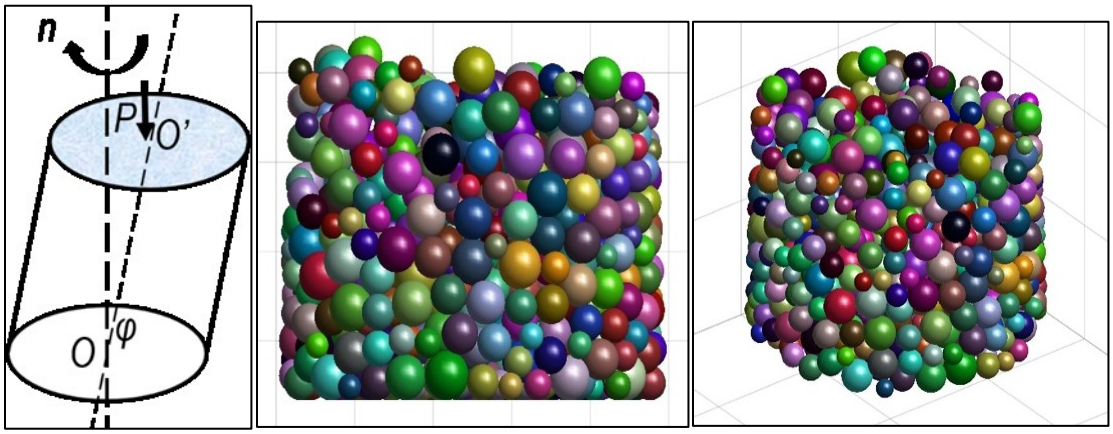

(a) (b) (c)

Figure 3.3 (a) Schematic of imposed motion and force for simulations of gyratory compaction, (b) side view of DEM model, and c) oblique view of DEM model.

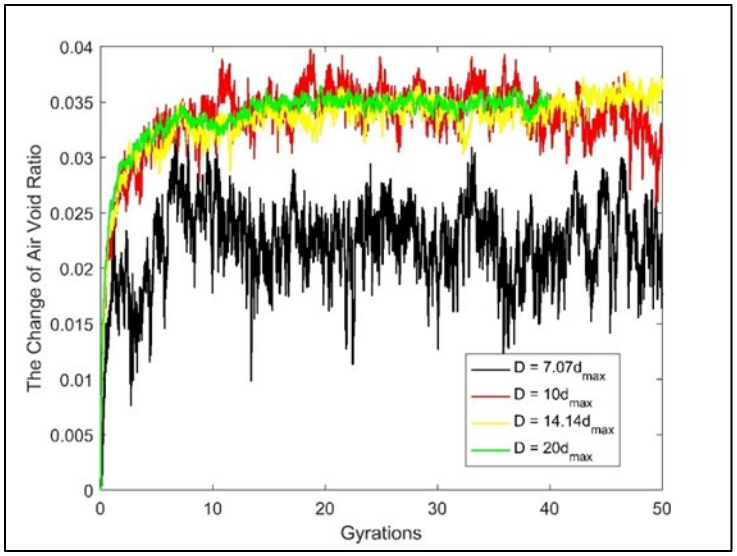

Figure 3.4 Simulated evolution of air void ratio versus gyration number for different chamber sizes.

We also investigate the effect of inter-particle friction on the compaction behavior of the mixtures. For this purpose, we consider a wide range of the values of inter-particle frictional coefficient: μ_p = 0.01, 0.05, 0.1, 0.2, 0.6, and 0.8. It is found that changing frictional coefficient can dramatically influence the compaction curve. Figure 3.5 shows the simulated change of air void ratio versus the number of gyrations for different input values of μ_p. It is seen that, as we increase the frictional coefficient from 0.01 to 0.2, the overall compaction performance is improved. However, a further increase in friction coefficient is shown to have an adverse effect on the compaction process. Besides, it is seen that a higher frictional coefficient also introduces unphysical large fluctuation effects to the whole system. Therefore, it appears that there is an optimum frictional coefficient for the compaction performance.

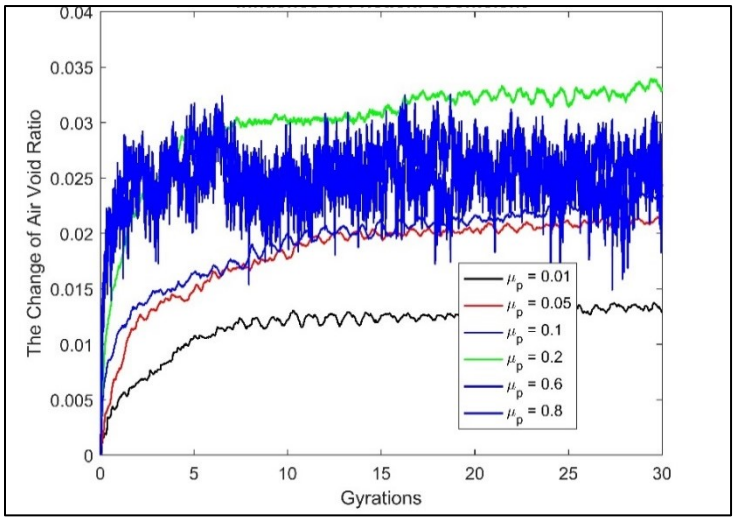

Figure 3.5 Simulated evolution of air void ratio versus gyration number for frictional coefficients.

Finally, we study the influence of the viscosity of inter-particle fluid on the compaction behavior. As a parametric study, we vary the viscosity of the fluid in the simulation from a much wider range (from 20

cP to 12500 cP) than that was typically found in the experiments. The simulation results are shown in Figure 3.6. It is observed that, despite the wide range of viscosities, the simulated compaction behaviors are essentially the same.

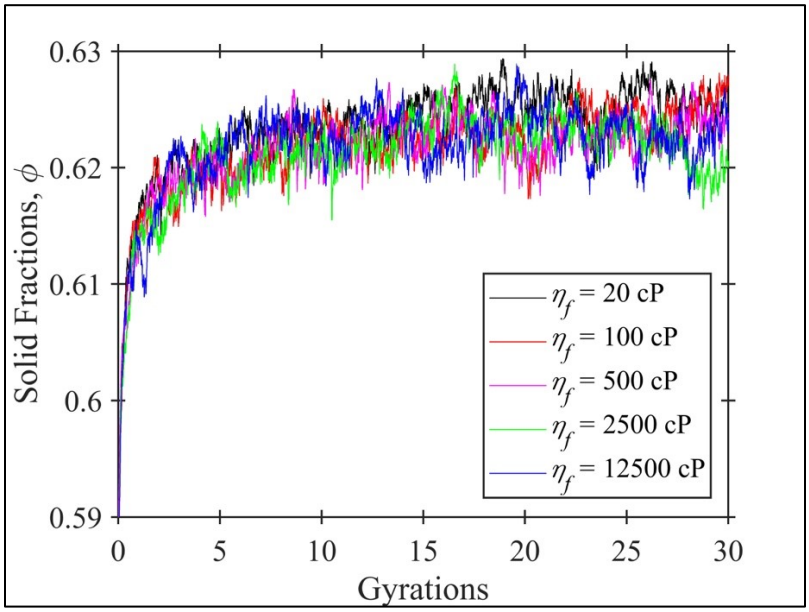

Figure 3.6 Influence of the inter-particle fluid viscosity on the compaction behavior

From Figure 3.4 to Figure 3.6, we observe that the simulations predict that the system reaches a steady state in about 5 gyrations, which is much faster than what is normally observed in the laboratory compaction experiments. This indicates that the time scale governing the compaction behavior in model does not match with the time scale of the actual compaction process. This could be due to the use of a simple viscous interstitial fluid model. Meanwhile, the non-contact particle interactions we used in this part are purely derived from the lubrication effect, which is too simple to describe the constitutive law of the mixtures existing between two aggregates. In the actual mixtures, the fluid between the aggregates consists of viscous binder and fines. Therefore, a more complex model will be needed.

3.3 DEVELOPMENT OF A TWO-SCALE DEM MODEL FOR ASPHALT MIXTURES

As mentioned earlier, one main drawback of DEM simulations is the required computational time especially when the system contains a large amount of fine particles. In a recent study on DEM simulations of low-temperature cracking of asphalt mixtures (Le et al. 2017), it was proposed to divide the aggregates into two categories, namely coarse aggregates and fine aggregates. In the DEM, only the coarse aggregates are modeled explicitly, and the contact law between the particles represents the collective behavior of the asphalt binder and fine aggregates, which is called the fine aggregate mixtures (FAM). It has been shown that the application of FAM effectively reduces the computational time of DEM without compromising the accuracy of the simulation. In the study, we use the concept of FAM for DEM simulation of the compaction process. In the DEM, the physical interaction between contacting particles is modeled by using the Hertzian-Mindlin contact theory with the rate dissipative terms

(Equations 3.1 and 3.2). The non-contact interaction between the coarse aggregates needs to capture the nonlinear fluid-like behavior of FAM. To this end, we modify the simple lubrication model (Equations 3.3 and 3.4) by incorporating a more complex material model.

To derive the constitutive law for the non-contacting behavior of FAM, we first introduce the inertial number of the system (Olivier Pouliquen and Forterre 2001; ; G.D.R. Midi 2004; Jop, Forterre, and Pouliquen 2006; Forterre and Pouliquen 2008):

$$I = \dot{\gamma} d / \sqrt{\sigma_n / \rho_s} \qquad [3.7]$$

where $\dot{\gamma}$ is the local shear rate of the system, d is the mean particle diameter, σ_n is the local pressure, and ρ_s is the density of the particles. For a granular material without interstitial fluid, the effective frictional coefficient, μ_{eff}, can be expressed as a function of I:

$$\mu_{\text{eff}} = \mu_1 + \frac{\mu_2 - \mu_1}{1 + I_0 / I} \qquad [3.8]$$

where μ_1 and μ_2, and I_0 are fitting parameters, but μ_1 and μ_2 can be seen as the effective frictional coefficients associated with quasi-static deformation and rapid collisional flows, respectively.

Adding interstitial fluid can bring much complexity to the system. Cassar *et al*. (2005) suggested that the behavior of the granular system can be classified into three different regimes: (i) free-fall regime, which is associated with dry granular system or where the effect of interstitial fluid is negligible; (ii) inertia regime; and (iii) viscous regime. Boyer *et al*. (2011) proposed that in viscous regime, the granular suspension can be fully described by another dimensionless number, i.e. viscous number:

$$I_v = \eta_{\text{f}} \dot{\gamma} / \sigma_n \qquad [3.9]$$

And the frictional rheology can then be written as the following form:

$$\mu_{\text{eff}} = \mu_1 + \frac{\mu_2 - \mu_1}{1 + I_0 / I} + I_v + 2.5 \phi_m I_v^{0.5} \qquad [3.10]$$

where ϕ_{m} is the maximum solid fraction of the granular system. When I_v is large, the system will converge to the Einstein rheology. Researchers also tried to investigate the transition from viscous regime to inertia regime in dense suspensions, for which a new dimensionless number, $K = I_v + \alpha I^2$, was proposed (Trulsson, Andreotti, and Claudin 2012), where α is a constant depending on the material properties.

To take into account both the collisional and lubrication effects, we propose a direct rheology to describe the behavior of granular system with wide range of both I and I_v, where $\mu_{\text{eff}}(I, I_v) = \mu_C(I) + \mu_F(I_v)$, and μ_C is the effective frictional coefficient due to particle collisions, and μ_F is the effective coefficient due to lubrication effect. Then, the overall frictional rheology can be written as

$$\mu_{\text{eff}} = \mu_1 + \frac{\mu_2 - \mu_1}{1 + I_0 / I} + \frac{\mu_3}{1 + I_1 / I_v} \qquad [3.11]$$

In addition, we can also obtain the relationship between solid fraction (volume fraction of the solid part only) and the dimensionless numbers, I and I_v, by considering the separation of dilation due to particle collision and lubrication interactions:

$$\phi = \frac{\phi_m}{(1+\alpha I)\left(1+\xi I_v^{0.5+I}\right)} \quad [3.12]$$

Here, we denote $\phi_m/(1 + \alpha I)$ as the collisional solid fraction, ϕ_c. We can then obtain the effective viscosity in both normal and tangential directions using such rheology.

$$\eta_{\mathrm{eff,t}} = 1 + \frac{5}{2}\phi\left(1 - \frac{\phi}{\phi_c}\right)^{-1} + \mu_C\left(\frac{\phi}{\phi_c - \phi}\right)^2 \quad [3.13]$$

$$\eta_{\mathrm{eff,n}} = \left(\frac{\phi}{\phi_c - \phi}\right)^2 \quad [3.14]$$

where $\phi_c = (1 + \alpha I)^{-1}\phi_m$ and $\mu_{\mathrm{C}} = \mu_1 + (1 + I_0/I)^{-1}(\mu_2 - \mu_1)$.

Now consider the FAM in between any two adjacent coarse aggregates in the aforementioned DEM simulation. Based on the relative position and relative velocity of the two aggregates, we can calculate the normal and tangential stresses on the boundary of the FAM material (Figure 3.7) as

$$\sigma_n = \eta_{\mathrm{eff,n}}\eta_{\mathrm{f}}\frac{v_{\mathrm{rel,n}} + v_{\mathrm{rel,t}}}{h} \quad [3.15]$$

$$\tau = \eta_{\mathrm{eff,t}}\eta_{\mathrm{f}}\frac{v_{\mathrm{rel,t}}}{h} \quad [3.16]$$

where $\eta_{\mathrm{eff,n}}$ and $\eta_{\mathrm{eff,t}}$ are effective viscosities in normal and tangential directions, respectively and $v_{\mathrm{rel,n}}$ and $v_{\mathrm{rel,t}}$ are the relative velocities between two surfaces in normal and tangential directions, respectively. h is the distance between two surfaces.

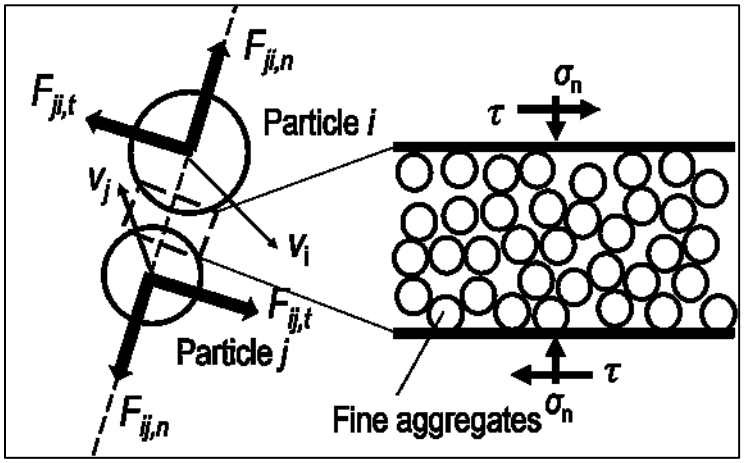

Figure 3.7 Formulation of non-contact interaction of FAM in DEM simulations.

We can then calculate the inter-particle viscous forces as

$$F_{ij}^{visc,n} = 6\pi R_{eff}^2 \sigma_n \left(1 - 1/\sqrt{1 + V/(\pi R_{eff} h^2)}\right) \quad [3.17]$$

$$F_{ij}^{visc,t} = 6\pi R_{eff} h\tau \left[\frac{8}{15}\ln\left(\frac{R_{eff}}{h}\right) + 0.9588\right] \quad [3.18]$$

where R_{eff} is the effective radius, which is given by $(R_i^{-1} + R_j^{-1})^{-1}$. Similar to Equations 3.3 and 3.4, we consider the FAM as the coating on the surface of coarse aggregates. Therefore, the maximum allowable magnitude of h should be twice the size of the coating, which is calculated based on the volume of FAM (Figure 3.2(b)).

By combining Equations 3.17 and 3.18 and the Hertzian-Mindlin contact theory, we can use Equations 3.5 and 3.6 to calculate the motion of each coarse aggregate, and therefore simulate the compaction curve of the asphalt mixtures.

3.4 PRELIMINARY COMPACTION EXPERIMENTS AND DEM SIMULATIONS

The proposed DEM framework is used to simulate a set of preliminary compaction experiments. The experiments involve both conventional asphalt mixtures and GNP modified asphalt mixtures. The aggregates were obtained from a local company. Figure 3.8 shows the size distribution of aggregates, based on which we group aggregates of a size larger than 2.36 mm as coarse aggregates. The FAM consists of aggregates size less than 2.36 mm and the binder. In this experiment, we use two types of binders: unmodified PG 58-28 and PG 58-28 modified by GNP 4827. For GNP modified binders, four different amounts of GNP (0.5%, 1.0%, 3.0%, and 6.0% by weight of the binder) are considered.

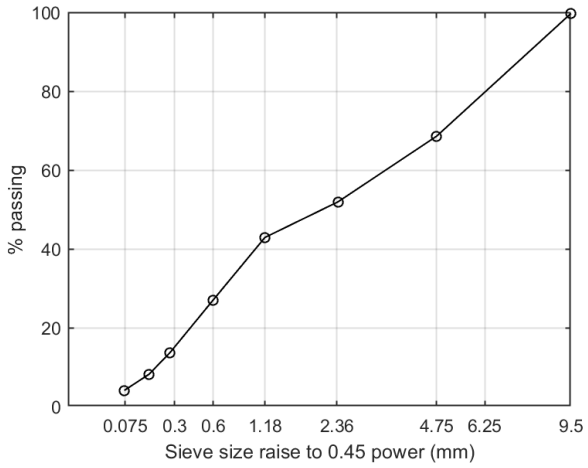

Figure 3.8 Sieve analysis of aggregate size

We first use a rotational viscometer to determine the viscosity of asphalt binders at different shear rate and different temperature. For each blend, the specimens are tested at angular velocity of 5 rpm, 10 rpm, 20 rpm, 50 rpm, and 100 rpm, and temperature of 100°C, 110°C, 120°C, 130°C, and 140°C. We first put the asphalt binder into the oven of 150°C, and then mix GNP and asphalt binder together using a high speed rotational mixer at constant temperature of 140°C.

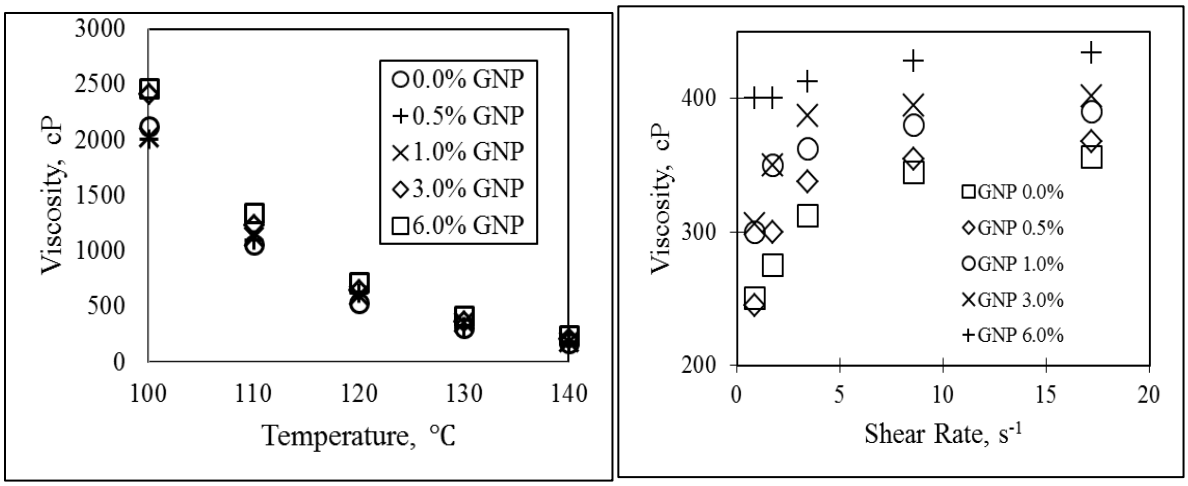

Figure 3.9 Measured viscosity of asphalt binders: a) at different temperatures, and b) at different strain rates at 130℃.

As seen in Figure 3.9, as we increase the temperature, the viscosity of asphalt binder decreases. At low temperatures, the change in GNP concentration has a more significant effect on viscosity than at high temperatures. When the temperature is at 130℃ or 140℃, the addition of GNP does not affect the viscosity of asphalt binder. In general, we observe that adding GNP leads to an increase in viscosity.

Compaction experiments are performed at 130℃. The pressure is kept constant at 600 kPa, the angle of gyration is set at 1.25 degree, and the gyratory rate is 30 gyration/min. Figure 3.10 shows the compaction curves experimentally obtained.

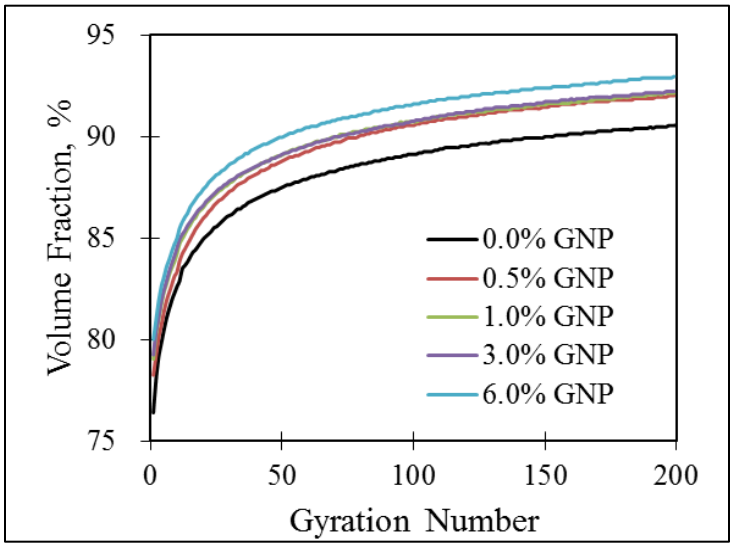

Figure 3.10 Measured compaction curves for both unmodified and modified asphalt mixtures.

It can be seen that the addition of a small amount of GNP improves the compaction of mixtures. It is also interesting to observe that the improvement from the addition of 0.5%, 1%, and 3% GNP is similar, while the effect of adding 6% GNP is much more significant. More importantly, the addition of GNP lowers the

initial solid volume fraction, which improves the overall compaction performance for a target air void ratio, which suggests that a higher viscosity (associated with GNP addition) results in higher densification in the incipient phase of compaction, after a few gyrations. We observe the same trend in the experimental data shown next.

The present DEM is used to simulate the aforementioned compaction experiments. There are gaps pre-set between two adjacent particles to take into account the volume of the fine aggregate asphalt mixture in between. As a preliminary study, we simulate the compaction process for the first 50 gyrations. In the simulations, prior to compaction, the random gap between coarse aggregates are set by using a random number, where the mean gap between aggregates is the coating size calculated based on the volume of FAM. Figure 3.11 shows the coarse aggregates at the beginning and the end of a compaction simulation. We can see that before compaction, the gaps between coarse aggregates are large, while after compaction, the mixture became close packed. In Fig. 3.11, the coordinates are normalized coordinates, thus are not equal to the actual dimension of Superpave gyratory compactor.

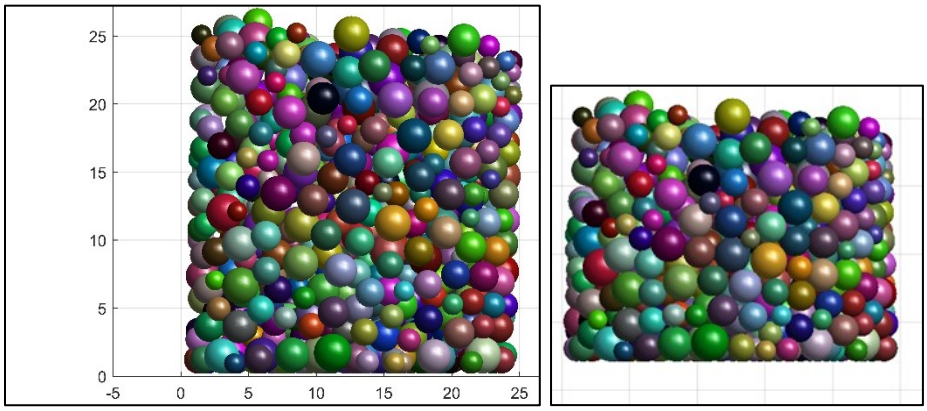

Figure 3.11 Snapshots from one simulation showing the state of the mixture from (left) the initial loosely placed material and (right) the final compacted state of the material.

The DEM model parameters are calibrated to fit the experimental results. We plot both the experimental and simulation results in Figure 3.12. It is seen that the DEM can also capture the overall shape and general trend of the compaction curve. For the case with the unmodified mixture, the simulation can almost predict the shape of the compaction curve. However, at early compaction stage, the simulated compaction rate is slightly larger than the measured one, while at the late compaction stage, the simulated compaction rate becomes slower than the experimental result. This implies that the model may over-predict the final air void ratio. Such a behavior is also seen for asphalt mixtures modified by 0.5%, 1% and 3% GNPs. For the case of 6% GNP addition, it is seen that the simulation result may underestimate the final air void ratio.

Despite the aforementioned discrepancy, the present simulations show that the proposed DEM can reasonably capture the overall compaction process of asphalt mixtures. However, the current simulations model all the aggregates as spherical particles, which is certainly an over-simplification. In the next stage of the project, we will improve the DEM by introducing asphereical particles, which will

give a more realistic representation of the aggregate shape and distribution. It is expected that it will improve the simulated compaction response.

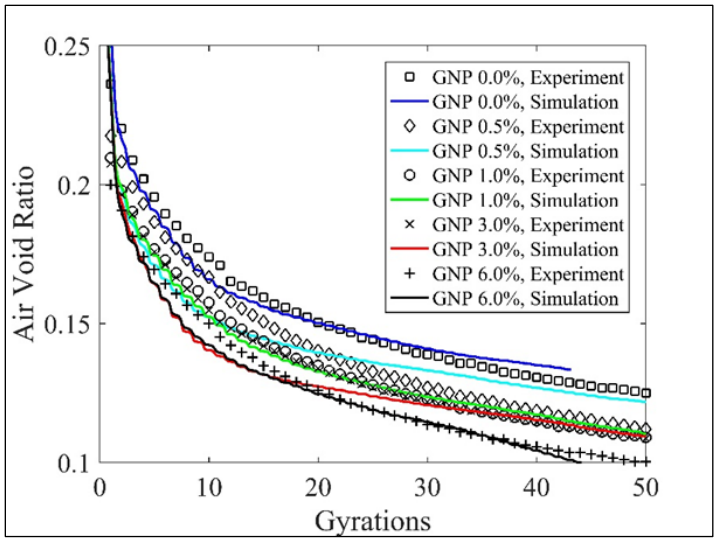

Figure 3.12 Measured and simulated compaction curves.

3.5 SUMMARY

In this chapter, we developed a two-scale DEM for simulation of the gyratory compaction process of asphalt mixtures. The model is anchored by the concept of FAM, whose constitutive behavior is represented by the contact law between coarse aggregates. In the DEM, the inter-particle contact law follows the Hertzian-Mindlin contact model, and the inter-particle non-contact law is derived from granular physics. We used the model to simulate a preliminary set of compaction experiments, which involve both unmodified and GNP modified asphalt mixtures. We showed that the present DEM can capture reasonably well the overall compaction process. Nevertheless, the current simulation does not consider the random aggregates shape, which may further help improve the simulation results. In addition, the rheology model of the FAM is calibrated to fit the experiments.

In the next stage of the research, we will further improve the DEM by 1) incorporating asphericity of coarse aggregates and 2) determining the rheology of FAM through a set of fine-scale DEM simulations. We will perform a set of gyratory compaction experiments on asphalt mixtures, which will be compared with the DEM simulations.

CHAPTER 4: EXPERIMENTAL CALIBRATION AND VALIDATION OF COMPUTATIONAL MODEL

4.1 INTRODUCTION

In this chapter, the computational model proposed in Chapter 3 is calibrated and validated using mix design and experimental compaction data for three Superpave 5 asphalt mixtures. In the process of calibration and validation, the coarse aggregates were modeled as non-spherical particles, the fine-scale computational model was validated using angle-of-repose experimental data for FAM, and based on the results, the rheological model for FAM was calibrated.

4.2 EXPERIMENTAL DATA FOR MODEL CALIBRATION AND VALIDATION

After a number of iterations regarding the selection of the best available compaction data for the computational model, the research team was able to obtain gradation and compaction information for a set of Superpave 5 asphalt mixtures that were used in pavements constructed in Indiana. The information was obtained from the North Central Superpave Center at Purdue University. Table 4.1 details the design parameters for the Superpave 5 mixtures and Figure 4.1, 4.2, and 4.3 present the compaction curves for the mixtures. Please note that Cat 3 means the mix was designed for 3 to 10 million ESALs and Cat 4 design is for greater than 10 million ESALs.

Table 4.1 Indiana Superpave 5 mixtures

	Category 3 NMAS = 9.5mm				Category 4 NMAS = 9.5mm			Category 4 NMAS = 19mm			
Parameter	N30	N50	N70	N100	N30	N50	N100	N30	N50	N70	N100
G_{sb}	2.694	2.692	2.692	2.692	2.626	2.630	2.631	2.651	2.650	2.665	2.665
% AC	6.0	6.0	5.9	5.9	6.4	6.4	6.5	5.1	5.1	4.7	4.7
G_{mm}	2.533	2.537	2.534	2.534	2.469	2.471	2.485	2.498	2.513	2.514	2.516
VMA	16.3	15.8	16.0	15.1	16.4	16.4	15.0	14.9	14.4	14.5	13.6
V_a	**5.3**	**4.9**	**5.1**	**4.1**	**5.0**	**4.9**	**3.8**	**4.9**	**4.9**	**4.9**	**4.0**
VFA	67.7	68.9	67.9	72.8	69.6	69.9	74.9	67.2	65.9	66.2	70.7

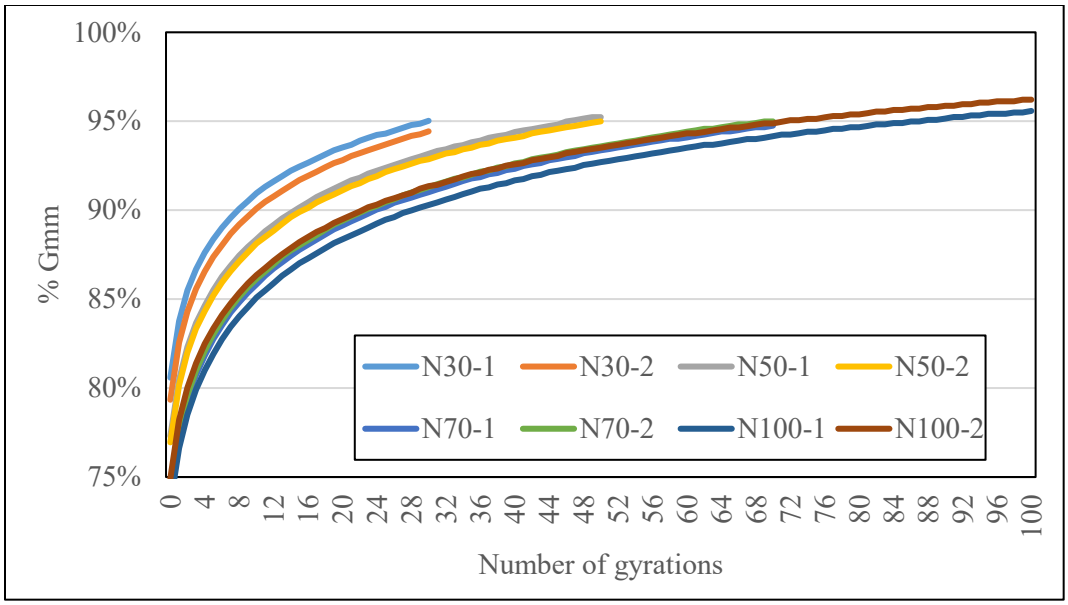

Figure 4.1 Compaction curves for Category 3, NMAS = 9.5mm

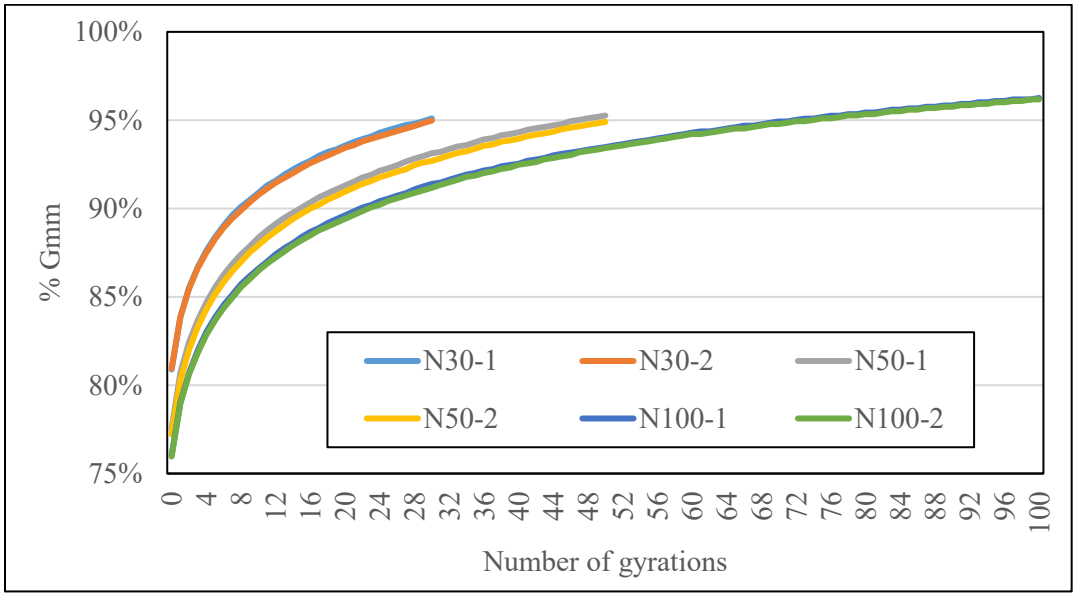

Figure 4.2 Compaction curves for Category 4, NMAS = 9.5mm

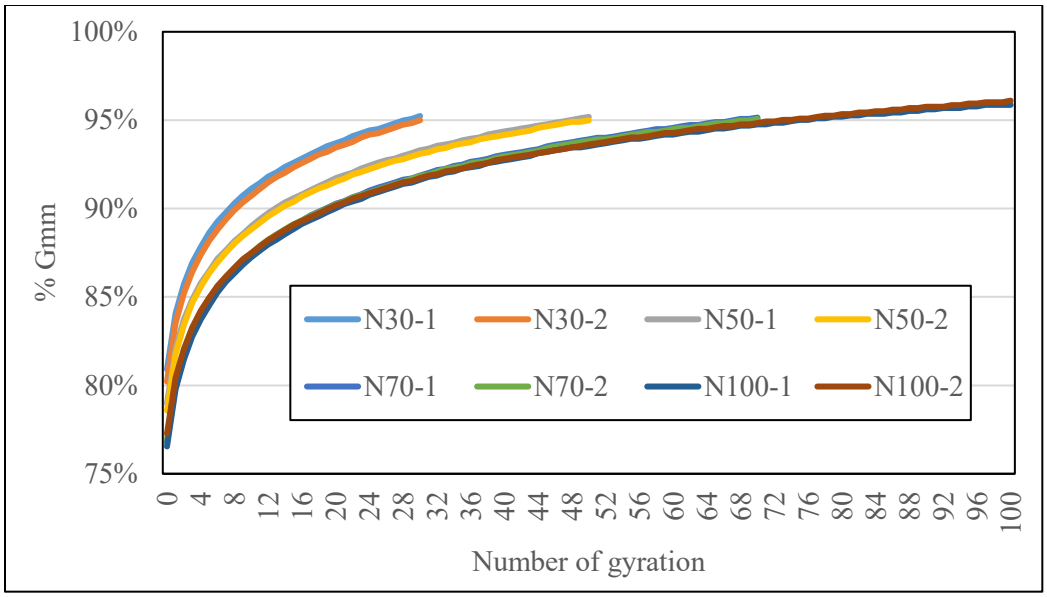

Figure 4.3 Compaction curves for Category 4, NMAS = 19mm

In Chapter 3, we developed a two-scale discrete element model (DEM) for simulating the compaction behavior of hot asphalt mixtures. To balance the efficiency and accuracy of the computation, the model was formulated at two scales. On the macroscopic level, only coarse aggregates were considered in the simulation. The interaction between these aggregates, which represents the combination of asphalt binder and fine aggregates, hereinafter called fine aggregate matrix (FAM), was described by using the theory of granular physics, and was calibrated by the DEM simulations of the FAM. In this recently developed model, the coarse aggregates were modeled by a set of spherical particles, which is certainly an over-simplification. Meanwhile, the model has not been used to examine the effect of aggregate gradation on the overall compaction behavior of the mixture.

In this chapter, we improve the model by considering non-spherical particles. The model is used to simulate the compaction behavior of the Category 3 mixtures with four aggregate gradations (N30, N50, N70, and N100). It is shown that the model is capable of capturing the overall compaction curve reasonably well. Meanwhile, an angle of repose experiment is performed on the fine aggregate matrix (FAM), and is used to calibrate the fine-scale computational model for the rheology of the FAM. The next sections summarize these new developments.

4.3 DISCRETE COMPUTATIONAL MODEL WITH NON-SPHERICAL PARTICLES

4.3.1 Non-spherical particles (Composite particle model)

Previously, we developed a two-scale discrete computational model for simulating the compaction of asphalt mixture in which we used spherical particles to represent coarse aggregates in the mixture. While the spherical particle model allows for an efficient simulation of large systems, we noted that there are several drawbacks. The most obvious one is that the model cannot capture realistically the interlock between spherical particles. In order to capture more realistically the interactions between

aggregates, we improve the model by considering the non-spherical particles. The simplest method to model such non-spherical particle is to combine several spheres to establish one complex particle, which is referred to as the composite particle (Poschel and Schwager, 2005).

In the composite particle model (CPM), we combine two spherical particles to form a composite particle, the larger particle (particle i in Figure 4.4(a)) is called the main particle, and the smaller particle (particle i + 1 in Figure 4.4 (a)) is called the peripheral particle. Geometrically, we position the center of particle i + 1 on the surface of particle i. The sphericity of a particle can be evaluated by adjusting the ratio between the radii of the outer and inner spheres. Here we define the measurement of non-sphericity, S, using the following equation:

$$S = 1 - L/2R \qquad [4.1]$$

where $L = \max\left\{R_i + R_{i+1} + \frac{R_i}{\sqrt{2}}, 2R_i\right\}$ = the size of the enveloping square, $R = R_i + 0.5R_{i+1}$ = the radius of the enveloping circle, which are shown in Figure 4.4(a), and R_i, R_{i+1} = radii of particles i and i + 1, respectively. As we change the ratio between particle i + 1 and particle i from 0.0 to 1.0, we can obtain the relationship between R_{i+1}/R_i and S shown in Figure 4.4 (b). In this study, we choose $R_{i+1} / R_i = 0.5$, which corresponds to a value of non-sphericity S equal to 0.117.

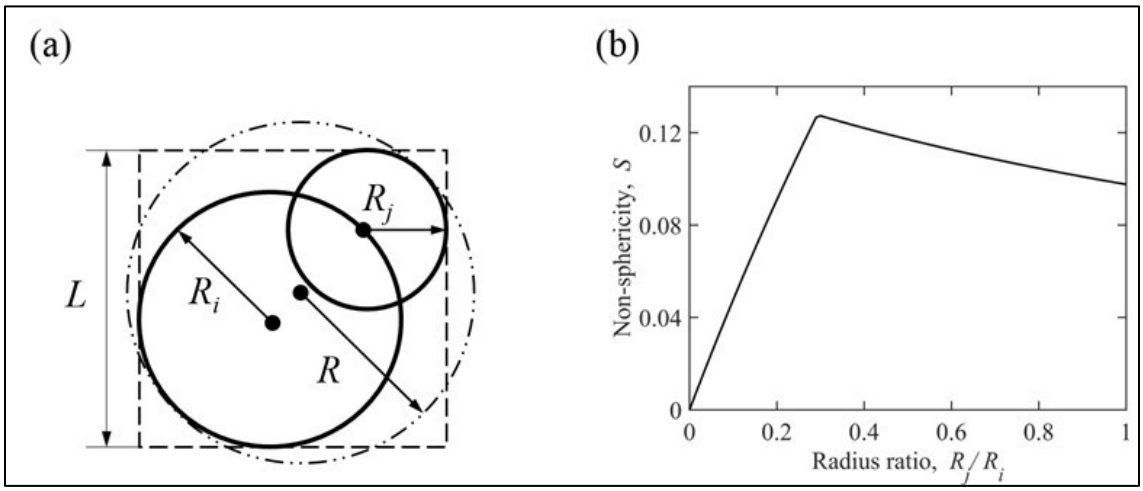

Figure 4.4 (a) Composite particle model; (b) Measure of non-sphericity of CPM as a function of the ratio between peripheral particle size and the main particle size.

To combine the two spheres as a single particle, we assign both normal and tangential springs to connect the individual spheres. The stiffness of springs is set to be the same as the stiffness of the Hertz-Mindlin contact law in the following section. Also, no slippery between two spheres is allowed so that the composite particle can move as a single elastic body. Besides, the volume of the composite particle is calculated using a Monte Carlo algorithm where random points were generated within the enveloping squares and the possibility of point falling within the composite particle can be calculated accordingly.

4.3.2 Simulation framework and aggregate interactions

In the previous chapter, we developed a two-scale DEM for simulations of the compaction process of hot asphalt mixture based on the FAM concept. In the simulation, we explicitly modeled the coarse aggregates only, while the FAM was smeared into the contact behavior of coarse aggregates. In the model, the coarse aggregates were modeled as spherical particles, whose size distribution based on the sieve analysis. During the compaction process, the FAM can reasonably be regarded as an interstitial granular-fluid system. The particle interaction can be divided into two types: 1) contact interaction when the adjacent particles are in touch with each other, and 2) non-contact interaction due to the viscous behavior of the FAM. The Hertz-Mindlin contact theory and lubrication theory were used to model the contact and non- contact particle interactions, respectively. The details of the contact interaction and non-contact interaction between coarse aggregates were presented in the previous chapter report. The dynamic equilibrium of the entire assembly of particles is enforced by applying the Newton 2nd law to each individual particle (i.e. Equations 3.5 and 3.6). The entire system of equilibrium equations is solved by using the 4th order Runge-Kutta method.

4.4 CALIBRATION OF DEM MODEL OF FAM

The essential ingredient of the proposed DEM model is the constitutive behavior of the FAM, which is hinged on the understanding of its rheology. Previous research attempted to characterize the aggregate interactions by studying the constitutive behavior of asphalt mastic, which consists of asphalt binder and fillers. However, asphalt mastic is a thin granular suspension while the FAM is a dense granular material with interstitial viscous fluid. The rheology of asphalt mastic is fundamentally different from that of the FAM (Abbas et al., 2007; Chen et al., 2012). In this study, we develop a rheology model for FAM informed by a set of fine-scale DEM simulations of FAM in a 3D Couette cell. Similar to the simulation framework of the compaction of asphalt mixtures, in this fine-scale DEM model, we use the Hertz-Mindlin contact theory to model the particle collisions, and the lubrication theory to model the viscous effect.

To calibrate the fine-scale computational model, we perform a numerical simulation of the angle of repose of the FAM, and compare it with the physical test. In the physical test, we designed the test channel as shown in Figure 4.5. We first heated the channel and FAM to the prescribed testing temperature (150°C) in the oven. After half an hour, we can take both the channel and the FAM out of the oven, and place the FAM into the confining portion of the channel. We then put the whole system into the oven again for 5 minutes to reheat the material to the designed temperature. After taking out the device from the oven, we removed the confining plate and let the FAM flow freely toward the opening end of the channel. The FAM flow stops quickly. We use a hand-held thermometer to measure the temperature along the flow surface and we observe no obvious temperature variation.

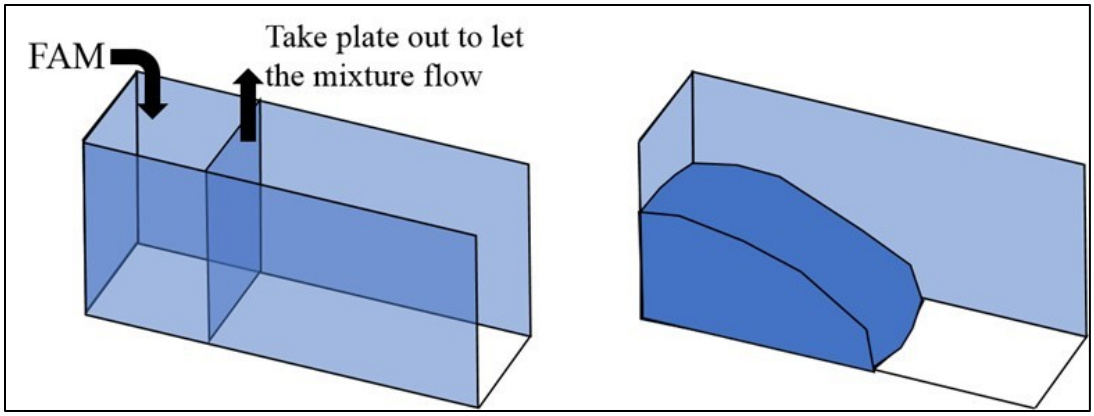

Figure 4.5 Design of the angle-of-repose experiment on FAM.

After one day, the FAM has become solid state, and we removed the cardboard channel so that we can clearly see the flow profile (see Figure 4.6). Using this flow profile, we can define the angle of repose of the FAM at the testing temperature. The final profile of the FAM is compared with the DEM simulation.

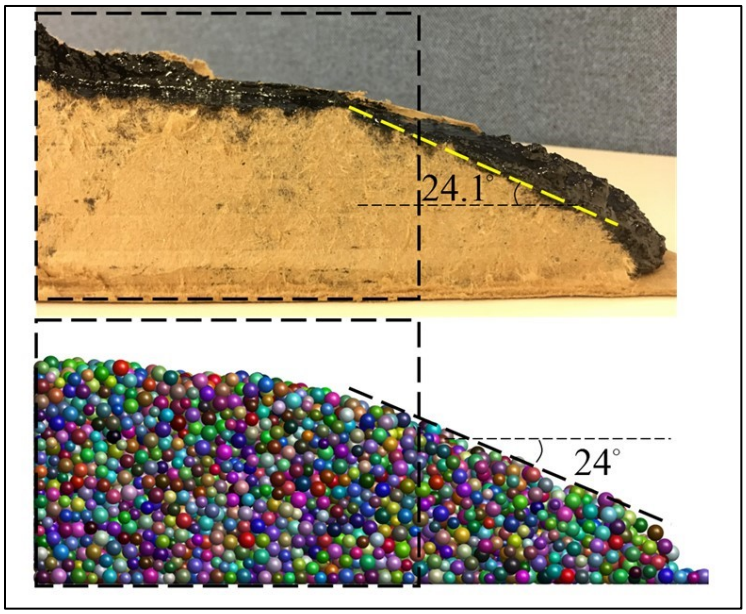

Figure 4.6 Comparison between the measured and simulated repose angles.

The fine-scale DEM is used to simulate the angle of repose experiment. The measured binder viscosity (150 cP) is directly used for the model. The particle size distribution to be uniformly distributed between 0.8*d* and 1.2*d*, where *d* is the median aggregate size of the FAM. The only parameter that needs to be calibrated are the inter-particle frictional coefficient. It is found that, when we set the inter-particle frictional coefficient, μ_p, to be 0.1, the simulation result can match the experimental observation very well.

4.5 RHEOLOGY OF THE FINE AGGREGATE MATRIX

Section 3.3 presents the mathematical model of the rheology of FAM. However, the model parameters for Equation 3.11 are left undetermined. The previous section showed that the fine-scale DEM can capture the angle of repose of the FAM at the relevant testing temperature. To determine the model parameters for the rheology of FAM, we use the aforementioned DEM to simulate the behavior of a granular-fluid system in a 3D Couette cell under simple shear, as shown in Figure 4.7. The cell has a dimension of 30 mm in *Y*−direction and 58.3 mm in *Z*−direction, and the initial dimension in *X*−direction is 51.5 mm. Periodic boundary conditions are prescribed on the upper and lower boundaries so that the simple shearing system can reach a steady-state condition. The left vertical wall, also called the translational wall, is assigned with a constant velocity U_w while the right vertical wall, called the non-translational wall, is restrained in *Y*− and *Z*− directions. The right wall is allowed to move in x−direction so that a constant pressure can be maintained throughout the simulation. To create a rough interface between the particles and the two vertical walls, particles whose centroid is less than a certain distance (2.5 mm in the current simulation) to the vertical walls are glued to the walls so that they will have the same velocity as the wall.

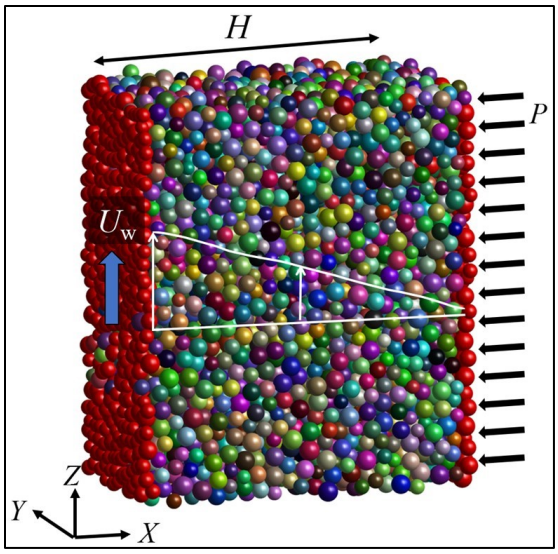

Figure 4.7 DEM simulation of simple shear test, where the white line denotes a typical velocity profile obtained by a single simulation.

In the DEM, the influential distance of the lubrication effect is considered to be equal to the average particle diameter. To test the system for a wide range of conditions, we choose the viscosity of interstitial fluid ranging from 0 cP to 20000 cP. On the non-translation wall, we apply different levels of constant pressures, which vary from 100 Pa to 100 kPa. On the translation wall, we apply constant velocity in a way that the glued particle on this wall can move with the wall at the same velocity. The wall velocity varies from around 0.001 m/s to 10 m/s.

During the simulation, the system experiences simple shear driven by the motion of the vertical wall with a constant velocity. As the system reaches a steady state, which is manifested by a stabilized

boundary shear stresses, we obtain a linear velocity profile in the Couette cell shown in Figure 4.7. The different sets of model parameters in the simulation correspond to a wide range of the inertia number (Equation 3.7) and the viscous number (Equation 3.9): $I \in [10^{-3}, 1]$ and $I_v \in [10^{-7}, 1]$.

Figure 4.8(a) shows the simulated relationships between the effective frictional coefficient μ_{eff} and the viscous number I_V for different values of the inertia number I. It is seen that, for a given inertial number, the effective frictional coefficient increases with the viscous number. When the viscous number is small, the effective frictional coefficient approaches an asymptotic value μ_0, which is dependent on the inertia number. Figure 4.8(b) presents the relationship between the asymptotic value μ_0 and the inertia number. For a sufficiently small inertia number, μ_0 approaches a constant. We use Equation 3.10 to fit the simulated $\mu_{eff} - I_V$ curve for the case of small inertia number ($I \leq 0.01$), as shown in Figure 4.8(a). It is clear that Equation 3.10 can provide an optimum fit of the most part of the curve except for large viscous numbers ($I_V \geq 0.1$).

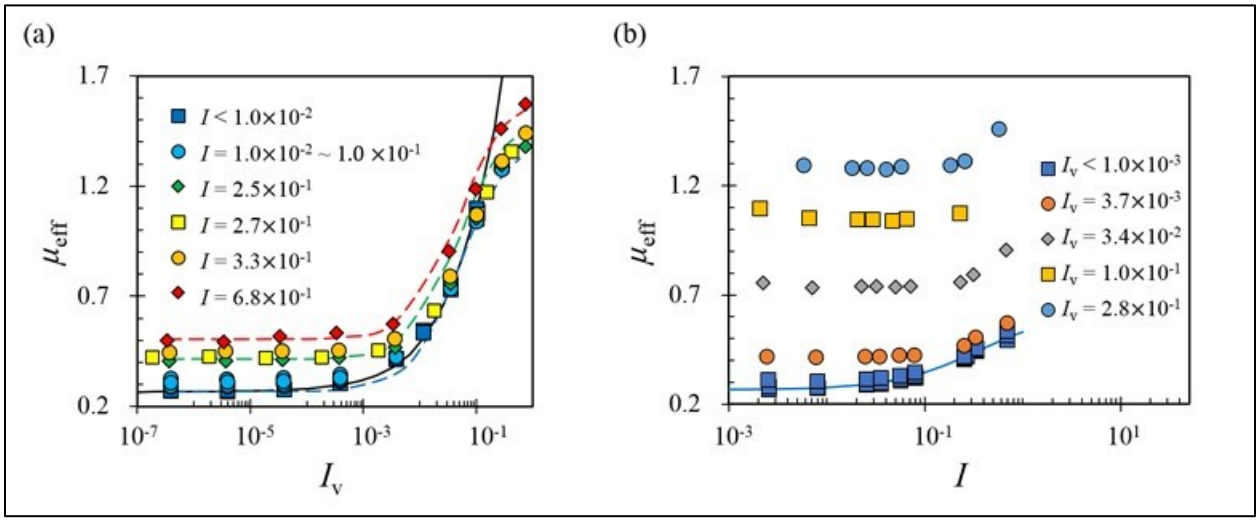

Figure 4.8 (a) Relationship between viscous number, I_V, and effective frictional coefficient, μ_{eff} (The solid line is the optimum fitting by Equation 3.10, and the dash lines are fitting curves based on Equation 3.11). (b) Relationship between I_V and solid fraction (The solid line of the optimum fitting by Equation 3.8).

Meanwhile, by comparing the $\mu_{eff} - I_V$ curves for different inertia numbers, we observe that the difference in the effective friction coefficients for different inertia numbers is almost independent of the viscous number. This implies that the effective frictional coefficient can be expressed as

$$\mu_{\text{eff}} = \mu_c(I) + \mu_f(I_v) \qquad [4.2]$$

which forms the basis for the rheology model presented in Section 3.3. The physical justification for Equation 4.2 is that the behavior of the current granular-fluid system is influenced by both the particle inertia and the viscosity of the interstitial fluid. Therefore, the rheology model should include the contributions from both particle collision and viscous interaction. Therefore, we may write the effective frictional coefficient as the sum of the contact contribution and the lubrication contribution.

Function $\mu_c(I)$ of Equation 4.2 can be determined from the aforementioned $\mu_{eff} - I_V$ curve (solid curve in Figure 4.8(b)), and function $\mu_f(I_v)$ can then be obtained from any one of the $\mu_{eff} - I_V$ curves. This allows us to determine all the constants in Equation 3.11, i.e.

$$\mu_{\text{eff}} = 0.265 + \frac{0.36}{1+0.35/I} + \frac{1.15}{1+0.05/I_v} \qquad [4.3]$$

The effective viscosities η_n and η_s of the FAM can then be determined by Equations. 3.15 and 3.16.

The constitutive law of the DEM model is numerically implemented in an explicit manner. Suppose that we have determined the particle positions, particle velocities, and particle interactions, from the previous calculation step. As we proceed to the current time step, we first need to check the contact condition between two particles. If two particles are not physically in contact, we need to calculate only the lubrication forces. Otherwise, both lubrication forces, $F_{\text{ij}}^{\text{visc,n}}$ and $F_{\text{ij}}^{\text{visc,t}}$ (Equations 3.17 and 3.18), and Hertz-Mindlin contact forces, $F_{ij}^{c,n}$ and $F_{ij}^{c,t}$ (Equations 3.1 and 3.2), will be calculated. Hertz-Mindlin contact forces can be determined based on the overlap and relative velocities of the particles calculated from the previous time step. For the lubrication forces, we can calculate the effective pressure between two particles. Together with the previously determined normal and tangential relative velocities, we can calculate shear rate between particles and inertia number I and viscous number I_v in the interstitial FAM. Through the present rheology model, we can determine the normal and tangential effective viscosity inside the interstitial FAM. Therefore, we can calculate the new lubrication forces. With all the updated interaction forces, we can solve the system of equilibrium equations (Equations **Error! Reference source not found.** and **Error! Reference source not found.**) to update the particle positions, velocities, and accelerations.

4.6 MODEL VALIDATION AND DISCUSSION

4.6.1 Experiments

To validate the proposed two-scale DEM, we performed a set of laboratory experiments on mixtures made of asphalt binder (PG64-22) but four different aggregate size distributions (i.e. N30, N50, N70, and N100). Figure 4.9 shows the gradation curves of the four types of aggregates. The compaction temperature was set to be equal to 135°C, and at that temperature, the viscosity of binder is around 250 cP. The mass ratio between asphalt binder and the whole mixture is 6%. The compaction tests were done according to ASTM D6925. The gyratory compactor consists of a cylindrical gyratory ring, a loading plate and a gyratory plate. During the compaction process, the bottom plate moves vertically while keeping a constant pressure of 600 kPa, and meanwhile to top plate gyrates horizontally with gyratory speed of 30 rpm, which leads to the gyratory motion of the cylindrical ring with a gyratory angle of 1.25°. Figure 4.10(a) shows the configuration of the Brovold gyratory compactor.

Experiments showed that the mixture with N30 aggregates can be compacted to a final volume fraction of 95% after 30 gyrations at temperature of 135°C. Similarly, the mixture with N50 aggregates can be compacted to 95% volume fraction after 50 gyrations, the mixture with N70 aggregates can reach 95%

volume fraction after 70 gyrations, and the mixture with N100 aggregates can reach 95% volume fraction after 100 gyrations. The results are shown in Figure 4.10(b).

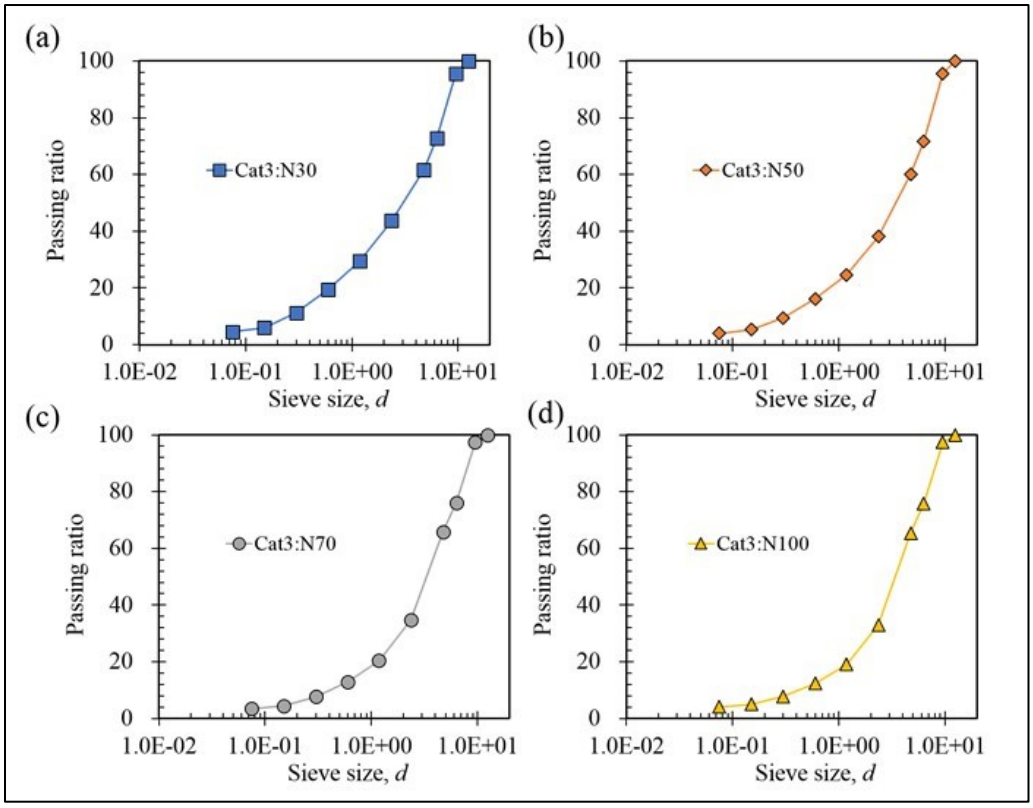

Figure 4.9 Grain size distribution of four different mix designs.

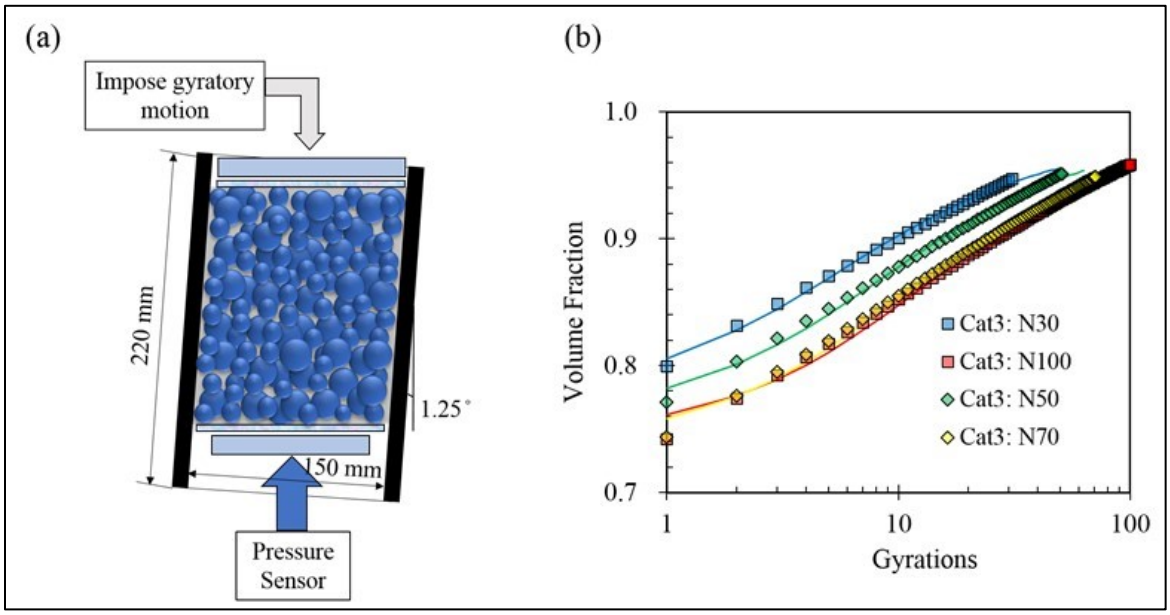

Figure 4.10 (a) The configuration of the gyratory compaction test; (b) Results of the compaction test, the markers are compaction test results and the solid curves represent fitting curves.

It is found that the measured compaction curves can be fitted by the following equation:

$$\phi(t) = 1 - \frac{1-\phi_0}{1+Bln(1+\frac{t}{\tau_0})} \quad [4.4]$$

where t = time, ϕ_0 = initial solid volume fraction of the mixture, B and τ_0= model constants to be fitted. The fitting parameters for each mixture are shown in **Error! Not a valid bookmark self-reference.**.

Table 4.2 Parameters of Equation 4. for optimum fitting of the compaction curves

Test	ϕ_0	B	τ_0
Cat3:N30	0.7750	3.326	20.76
Cat3:N50	0.7585	4.571	42.06
Cat3:N70	0.7377	4.214	49.05
Cat3:N100	0.7443	5.649	78.46

4.6.2 Simulation of Gyratory Compaction of Asphalt Mixtures

The present model is used to simulate the aforementioned gyratory compaction experiments of asphalt mixtures. Based on the aggregates used in the aforementioned experiments, we use the following particle properties: particle density is 2650 kg/m^3, elastic modulus of the particle is 29 GPa, and Poisson's ratio is 0.20. For calculating the Hertz-Mindlin contact forces, the damping coefficient is determined based on α = 0.9. According to [5], the coefficient of friction between particles, μ_p, is set to be 0.10. The particle size distribution follows the gradation curve of the aggregates shown in Figure 4.9.

The rheology of the FAM is represented by Equations 3.15, 3.16 and 4.3. As mentioned in the previous section, the $\mu_{eff} - I - I_v$ relation is determined by the fine-scale DEM simulation of a simple shear test on FAM. In the aforementioned simple shear simulations, the mean particle size corresponds to the median aggregate size of FAM, which is about 1 mm. Though the range of particle size used in the simulation is considerably smaller than that actual particle size distribution of FAM, recent studies have shown that the rheology of granular mixture scales is primarily governed by the median grain size (Hill and Yohannes, 2011; Yohannes and Hill, 2010). The effective viscosities of the FAM are then calculated based on the $\mu_{eff} - I - I_v$ relation through measured viscosity of the binders (Equations **Error! Reference source not found.** and **Error! Reference source not found.**).

At the beginning of the simulation, about 1000 particles were generated according the size distribution of the coarse aggregates and these particles dropped into a tilted cylindrical chamber. In order to consider the coating thickness of the FAM on the surface of coarse aggregates, we keep the distance between surfaces of adjacent particles to be equal to twice the thickness of particle coatings, where the coating thickness is calculated as

$$t_c = \left[(1 + \frac{1}{\phi_{vol}})^{\frac{1}{3}} - 1\right] R_a \quad [4.5]$$

where$\phi_{vol} = V_{ca}/V_{FAM}$, R_a is the average radius of coarse aggregates, and V_{ca},V_{FAM} are the volumes of coarse aggregates and FAM, respectively.

After particles are dropped into the cylindrical ring, the top plate is added to the simulation. As the bottom plate starts to be pushed upward at a constant pressure of 600 kPa, the top plate and the cylindrical ring are set to gyrate with the same manner as the experimental setup, and the entire simulations run for 30 to 100 gyrations for different mixtures. A small-time increment, which is on order of 10^{-8} seconds, is used to ensure the stability of the simulation.

During the simulation, the movement of the bottom plate is recorded, from which we can calculate the volume fraction of the asphalt mixture as

$$\phi_{vf}(t) = \frac{V_{ca}+V_{FAM}}{A_0 h(t)} \quad [4.6]$$

where $\phi_{vf}(t)$ is the volume fraction of the asphalt mixture at time t, A_0 is the cross-section area of the cylindrical gyratory ring in the simulation, and $h(t)$ is the distance between the top and bottom plates measured at time t. Equation 4. can be used to obtain relationship between $\phi_{vf}(t)$ and gyration number based on the gyration speed.

4.6.3 Results and Discussion

Figure 4.11 shows the comparison between experimental and simulation results. The open markers represent the experimental results, and the solid curve in each sub-figure represents the simulation result. It is seen that simulation results agree with the experimental measurement reasonably well and that DEM can predict final compaction state well, a key measure of the compactability of the mixture.

It is seen that the simulation predicts a considerable slower compaction rate as compared to the experimental result for the initial part of the compaction process. This indicates that the composite particles are able to enhance the interlock between aggregates, which hinders the particle rearrangement during the compaction process. Note that, in the present simulation, we used a high non-sphericity level (S = 0.117). It can be expected that the initial portion of the simulated compaction curves can be improved if we consider a lower level of non-sphericity.

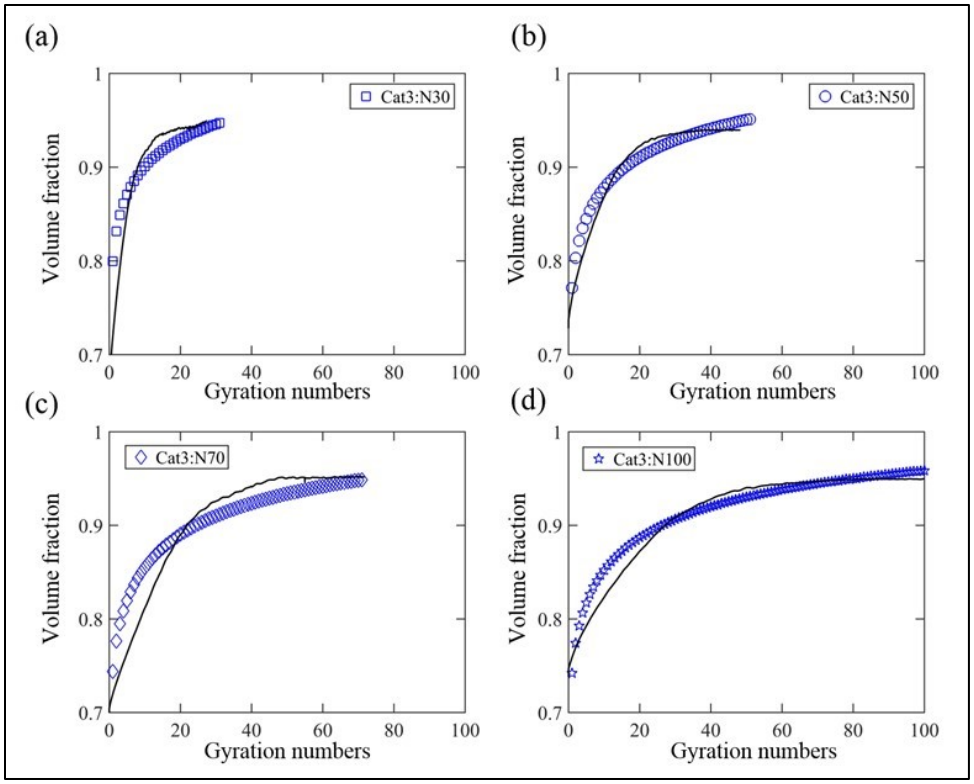

Figure 4.11 The comparison between experiments and simulation results. The markers represent experimental results, while the solid curves represent simulation results.

4.6.4 Conclusions

In this chapter, we presented a two-scale DEM computational model with non-spherical particles (composite particle model) to simulate the compaction behavior of asphalt mixtures. The main idea is to simulate the behavior of fine aggregate mixtures using the rheology of granular-fluid systems, while simulating the motion of coarse aggregate explicitly as composite particles. We calibrated the fine-scale DEM using the angle of repose experiment, and the model was subsequently used to determine the rheology of FAM. We then simulated the compaction of asphalt mixture based on the rheological model of FAM and the size distribution of the given experiments. The comparison between experiments and simulations shows that the current DEM simulation with composite particle model can capture the overall effect of gradation of aggregates on the bulk part of the compaction curves. However, we found that, for the initial portion of the compaction curve, the simulation results deviate from the experiments, which can be attributed by the fact that the interlock between composite particles hinders the particle rearrangement. We expect that the simulation can be improved by considering a different level of non-sphericity.

CHAPTER 5: MECHANICAL TESTING OF ASPHALT MIXTURES

5.1 INTRODUCTION

In this task, we performed laboratory experiments to evaluate the mechanical properties of different mixtures that used in the 2017 NRRA study at MnROAD. We conducted the following experiments: Bending Beam Rheometer (BBR) Creep and Strength, Indirect Tensile (IDT) Creep, Diametral Dynamic Modulus (E*), Semi-Circular Bending (SCB), Uniaxial Dynamic Modulus (E*), and Flow Number (FN). The goal is to determine if there are significant differences between high density and conventional mixtures.

5.2 LABORATORY COMPACTION OF HIGH-DENSITY ASPHALT MIXTURES

First, three high-density mixtures were prepared and tested. The first two, Regressed Air Void (RG3) and MnROAD Superpave 5 (MnSP5), represent asphalt mixtures used in the 2017 NRRA study at MnROAD. These mixtures were used in the construction of Cells 989 and 990 and were designated with 5% and 3% target air voids and design gyrations of 50 and 90, respectively. Table 3 shows the details of loose mixtures used.

Table 5.1 Details of loose mixtures used in MnROAD Cells 989 and 990

Mixture ID	Mixture Type	Cell No.	Mix Design	Binder Grade (PG)	Lift	Agg. Size	Air Voids	N_{design}
SP5	Superpave 5	989	SPWEB450E	58H-28	2	12.5	5%	50
RG3	Regressed Air Voids	990	SPWEB430E	58H-28	2	12.5	3%	90

In the regressed air voids design, the mixture is initially designed for the traditional 4.0 % of air voids, and then the amount of additional binder needed to achieve 3.5% or 3% air voids is calculated and used in the final mix design. This increases the design asphalt content by up to 0.4 percent. The goal is to increase the in-place density, impermeability, durability, and film thickness (Wisconsin Asphalt Pavement Association, 2016).

The Superpave 5 asphalt mixtures are designed for 5% air voids and field compacted at the same 5% air voids. Unlike regressed air voids approach, the density is improved by adjusting the aggregates gradation with minimal changes to the binder content (Hekmatfar et al., 2015).

Gyratory compacted samples of 150 mm diameter were prepared at design gyratory levels. The loose mixtures obtained from MnROAD test sections were first warmed to a workable condition followed by sampling the representative sample of 4800 gm by quartering method (AASHTO R47-10). The sampled material was heated to mixing temperature to activate the binder, thoroughly mixed, and then brought to the compaction temperature. Table 5.2 shows the recommended compaction temperatures for the loose mixtures.

Table 5.2 Compaction temperatures for loose mixtures

Mixture ID	Mix Design	G_{mm} (Avg.)	Compaction Temp. (F)
SP5	SPWEB450E	2.431	247-255
RG3	SPWEB430E	2.470	247-255

The third mixture is a reproduced Superpave 5 mixture (UMDSP5), designed and prepared at University of Minnesota, Duluth. Table 5.3 shows the details (combined aggregate gradation, material proportions and volumetric properties) of Indiana's SP5 mixture design for Cat 3 traffic level (N_{design} -50). In the present work, a sieve analysis was conducted to determine the gradations of individual aggregates collected for reproducing the Indiana mix. The blending of these aggregates was performed to match the final combined aggregate gradation to Indiana's SP5 aggregate gradation. Asphalt mixtures were prepared at 297-310F and short-term aged (AASHTO R30-10) for 2 hours at 275F, followed by compaction at design gyration levels of 50 at recommended compaction temperature of 265-272F. Two gyratory compacted samples (150 mm height) were prepared for this mixture.

Table 5.3 Details of Indiana's SP5 mixture design for Cat 3 traffic level (3-10 million ESAL)

Combined aggregate gradation										
Sieve Size, mm	12.5	9.5	6.3	4.75	2.36	1.18	0.600	0.300	0.150	0.075
Cum. % Passing	100.0	95.6	71.7	60.1	38.1	24.6	16.1	9.5	5.3	4.0
Material proportions										
Material	Aggregate									**%AC**
	#11 stone		#12 stone		#24 Nat. Man. sand		Manufactured sand		BHF	
Proportions, %	40.3		28.5		8.1		20.7		2.4	6.0
Volumetric properties										
Parameter			G_{sb}		G_{mm}		VMA		V_a	VFA
Values			2.692		2.537		15.8		4.9	68.9

The height of the sample and the corresponding gyration numbers were recorded during the compaction of samples. The gyratory compaction curves (percentage theoretical maximum specific gravity (%G_{mm}) vs. No. of Gyrations) were plotted to evaluate the degree of compaction with respect to the number of gyration. The percentage theoretical maximum specific gravity (% G_{mm}) was determined using the following equation:

Percentage theoretical maximum specific gravity, $\% \, G_{mm} = \frac{G_{mb}}{G_{mm}} \times 100$

Where,

G_{mb} = Estimated bulk specific gravity, using sample dimensions and weight

G_{mm} = Measured theoretical maximum specific gravity of the asphalt mixture

Volumetric properties such as Voids in Total Mix (VTM), Voids in Mineral Aggregate (VMA), Voids Filled with Asphalt (VFA), and Percentage of effective asphalt (P_{be}) were determined using the relations provided in NCAT HMA Handbook (Brown et al. 2009).

5.2.1 Results and discussions

Table 5.4, Figure 5.1 and Figure 5.2 show the compaction data and the compaction curves for the loose mixtures SP5 and RG3, respectively. Because of the limited quantity available for the loose mixtures, only two samples could be prepared for each mixture. For each mixture, the compaction properties of the two replicates are similar, with almost identical compaction curves. The SP5 mixture is more compactable than RG3, since it has a higher % G_{mm} than RG3 at the same number of gyration.

Table 5.4 Compaction data for the loose mixtures SP5 and RG3

Number of gyration	Sample height, mm				%G_{mm}			
	Sample ID							
	SP5-1	SP5-2	RG3-1	RG3-2	SP5-1	SP5-2	RG3-1	RG3-2
1	135.2	135.4	136.7	136.4	82.6	82.5	80.4	80.6
2	132.2	132.3	133.6	133.3	84.5	84.5	82.3	82.5
3	130.3	130.4	131.7	131.3	85.8	85.7	83.5	83.8
4	128.9	129	130.2	129.9	86.7	86.6	84.5	84.7
5	127.7	127.8	129.1	128.8	87.5	87.4	85.2	85.4
6	126.1	126.9	128.2	127.9	88.6	88.0	85.8	86.0
7	126.1	126.2	127.4	127.1	88.6	88.5	86.3	86.5
8	125.4	125.6	126.8	126.5	89.1	89.0	86.7	86.9
9	124.9	125	126.2	125.9	89.5	89.4	87.1	87.3
10	124.4	124.5	125.7	125.4	89.8	89.7	87.5	87.7
20	121.3	121.5	122.6	122.4	92.1	92.0	89.7	89.8
30	119.7	120	121.1	120.8	93.3	93.1	90.8	91.0
40	118.7	119	120.1	119.8	94.1	93.9	91.6	91.8
50	118	118.2	119.3	119.1	94.7	94.5	92.2	92.3
60	-	-	118.8	118.5	-	-	92.6	92.8
70	-	-	118.3	118.1	-	-	93.0	93.1
80	-	-	117.9	117.7	-	-	93.3	93.4
90	-	-	117.6	117.4	-	-	93.5	93.7

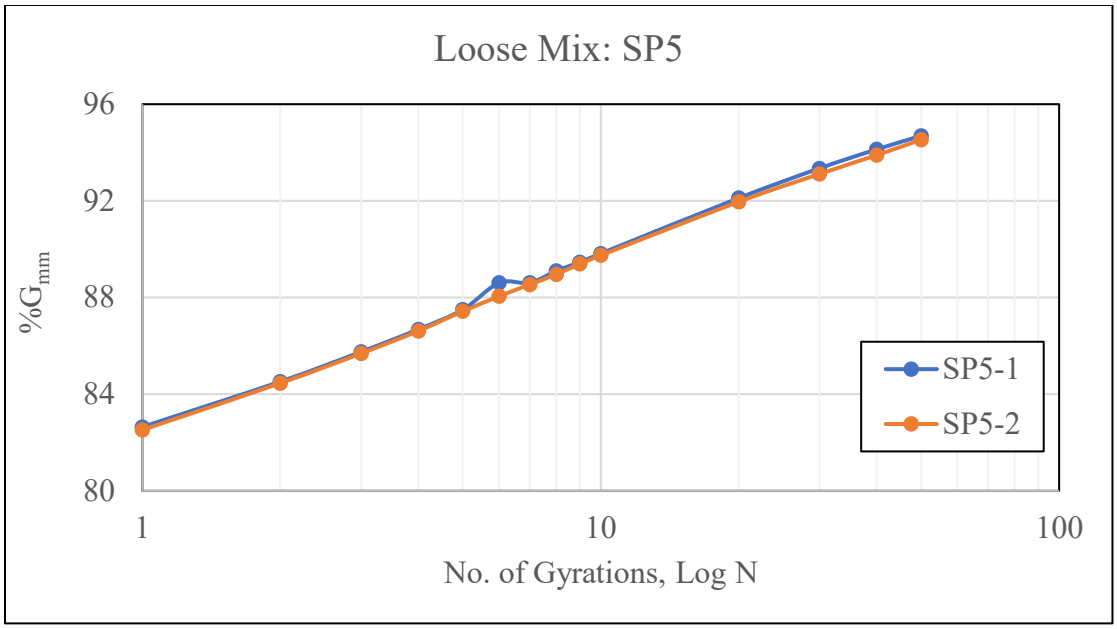

Figure 5.1 Compaction curve for SP5 mixture

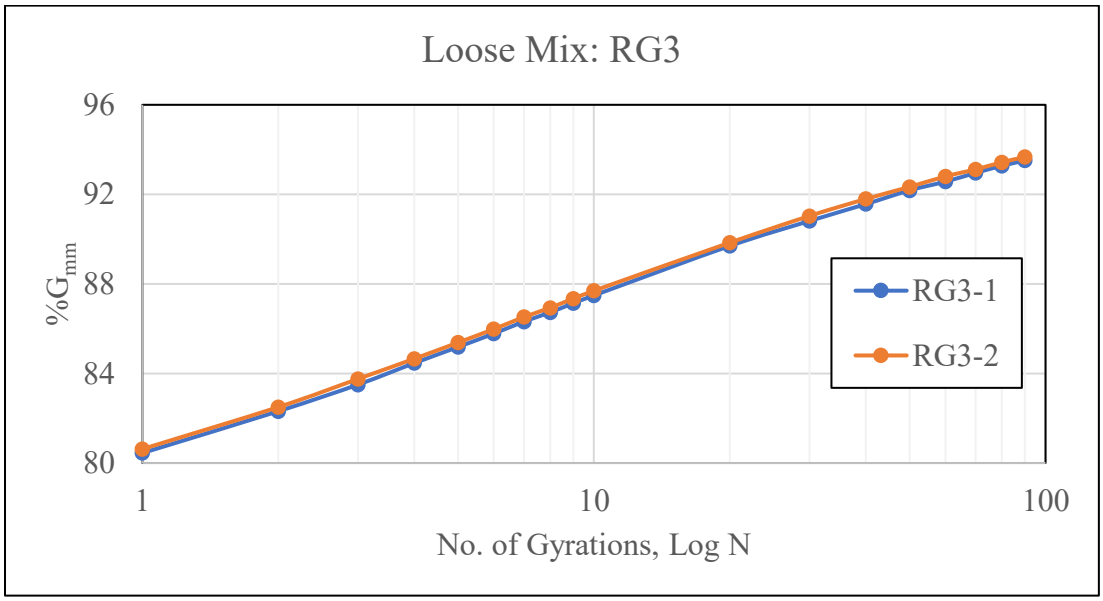

Figure 5.2 Compaction curve for RG3 mixture

Table 5.5 and Table 5.6 show the results of volumetric properties of mixtures SP5 and RG3 along with the results provided by the contractor and MnDOT for these mixtures. The SP5 mixture achieved around 3% air voids for a targeted 5% air voids, with a variation of approximately 2%. This is in agreement with the air voids percentage provided by the contractor and MnDOT. It is hypothesized that these mixtures were produced with a relatively high amount of asphalt content (6.9%) to reduce the air voids instead of

altering the aggregate mixture gradation. The mixture RG3 achieved the required target air voids of 3% with around 1% variation.

Table 5.5 Volumetric properties of mixture SP5

Mix Type	SP5		Reference Information		
Specimen ID	SP5-1	SP5-2	JMF	Contractor	MnDOT
G_{mm}	2.431	2.431	-	2.431	2.439
G_{mb}	2.358	2.354	-	2.358	2.637
G_b	1.03	1.03	-	-	-
P_b (% AC)	6.9	6.9	6.6	6.9	6.7
G_{sb}	2.65	2.65	-	-	-
P_s, %	93.1	93.1	-	-	-
G_{se}	2.704	2.704	-	-	-
P_{ba}, %	0.77	0.77	-	-	-
P_{be}, %	6.18	6.18	5.9	6.3	-
VTM, %	3.00	3.17	5.0	3.0	3.0
VMA, %	17.16	17.30	15.00	17.4	16.9
VFA, %	82.50	81.69	-	-	-

Table 5.6 Volumetric properties of mixture RG3

Mix Type	RG3		Reference Information		
Specimen ID	RG3-1	RG3-2	JMF	Contractor	MnDOT
G_{mm}	2.470	2.470	-	2.470	2.480
G_{mb}	2.360	2.375	-	2.388	2.384
G_b	1.03	1.03	-	-	-
P_b (% AC)	5.7	5.7	5.7	5.7	5.4
G_{sb}	2.649	2.649	-	-	-
P_s, %	94.3	94.3	-	-	-
G_{se}	2.698	2.698	-	-	-
P_{ba}, %	0.71	0.71	-	-	-
P_{be}, %	5.03	5.03	5	5.1	-
VTM, %	4.45	3.85	3.0	3.3	3.9
VMA, %	15.99	15.45	-	15.2	15.0
VFA, %	72.14	75.11	-	-	-

[G_{mb}-Bulk Density, G_b-Specific Gravity of Binder, P_b-% Binder in the Total Mix, P_s-% Aggregate, G_{se}-Effective Specific Gravity of Aggregate, G_{sb}-Bulk Specific Gravity of Aggregate, P_{ba}-% Absorbed Asphalt, P_{be}-% Effective Asphalt, VTM-Voids in Total Mix, VMA-Voids in Mineral Aggregate, VFA-Voids Filled with Asphalt]

Table 5.7 shows the results of individual gradations of the aggregates used for reproducing the Indiana's SP 5 mixtures, and Table 5.8 shows the final designed blended aggregate proportions for the reproduced SP5 (Rep. SP5) mixture. Table 5.9 and Figure 5.3 show the aggregate gradations of reproduced SP5 mixture and Indiana's SP5 mixture and the gradation charts, respectively. It can be seen in Figure 5.3

that the gradations of mixtures used in the current work matched well with the gradation of the Indiana's SP5 mixture.

Table 5.7 Individual gradations of aggregate material

Sieve Size, mm	Aggregates			
	½-inch CA	½- inch taconite	Rock fines	Natural sand
12.5	96.54	99.92	99.23	98.85
9.5	68.08	80.52	94.60	96.48
4.75	7.54	6.77	56.56	84.23
2.36	2.15	1.31	37.56	71.52
1.18	1.73	1.08	26.00	52.67
0.600	1.65	1.03	19.06	28.54
0.300	1.57	1.00	12.60	8.83
0.150	1.36	0.99	7.65	2.81
0.075	1.14	0.96	4.15	1.71

Table 5.8 Blended proportions of aggregates in the reproduced SP5 mixture

Aggregates	Proportions, %
Rep. SP5	
½-inch CA	11
½-inch taconite	12
Rock fines	39
Natural sand	38

Table 5.9 Gradations of the reproduced SP5 vs. Indiana's SP5 mixtures

Sieve Size, mm	Combined Aggregate Gradation	
	Rep. SP5	Indiana's SP5
12.5	98.9	100.0
9.5	90.7	95.6
4.75	55.7	60.1
2.36	42.2	38.1
1.18	30.5	24.6
0.600	18.6	16.1
0.300	8.6	9.5
0.150	4.3	5.3
0.075	2.5	4.0

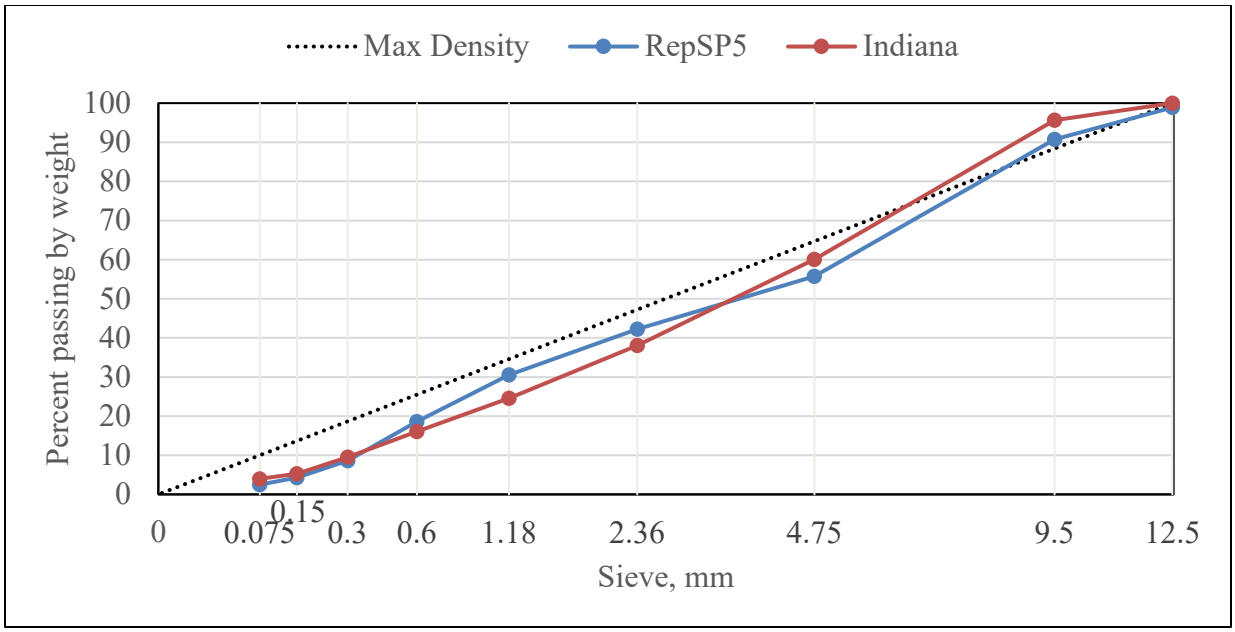

Figure 5.3 Gradation charts of the reproduced SP5 vs. Indiana's SP5 mixtures

Table 5.10 and Figure 5.4 show the data and plots of the compaction curve for the laboratory reproduced mixtures SP5. The plots indicate the similar sensitivity of compaction for both the samples of the reproduced SP5 mixture.

Table 5.10 Compaction data for Reproduced SP5 mixture

	Height, mm		% G_{mm}	
	Sample ID			
N	Rep. SP5-1	Rep. SP5-2	Rep. SP5-1	Rep. SP5-2
1	135.5	133.6	80.1	81.1
2	132.2	130.4	82.1	83.1
3	130	128.4	83.4	84.4
4	128.4	126.9	84.5	85.4
5	127.2	125.8	85.3	86.2
6	126.2	124.8	86.0	86.9
7	125.3	124.1	86.6	87.3
8	124.6	123.4	87.1	87.8
9	124	122.8	87.5	88.3
10	123.4	122.3	87.9	88.6
20	120	119	90.4	91.1
30	118.3	117.4	91.7	92.3
40	117.1	116.2	92.6	93.3
50	116.3	115.4	93.3	93.9

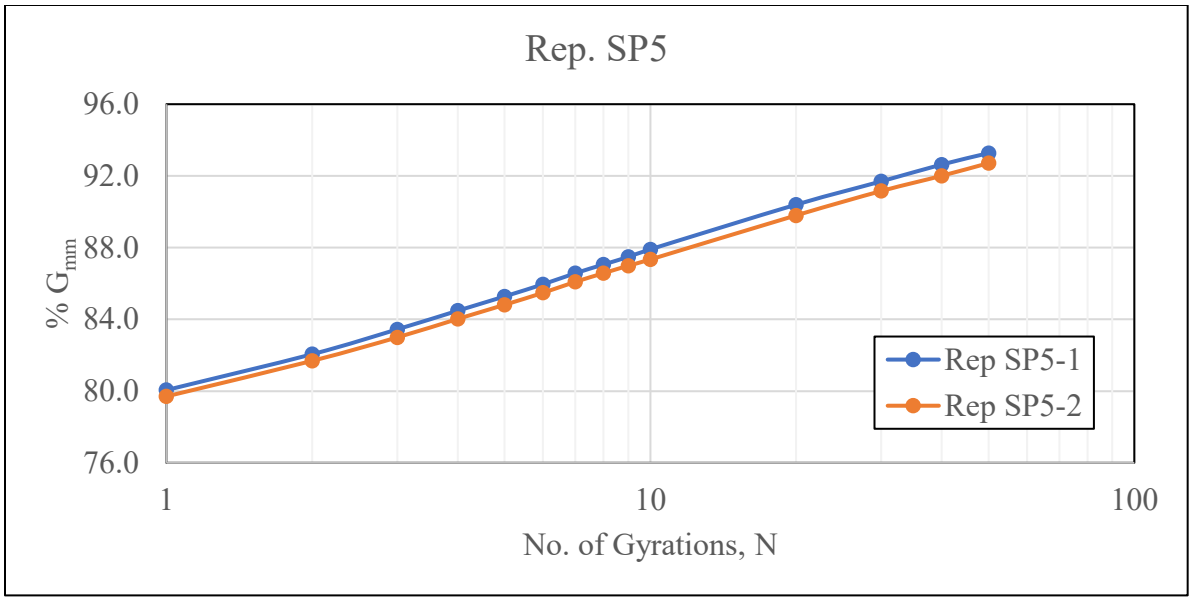

Figure 5.4 Compaction curves for Reproduced SP5 mixture

Table 5.11 shows the results of volumetric properties of reproduced SP5 mixture in comparison to Indiana's SP5 mixture. It can be seen that the reproduced SP5 mixture with the locally available material attained the required target air voids of 5% (similar to Indiana's SP5 mixture) with 0.3% less asphalt content than what was used for Indiana's SP5 mixture design (6%).

Table 5.11 Volumetric properties of Rep. SP5

Mix Type	Rep. SP5		Indiana's SP5_Cat3
Specimen ID	Rep SP5-1	Rep SP5-2	
G_{mm}	2.504	2.504	2.537
G_{mb}	2.391	2.380	-
G_b	1.03	1.03	-
P_b (%AC)	5.7	5.7	6.0
G_{sb}	2.72	2.72	2.692
P_s, %	94	94	-
G_{se}	2.756	2.756	-
P_{ba}, %	0.49	0.49	-
P_{be}, %	5.54	5.54	-
VTM, %	4.52	4.94	4.9
VMA, %	17.38	17.74	15.8
VFA, %	73.98	72.16	68.9

G_{mb} - Bulk Density, G_b - Specific Gravity of Binder, P_b - % Binder in the Total Mix, P_s - % Aggregate,

G_{se} - Effective Specific Gravity of Aggregate, G_{sb} - Bulk Specific Gravity of Aggregate,

P_{ba} - % Absorbed Asphalt, P_{be} - % Effective Asphalt, VTM - Voids in Total Mix,

VMA - Voids in Mineral Aggregate, VFA - Voids Filled with Asphalt

5.3 OTHER ASPHALT MIXTURES INVESTIGATED

For comparison purposes, six other asphalt mixtures, also used in the 2017 NRRA study at MnROAD, were investigated. These mixtures represent standard mix designs obtained by achieving 4% air voids in laboratory conditions at N_{design}, which is determined according to the traffic volume of the road. The nine mixtures investigated are shown in Table 5.12. As shown, the first five mixtures are standard mixtures designed at 4% air voids, but with different NMAS, N_{design} and asphalt content. The sixth mixture, D43, is a fracture resistant interlayer mixture, which has small NMAS (4.75 mm), the highest design asphalt content (8.2%), and lowest design air voids (2.5%). The last three are mixtures that can be field compacted at high densities, as introduced before.

Figure 5.5 shows the gradation curves. It can be seen that mixtures D44 and D43 have similar gradations and the smallest aggregates size, with NMAS = 4.75mm. Mixtures A44 and UMDSP5 have the second smallest aggregates size (NMAS = 9.5mm), but their gradations are quite different. A44 is more fine-graded, while UMDSP5 is more coarse-graded. The remaining mixtures, B34, B44, RG3, MnSP5, and C44, have quite similar gradation curves, though C44 has a larger NMAS of 19mm than the others.

Table 5.12: Asphalt mixture information

Mix ID	Mixture type	NMAS mm	N_{design}	Design air void %	Design asphalt content %
B34	Mix used for all LVR sections	12.5	60	4	5.3
A44	Cells 984, 987, 991-994, 9.5mm mix for surface and single lifts	9.5	90	4	5.8
B44	Cells 985, 986, 988, 12.5mm for surface and single lifts	12.5	90	4	5.4
C44	Cells 987-991 first lift	19	90	4	5.6
D44	Cells 201 and 215, 4.75mm thin layer	4.75	75	4	7
D43	Cell 992, interlayer mix	4.75	50	2.5	8.2
RG3	Cell 990, surface lift, 3% Regressed Air Void	12.5	90	3	5.7
MnSP5	Cell 989, Superpave 5, surface course	12.5	50	5	6.6
UMDSP5	UMD reproduced Indiana Superpave 5 mixture	9.5	50	5	5.7

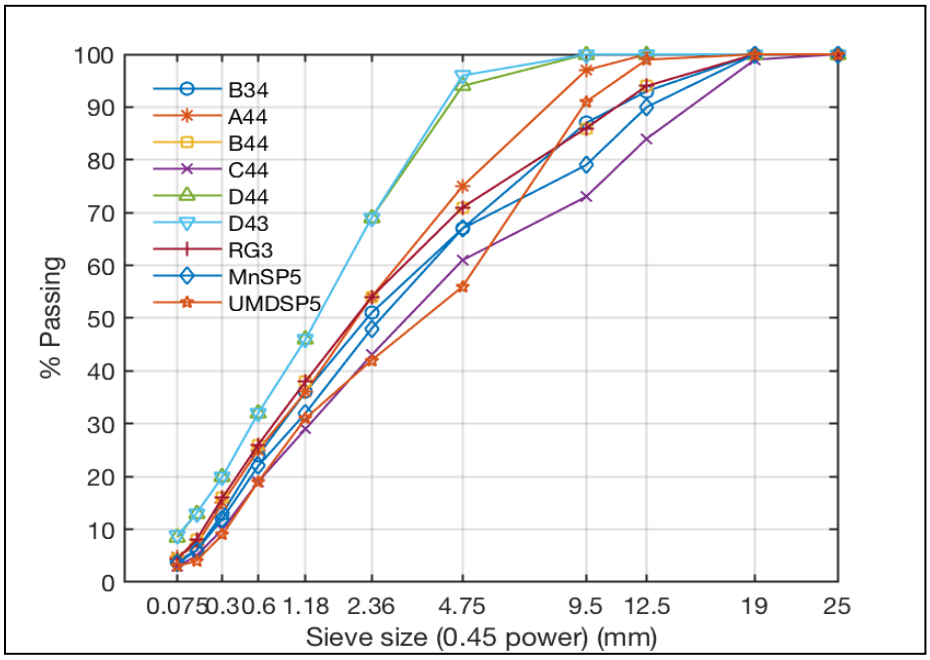

Figure 5.5: Gradation curves of mixtures

5.3.1 Sample Preparation

Asphalt mixture specimens were prepared in laboratory conditions using loose mix collected from MnROAD during the construction process. The loose mix were first heated to a workable condition followed by sampling the representative sample of 4800 gm by quartering method (*AASHTO R47-10, 2008*). The sampled loose mix was heated to the mixing temperature, thoroughly mixed, and then compacted at the design number of gyrations. Relevant volumetric information of the compacted specimens is shown in Table 5.13.

Table 5.13: Volumetric information of the mixtures

Mix ID	B34	A44	B44	C44	D44	D43	RG3	MnSP5	UMDSP5
Gmm	2.487	2.477	2.484	2.493	2.357	2.380	2.470	2.431	2.504
Gmb	2.367	2.335	2.363	2.294	2.254	2.268	2.323	2.268	2.385
VMA, %	15.6	17.1	15.7	18.4	21.2	21.7	17.4	20.3	17.3
Air voids, %	4.8	5.7	4.9	8.0	4.4	4.7	5.9	6.7	4.8

5.4 TESTING METHODS AND RESULTS

The following experiments were conducted: Bending Beam Rheometer (BBR) Creep and Strength, Indirect Tensile (IDT) Creep, Diametral Dynamic Modulus (E*), Semi-Circular Bending (SCB), Uniaxial Dynamic Modulus (E*), and Flow Number (FN). The experimental matrix is shown in Table 5.14.

The BBR creep and strength tests were conducted on the same specimen, sequentially. Each mixture was tested at three temperatures, and at each temperature, six replicates were tested. The IDT creep test was performed at -12℃, and two replicates were tested for each mixture. The diametral E* test was performed at three different temperatures and eight frequencies in order to obtain |E*| master curves. Each mixture was tested using three replicates, except for mixture UMDSP5, for which only two replicates were available. For SCB test, three replicates were tested for each mixture at each temperature level. The high-density mixtures were tested at two temperatures and the standard mixtures were tested only at -21˚C. The standard Dynamic Modulus test and Flow Number test were performed only on the high-density mixtures, using three replicates.

Table 5.14: Experimental matrix

Mixture ID	Number of replicates								
	BBR Creep and Strength			IDT Creep	Diametral E*	SCB		Uniaxial E*	Flow Number
	-24°C	-12°C	0°C	-12°C	-12, 6, 24°C	-21°C	-12°C	4, 20, 35°C	49°C
B34	6	6	6	2	3	3	0	0	0
A44	6	6	6	2	3	3	0	0	0
B44	6	6	6	2	3	3	0	0	0
C44	6	6	6	2	3	3	0	0	0
D44	6	6	6	2	3	3	0	0	0
D43	6	6	6	2	3	3	0	0	0
RG3	6	6	6	2	3	3	3	3	3
MnSP5	6	6	6	2	3	3	3	3	3
UMDSP5	0	0	0	2	2	3	3	3	3

5.4.1 Bending Beam Rheometer (BBR) Creep and Strength Test

Each mixture beam was tested under a combined procedure that included an initial BBR creep test (AASHTO TP125-16), followed by a recovery period and a strength test (Marasteanu et al., 2012) without removing the beam from the testing frame. The creep test had a duration of 500 second selected to ensure that the individual temperature results overlap when shifted to create master curves.

Creep tests followed by recovery and strength tests were performed at three temperatures for each cell: 0°C, -12°C and -24°C. The creep loading was chosen to be 2N, 4N and 6N for testing at 0°C, -12°C and -24°C, respectively, to be able to measure the small deflection values obtained in mixture testing. The creep test was followed by a recovery of 500 seconds, using a very small seating load that allowed measuring the recovery deflection. At the end of the recovery period, a strength test was performed using a constant loading rate that was selected such that a load of 44N was obtained in 60 sec. The test ended when the beam broke.

Six replicates were tested and the average and coefficient of variation were calculated. Table 5.15 lists the average and the coefficient of variation (CV) of the BBR creep stiffness and m-value. The results of the strength tests are listed in Table 5.16.

Table 5.15: Creep stiffness and m-value results of the BBR Creep test

Mix ID	Temperature °C	S @ 60s, GPa		m-value @ 60s	
		AVG	CV %	AVG	CV %
B34	0	1.53	41	0.314	15
	-12	4.71	30	0.176	14
	-24	7.50	22	0.076	24
A44	0	1.55	14	0.355	3
	-12	4.28	37	0.161	22
	-24	9.71	16	0.074	19
B44	0	1.15	3	0.373	7
	-12	4.89	11	0.201	6
	-24	12.58	18	0.125	9
C44	0	1.01	18	0.413	11
	-12	3.00	47	0.225	10
	-24	8.40	17	0.088	11
D44	0	0.92	20	0.399	6
	-12	2.63	41	0.189	20
	-24	5.81	57	0.076	36
D43	0	1.55	12	0.298	7
	-12	3.78	12	0.163	9
	-24	7.45	22	0.079	16
RG3	0	1.24	26	0.403	9
	-12	3.88	18	0.220	7
	-24	8.28	17	0.083	14
MnSP5	0	0.99	14	0.451	4
	-12	3.61	13	0.260	5
	-24	7.83	17	0.095	15

Table 5.16: Failure strength and strain results of the BBR strength test

Mix ID	Temperature °C	Failure strength, MPa		Failure strain	
		AVG	CV %	AVG	CV %
B34	0	8.6	8.6	0.70	37
	-12	7.2	8.6	0.22	82
	-24	9.2	8.3	0.10	60
A44	0	9.3	9.3	0.70	17
	-12	11.1	9.5	0.17	26
	-24	9.6	8.4	0.06	14
B44	0	9.7	9.1	1.14	37

	-12	10.5	10.6	0.19	10
	-24	10.6	8.8	0.16	173
C44	0	8.5	7.4	0.81	32
	-12	8.7	6.0	0.14	20
	-24	6.9	6.6	0.13	117
D44	0	8.3	9.6	1.28	18
	-12	10.0	11.8	0.35	20
	-24	11.0	10.8	0.19	63
D43	0	7.7	9.1	0.76	8
	-12	9.3	11.0	0.25	13
	-24	9.0	9.8	0.17	82
RG3	0	7.9	8.2	0.76	29
	-12	8.3	8.6	0.19	24
	-24	8.9	7.5	0.07	13
MnSP5	0	8.5	7.2	0.76	26
	-12	8.5	8.2	0.19	16
	-24	6.2	6.4	0.06	12

The creep stiffness and m-value results are also plotted in Figure 5.6 and Figure 5.7, respectively. For all mixtures, as the temperature increase, the creep stiffness decreases while the m-value increases. The rankings based on creep stiffness and on m-value remain almost unchanged at all temperature levels.

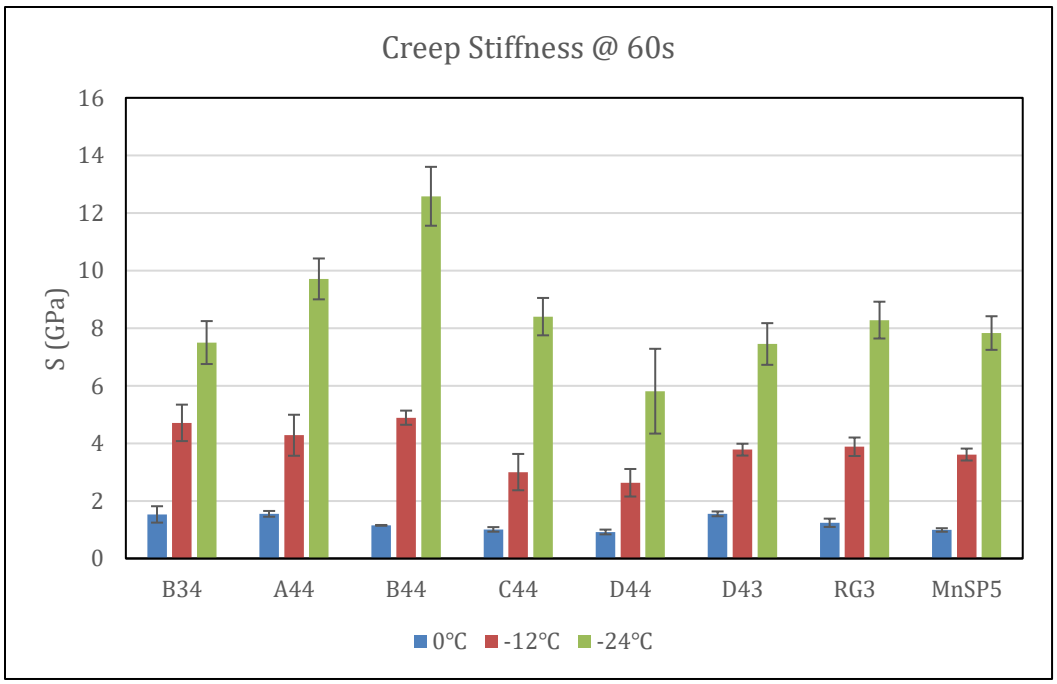

Figure 5.6: BBR creep stiffness at 60 seconds

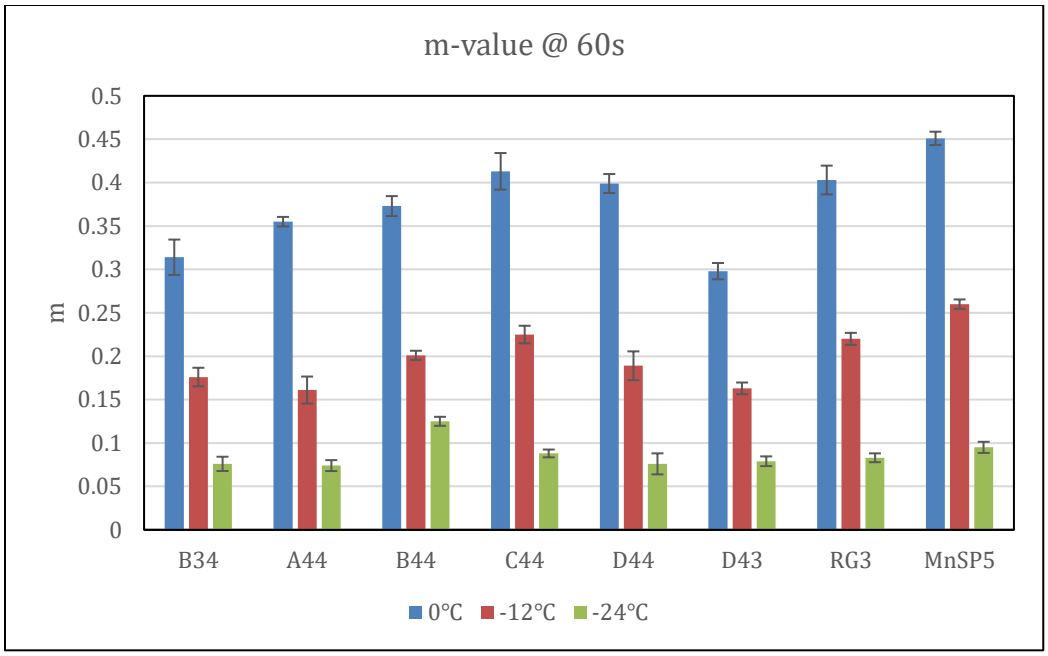

Figure 5.7: BBR m-value at 60 seconds

Figure 5.8 and Figure 5.9 show the failure strength and strain of mixtures at different temperatures. For all mixtures, except C44, the strength reaches a maximum at -12 ℃, while the strain at failure shows a consistent trend of increasing with increase in temperature.

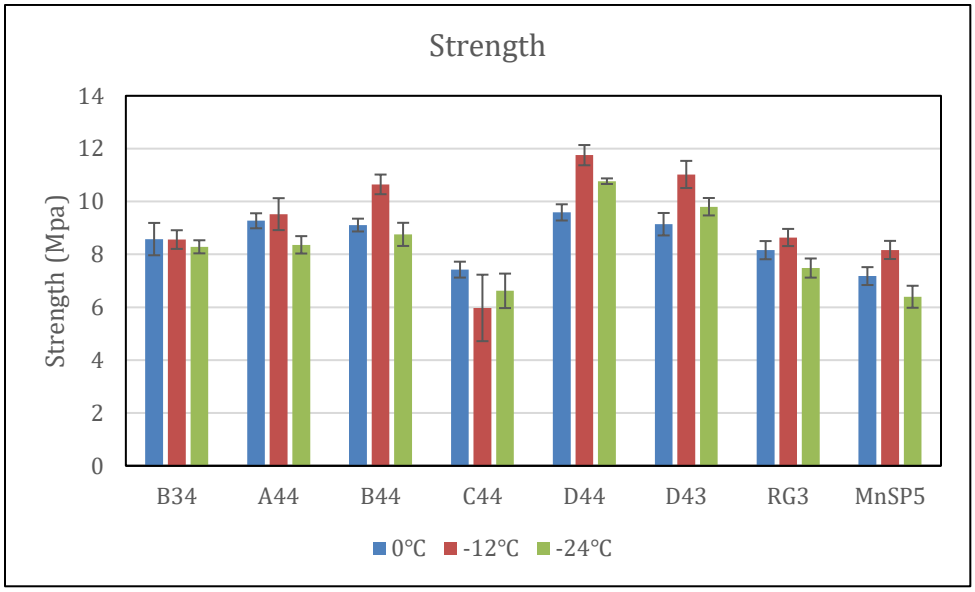

Figure 5.8: BBR strength of different mixtures

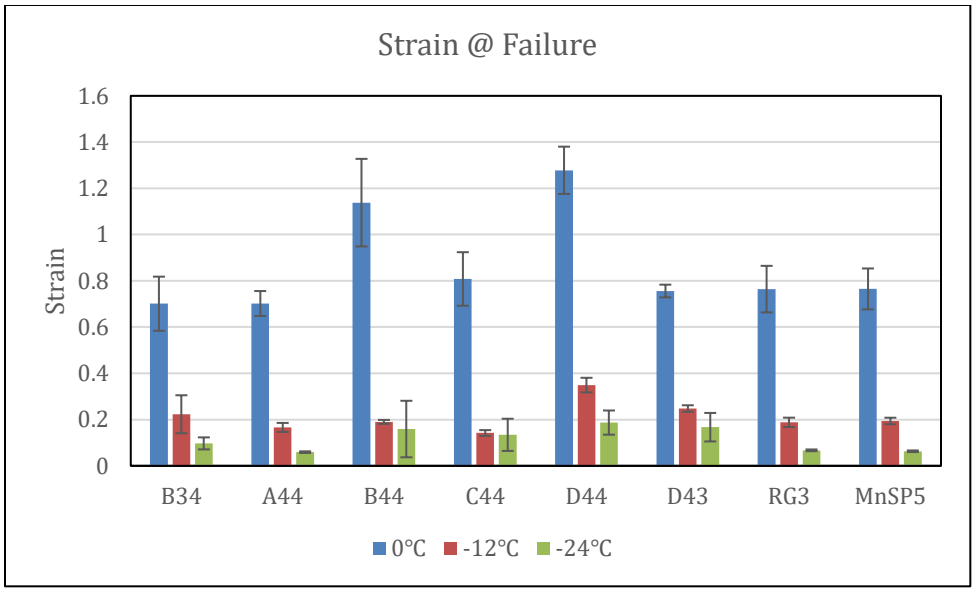

Figure 5.9: BBR strain at failure of different mixtures.

5.4.2 Indirect Tensile (IDT) Creep Test

Creep and tensile strength tests followed procedures outlined in "Standard Test Method for Determining the Creep Compliance and Strength of Hot Mix Asphalt (HMA) Using the Indirect Tensile Test Device," AASHTO T322 -07 (2007). Two replicates were tested for each material at -12°C. Table 5.17 shows the results of S @ 60s and S @ 500s in IDT creep tests.

Table 5.17: Creep Stiffness results of IDT creep test

MIX ID	Temperature	S @ 60s, GPa		S @ 500s, GPa	
		AVG	CV, %	AVG	CV, %
B34	-12	13.83	7.0	7.64	0.3
A44	-12	8.08	1.3	4.93	1.8
B44	-12	7.31	12.4	4.49	0.5
C44	-12	8.38	3.2	4.51	3.3
D44	-12	6.77	3.2	3.72	0.6
CR	-12	7.68	7.6	4.59	12.5
RG3	-12	8.83	8.6	4.76	4.4
MnSP5	-12	5.46	16.8	2.78	18.0
UMDSP5	-12	7.83	10.1	4.66	7.6

Figure 5.10 shows Creep Stiffness at 60 and 500 seconds. It can be seen S @ 60s and S @ 500s have the same ranking for different mixtures. For different mixtures the ratios between S @ 500s and S @ 60s remain consistent, ranging from 0.5 to 0.6.

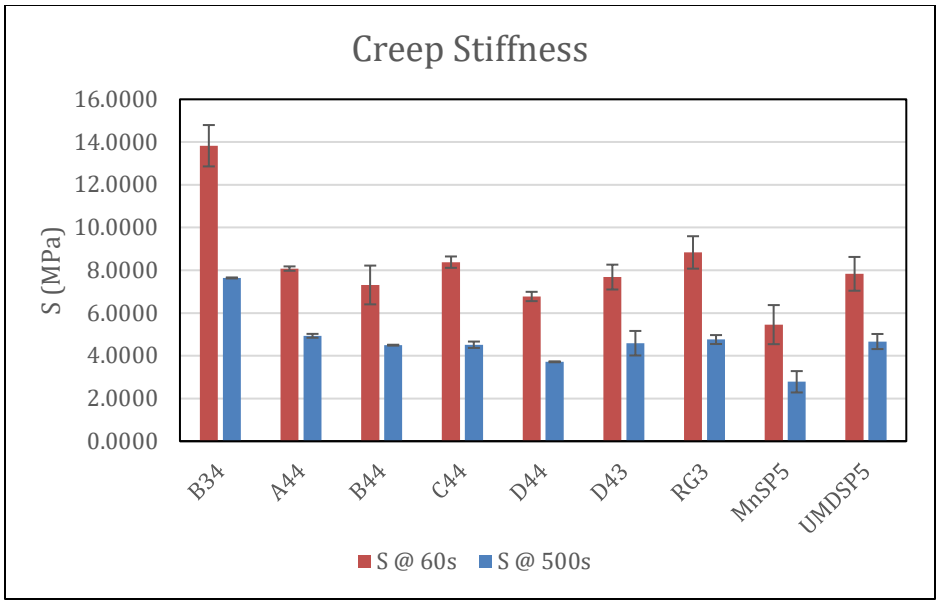

Figure 5.10: IDT Creep Stiffness results

5.4.3 Diametral Dynamic Modulus Test

Dynamic modulus is typically measured in compression on cylinders 100 mm in diameter and 170 mm tall (AASHTO TP 62-03, 2006). This geometry severely limits the possibility of testing field cores. An alternative method, based on the indirect tension (IDT) loading mode, described by Kim et al. (2004), was used. Frequency sweeps using eight frequencies were performed at 3 temperatures: -12°C, 6°C, and 24°C. Three replicates were tested, except for UMDSP5 which had two replicates. Average |E*| values were calculated and were then used to construct master curves using time-temperature superposition principle. Table 5.18 lists the results.

Table 5.18: Diametral dynamic modulus results, the average of |E*|

Mix ID	Temperature °C	AVG of |E*|, (GPa)							
		25 Hz	10 Hz	5 Hz	1 Hz	0.5 Hz	0.1 Hz	0.05 Hz	0.01 Hz
B34	-12	20.878	16.445	15.255	13.969	12.500	11.283	10.232	7.114
	6	10.997	9.387	8.525	6.620	5.985	4.243	3.730	2.024
	24	4.028	2.375	2.278	1.151	0.935	0.494	0.409	0.206
A44	-12	18.268	10.259	8.214	7.276	6.223	6.025	5.643	4.892
	6	8.523	8.130	7.394	5.793	5.127	3.697	2.875	1.801
	24	2.678	2.631	2.140	1.080	0.852	0.434	0.357	0.180
B44	-12	19.427	12.890	10.520	9.234	7.998	7.606	7.060	6.139
	6	9.621	9.396	8.579	5.909	5.546	3.605	2.882	1.288
	24	3.443	3.048	2.535	1.508	1.181	0.654	0.524	0.283
C44	-12	15.578	9.436	7.772	6.708	5.810	5.444	5.005	4.153
	6	7.842	7.287	5.909	4.490	3.945	2.460	1.957	0.862
	24	2.956	2.306	1.831	0.939	0.739	0.429	0.367	0.204

D44	-12	18.065	12.986	11.558	10.154	9.388	8.288	7.709	5.993
	6	7.744	8.018	6.573	4.934	4.269	2.481	2.061	0.915
	24	2.889	2.461	1.926	1.009	0.803	0.398	0.315	0.175
CR	-12	16.560	11.051	10.581	8.854	8.028	7.855	7.408	6.247
	6	8.981	8.207	7.417	6.099	5.298	3.667	3.090	1.619
	24	3.395	2.883	2.433	1.369	1.099	0.568	0.286	0.133
RG3	-12	16.806	10.758	8.588	7.763	6.808	6.515	6.046	5.199
	6	4.470	4.629	4.424	3.339	2.684	1.867	1.599	0.925
	24	4.050	3.719	3.405	1.707	1.361	0.718	0.613	0.328
MnS P5	-12	14.977	7.475	5.843	4.931	4.138	3.847	3.531	2.850
	6	7.743	7.106	6.127	4.071	3.387	1.875	1.413	0.502
	24	2.380	1.961	1.517	0.670	0.503	0.238	0.191	0.091
UM NSP 5	-12	14.866	11.269	10.243	8.703	8.236	7.855	7.255	5.752
	6	5.561	6.386	5.716	4.439	3.875	2.506	2.050	0.912
	24	2.074	1.995	1.700	0.895	0.696	0.348	0.275	0.152

The Dynamic Moduli at different temperatures were fitted to a master curve by using time-temperature superposition principle. The refrenced temperature is 6°C. Figure 5.11 summarizes the master curves of the nine mixtures. As shown in Figure 5.11, B34 mixture has the highest dynamic modulus, while MnSP5 mixture has the lowest. Notably, the mix A44 seems has a more desirable master curve, because it is less frequency (temperature) susceptible. It has a relatively high E* at high temperature (low frequency) to resistant rutting, while at low temperature (high frequency) E* is relatively low and most likely less brittle to help preventing cracking.

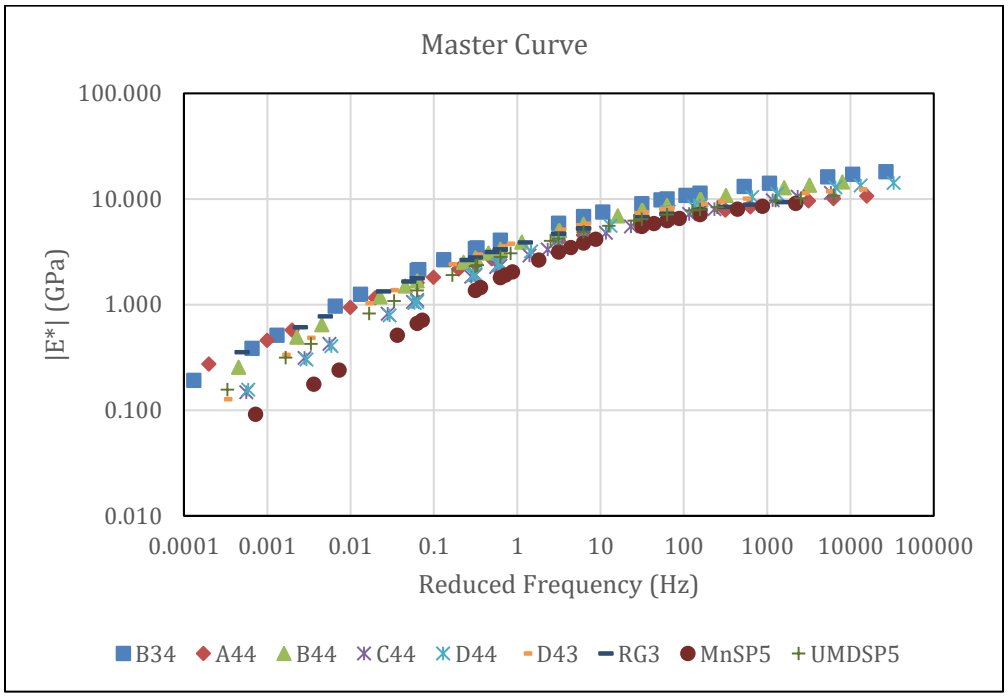

Figure 5.11: Results of dynamic modulus

5.4.4 Semi-Circular Bending (SCB) Test

The Semi-Circular Bending (SCB) fracture tests was performed according to AASHTO TP-105 (AASHTO TP105, 2013). All mixtures were tested at two temperatures, -21°C, and -12°C, using three replicates. The results of SCB fracture energy and fracture toughness at -21°C are presented in Table 5.19. Table 5.20 shows the results at -12°C, which only preformed on high-density mixtures.

Table 5.19: Results of SCB test at -21°C.

MIX ID	Temperature °C	G_f (J/m^2)		K_{IC} (MPa*m^0.5)	
		AVG	COV, %	AVG	COV, %
B34	-21	0.36	17	0.67	6
A44	-21	0.37	14	0.71	2
B44	-21	0.39	20	0.64	27
C44	-21	0.52	15	0.66	4
D44	-21	0.43	3	0.76	2
CR	-21	0.52	4	0.76	8
RG3	-21	0.36	4	0.61	6
MnSP5	-21	0.44	12	0.56	11
UMDSP5	-21	0.44	9	0.71	11

Table 5.20: Results of SCB test at -12 °C.

MIX ID	Temperature °C	G_f (J/m^2)		K_{IC} (MPa*m^0.5)	
		AVG	COV, %	AVG	COV, %
RG3	-12	0.76	11	0.61	1
MnSP5	-12	0.84	5	0.5	9
UMDSP5	-12	0.65	11	0.62	9

Fracture energy and toughness results at -21°C are also shown in Figure 5.12 and Figure 5.13, respectively. The energy ranges from 0.36 to 0.52 J/m^2, while toughness ranges from 0.56 to 0.76 MPa*m^0.5.

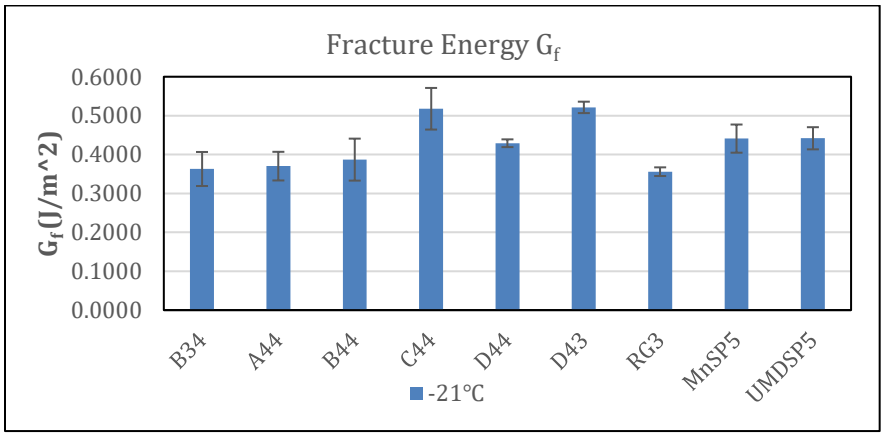

Figure 5.12: Fracture energy of different mixtures at -21°C.

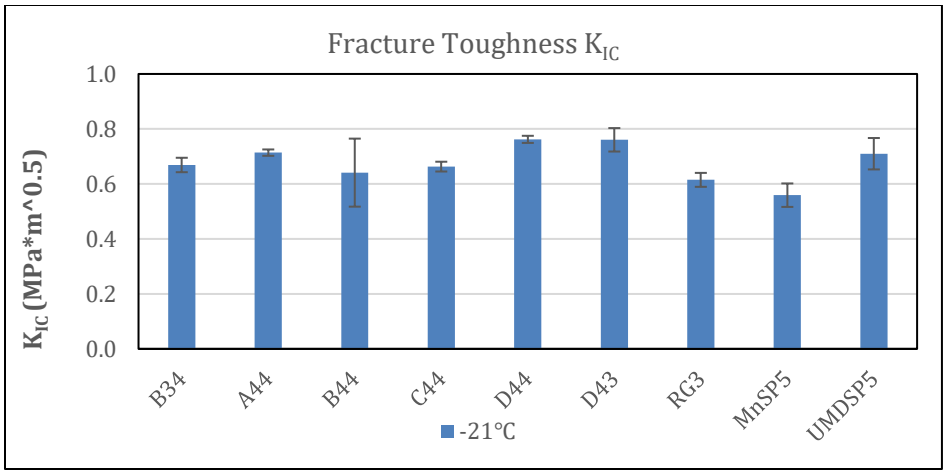

Figure 5.13: Fracture toughness of different mixtures at -12°C.

For the high-density mixtures, the SCB tests were performed also at -12°C. The results are compared in Figure 5.14 and Figure 5.15 for fracture energy and fracture toughness respectively.

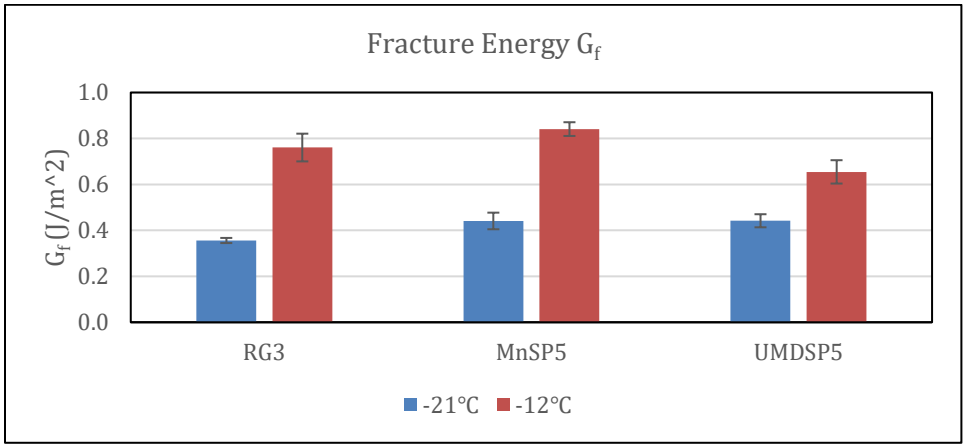

Figure 5.14: Fracture energy at -21 °C and -12 °C for high-density mixtures.

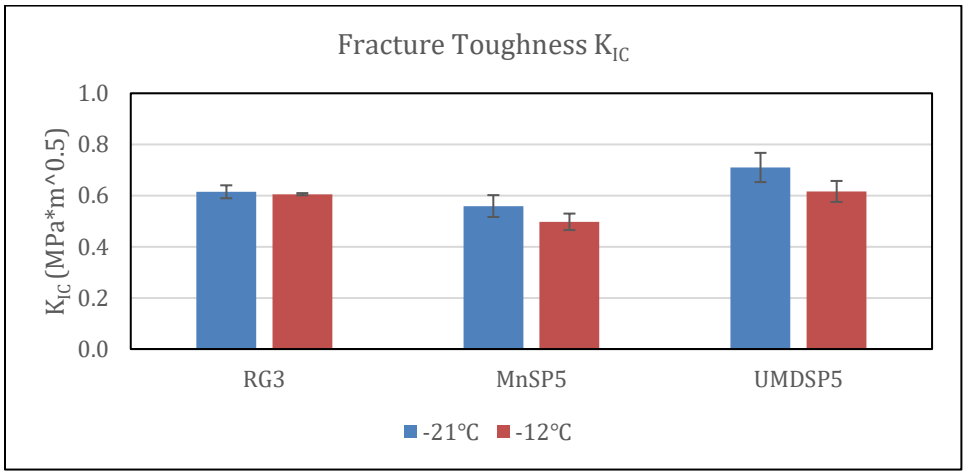

Figure 5.15: Fracture toughness at -21°C and -12°C for high-density mixtures.

For all mixtures, the fracture energy increases with temperature, while the fracture toughness decreases with temperature. MnSP5 has the highest fracture energy, while UMDSP5 has the highest fracture toughness, among the three high-density mixtures.

5.4.5 Dynamic Modulus (|E*|) and Flow Number (FN) Test

Dynamic modulus (E*) and Flow Number (FN) tests (*AASHTO T 378, 2017*) were conducted at University of Minnesota Duluth to determine the mechanical properties of the asphalt mixtures. While the E* determines the mixture stiffness, the FN characterize the resistance of the asphalt mixture to permanent deformation.

The E* test was conducted at three temperatures - 4, 20 and 35°C. Prior to testing, the specimens were conditioned in an environmental chamber; a dummy asphalt mixture specimen was used to monitor the test temperature. The FN test was conducted at 49°C. This temperature corresponds to the 7-day maximum pavement temperature 20 mm from the pavement surface at a 50% reliability, determined using the LTPPBind software (Appendix X2.3.1 of AASHTO T 378-17). The FN test was conducted on the same specimens used for the dynamic modulus testing, since dynamic modulus test is considered non-destructive. Table 5.21 summarizes the testing performed.

Table 5.21: Protocol for Dynamic Modulus and Flow Number tests

Dynamic Modulus	
Temperature, °C	Frequency, Hz
4	10, 1, 0.1
20	10, 1, 0.1
35	10, 1, 0.1, 0.01
Flow Number	
Test temperature	49°C
Repeated axial stress	600 kPa
Contact Stress	30 kPa
Confining Stress	0 kPa (unconfined)

Figure 5.16 and Figure 5.17 show the results of dynamic modulus (E*) for all the three mixtures. As anticipated, the values of the E* of all the mixtures significantly decreased as the testing temperature increased and as the loading frequency decreased. The mixture RG3 with lower air voids of 3% showed the highest E* followed by SP5 and Rep.SP5 mixtures with 5% air voids. Note, in this section, the SP5 and Rep. SP5 represent MnSP5 and UMDSP5 repectively.

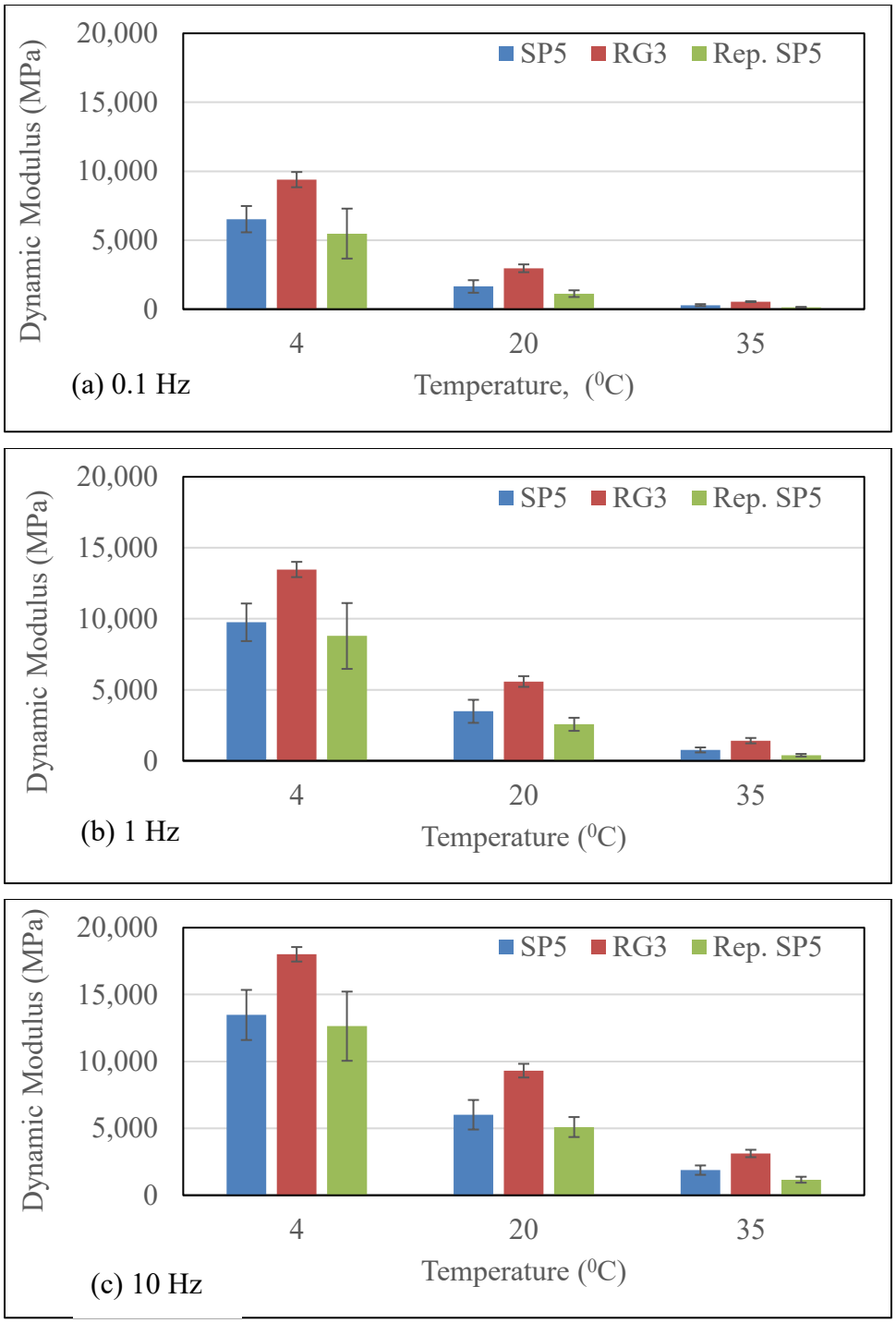

Figure 5.16: Dynamic Modulus results at: (a) 0.1 Hz (b) 1 Hz (c) 10 Hz

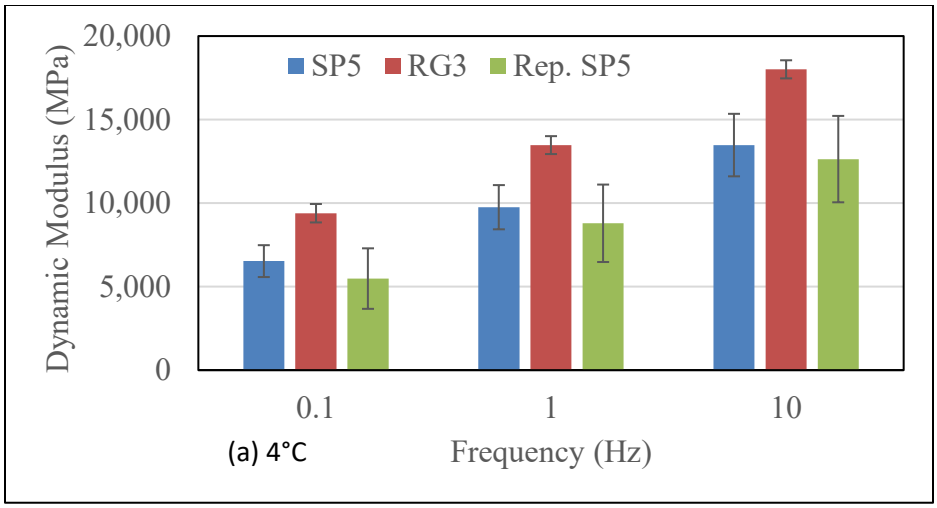

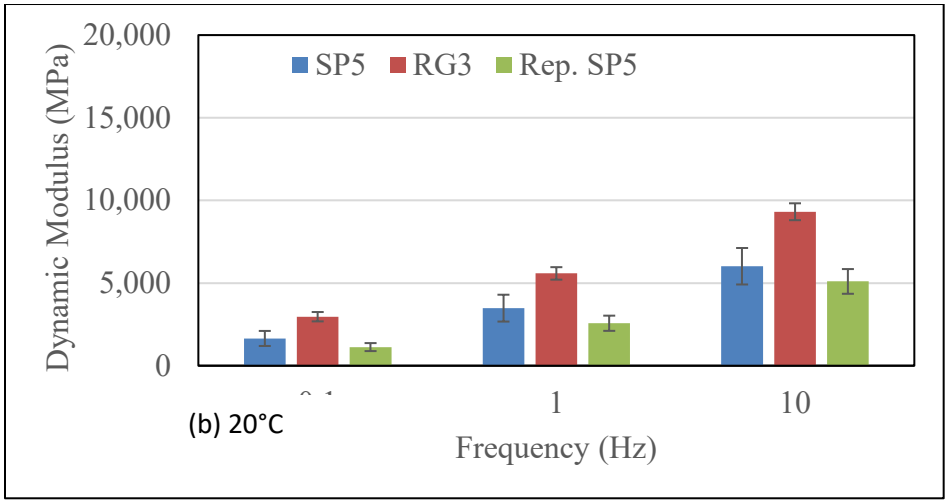

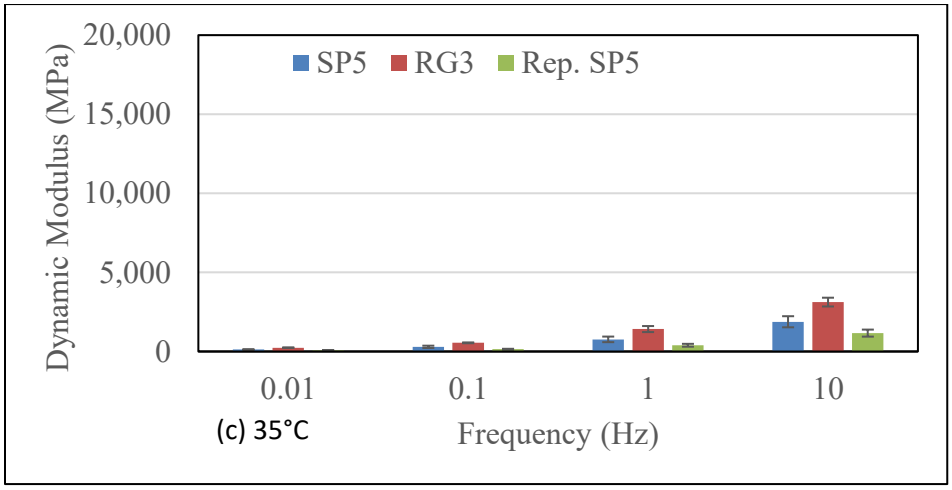

Figure 5.17: Dynamic Modulus results at: (a) 4°C (b) 20°C (c) 35°C

Figure 5.18 shows the dynamic modulus master curves constructed at a reference temperature of 20°C for all the three mixtures used in this study. It can be seen that, at the higher frequency, all mixtures

showed almost identical dynamic moduli, whereas, at lower frequency, the RG3 mix showed higher moduli than the SP5 mixes. The Rep.SP5 mixture (Reproduced Indiana mixture) had lower E* than the SP5 (MnROAD's mixture).

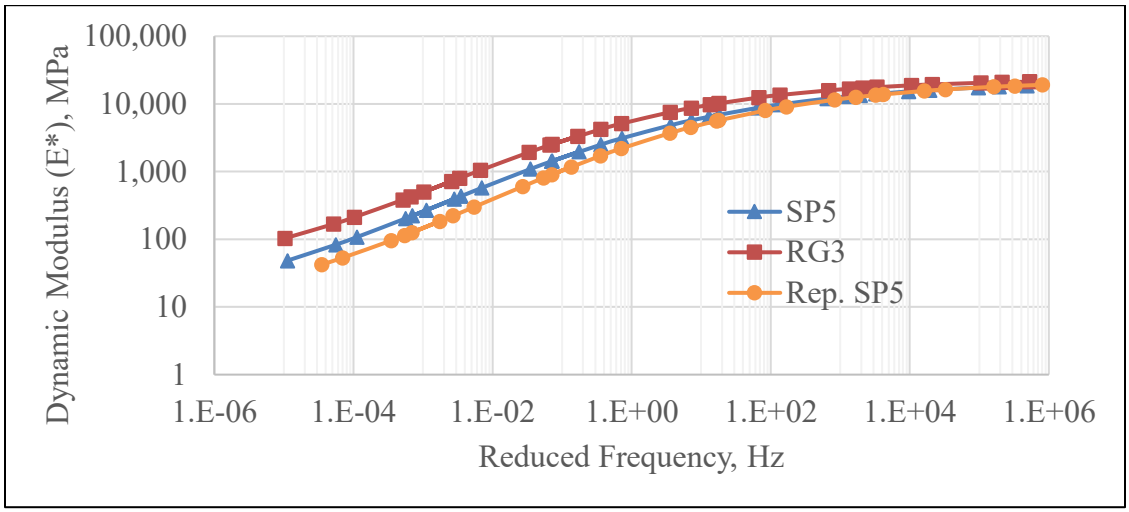

Figure 5.18: Dynamic Modulus Master Curve

Uniaxial E* results are also compared with the Diametral E* results (as shown in Figure 5.11) for the high-density mixtures. RG3 has the greatest dynamic modulus in both the tests, while MnSP5 and UMDSP5 rank differently in the two tests. Several possibilities can cause this difference. First, this two test are done in different material directions, with Uniaxial E* done in the vertical material direction, while IDT E* in the horizontal material direction. The differences we observed will be reasonable, if the asphalt material we tested is anisotropic. Secondly, the difference between MnSP5 and UMDSP5 could also be the randomness of different tests, providing that the difference is not large and the later-on statistics analysis also shows no significant difference between the E* of UMDSP5 and MnSP5.

Figure 5.19 shows the results of Flow Number (FN) tests for all the three mixtures. The mixture RG3 (~3% air voids) has the highest FN as expected, which indicates a greater resistance to permanent deformation. Between SP5 and Rep. SP5 mixtures, the SP5 showed higher FN than the Rep.SP5 mixture.

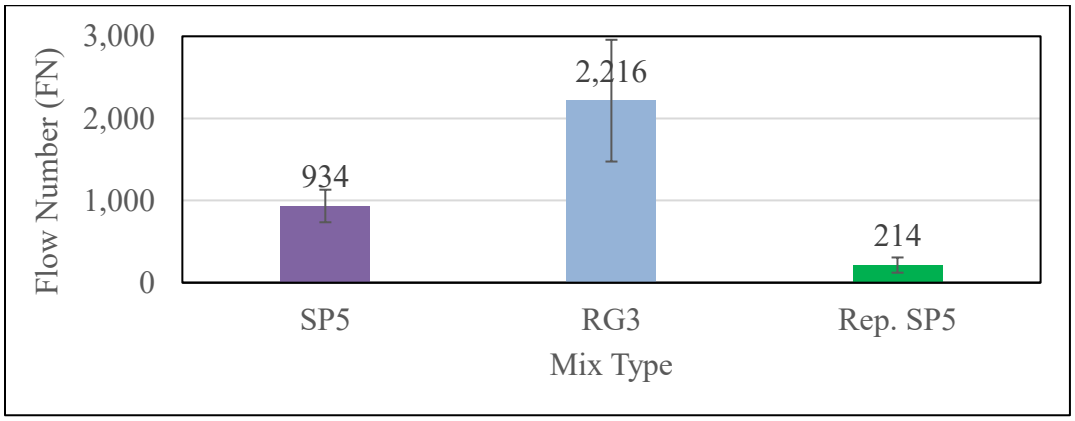

Figure 5.19: Results of Flow Number (FN) test

5.5 DATA ANALYSIS

In this section, we performed statistical analyses to compare the tests results between different mixtures, and to identify significant factors. The tools used include analysis of variance (ANOVA), and Tukey's method. Analysis of variance (ANOVA) is used to determine whether there are significant differences between different groups. To detect significant pairs, Tukey analysis is performed.

We performed one-way ANOVA on all test results. The significance level (α) was set at 0.05. The null hypothesis (H_0) assumed that all the means of tests results of different mixtures are equal. The alternate hypothesis (H_a) is that: at least one of mixture has the different mean compared with others. If the result of ANOVA analysis gives p-value > 0.05, then we should accept the null hypothesis that there is no significant difference between different mixtures. On the Contrary, if p-value < 0.05, we should reject the null hypothesis, which means there exists significant difference between mixtures.

We also perform Tukey analysis, which represents a pairwise comparison technique that constructs simultaneous confidence intervals for differences of all pairs of means and controls the probability of making one or more Type I errors (Oehlert, 2000). Based on the pairwise comparison results of Tukey analysis, one can further group and rank the mixtures.

5.5.1 Analysis of BBR Creep Stiffness Results

Table 5.22, Table 5.23, and Table 5.24 show the one-way ANOVA analysis of BBR creep stiffness results at 0, -12 and -24℃, respectively.

Table 5.22: ANOVA analysis of BBR creep stiffness results at 0℃

Source of Variation	SS	df	MS	F	P-value
Between Groups	3012100.34	7	430300.05	4.23	1.41E-03
Within Groups	4067647.98	40	101691.20		
Total	7079748.32	47			

Table 5.23: ANOVA analysis of BBR creep stiffness results at -12 ℃

Source of Variation	SS	df	MS	F	P-value
Between Groups	25642410.98	7	3663201.57	2.74	2.02E-02
Within Groups	53493874.12	40	1337346.85		
Total	79136285.10	47			

Table 5.24: ANOVA analysis of BBR creep stiffness results at -24 ℃

Source of Variation	SS	df	MS	F	P-value
Between Groups	1.68E+08	7	23978159.49	5.36	2.21E-04
Within Groups	1.79E+08	40	4477186.74		
Total	3.47E+08	47			

The p-values are all less than the significant level of 0.05. Therefore, at all temperature levels, the results of BBR creep stiffness have significant difference between mixtures.

Tukey analysis is performed to further detect specific difference between mixtures. The results of the three temperature levels are shown in Figure 5.20, Figure 5.21, and Figure 5.22, respectively. As shown in the (a) part of these figures, if the pairwise confidence interval intersect with zero, that means the pair do not have significant difference; if the interval larger than zero, that means the value of the first mixture of the pair is significantly larger than the second mixture of the pair. On the contrary, if the interval is smaller than zero, values of the second mixture are significantly larger than that of the first mixture of the pair. Based on the pairwise comparison results, the mixtures are ranked and grouped by the compact letter display (CLD) method (as shown in the part (b) of Figure 5.20, Figure 5.21, and Figure 5.22). The alphabetical order of letter grouping shows the ranking of the mixtures. Groups sharing same letters do not have significant difference. By contrast, groups with different letter are significantly different from each other (*Piepho, 2004*).

As shown in Figure 5.20, Figure 5.21, and Figure 5.22, creep stiffness of D44 shows a consistent tendency of significantly smaller than other mixtures at all temperature levels. At 0°C, D44 is significantly smaller than B34, A44, and D43. At -12°C, D44 is significantly smaller than B44. At -24°C, D44 is significantly smaller than B44 and A44. In terms of the high-density mixtures, RG3 and MnSP5, no significant differences are found between them and other mixtures.

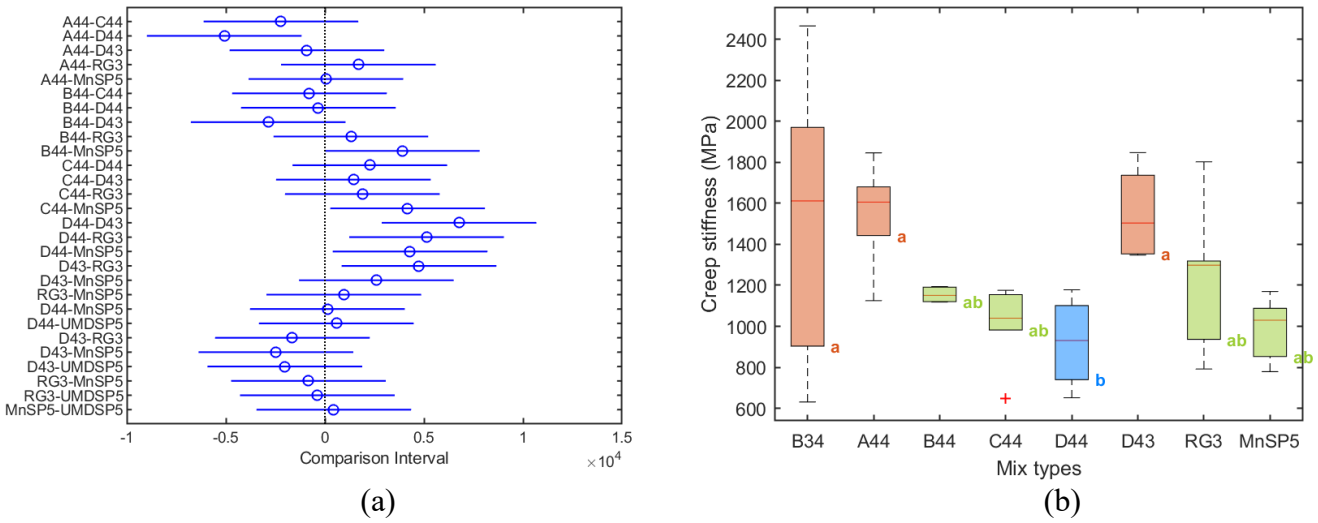

Figure 5.20: Tukey analysis of BBR creep stiffness at 0°C. (a): confidence interval of the pairwise comparison. (b): boxplot of results with letter grouping.

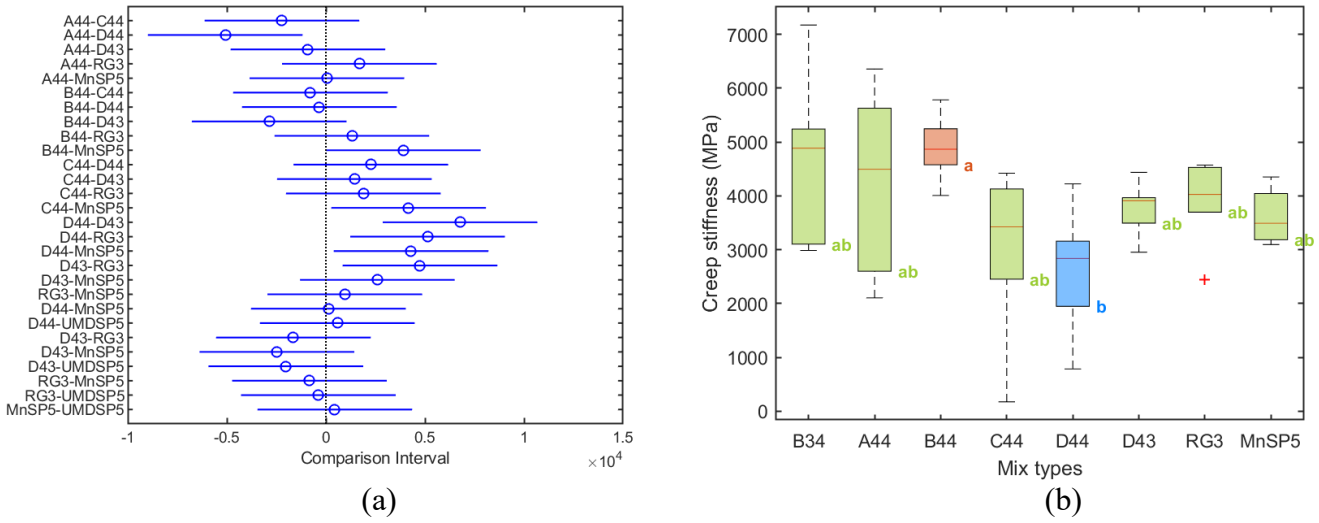

Figure 5.21: Tukey analysis of BBR creep stiffness at -12°C. (a): confidence interval of the pairwise comparison. (b): boxplot of results with letter grouping.

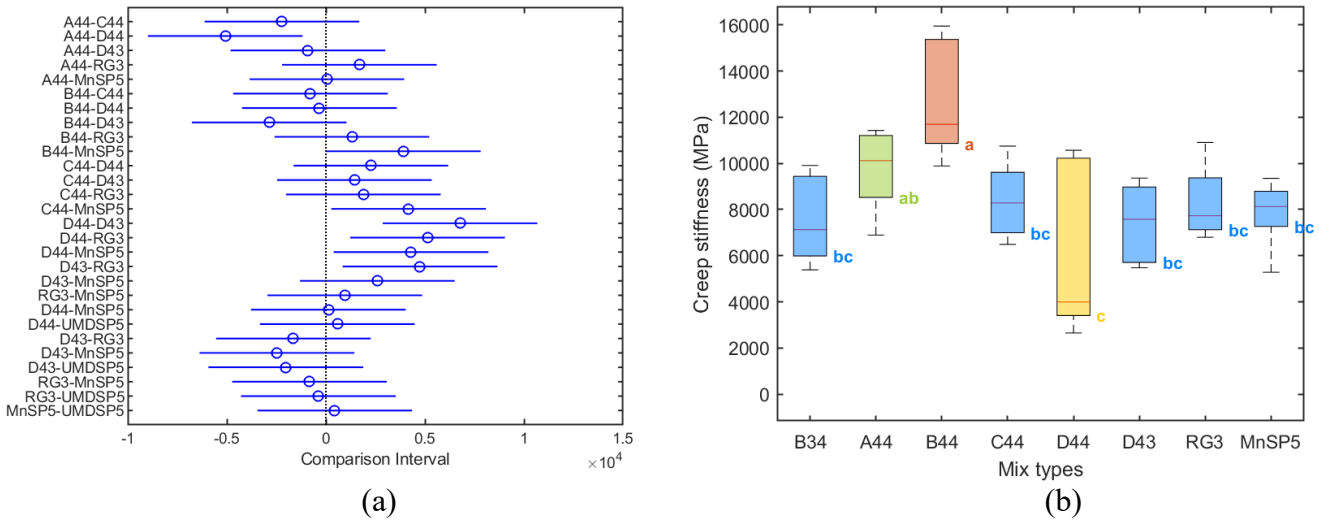

Figure 5.22: Tukey analysis of BBR creep stiffness at -24°C. (a): confidence interval of the pairwise comparison. (b): boxplot of results with letter grouping.

5.5.1 Analysis of BBR m-Value Results

Table 5.25, Table 5.26, and Table 5.27 show the one-way ANOVA analysis of BBR m-value results at 0, -12 and -24°C, respectively.

Table 5.25: ANOVA analysis of BBR m-value results at 0°C

Source of Variation	SS	df	MS	F	P-value
Between Groups	1.119E-01	7	1.598E-02	1.363E+01	7.444E-09
Within Groups	4.691E-02	40	1.173E-03		
Total	1.588E-01	47			

Table 5.26: ANOVA analysis of BBR m-value results at -12°C

Source of Variation	SS	df	MS	F	P-value
Between Groups	4.964E-02	7	7.091E-03	1.069E+01	1.675E-07
Within Groups	2.653E-02	40	6.633E-04		
Total	7.617E-02	47			

Table 5.27: ANOVA analysis of BBR m-value results at -24°C

Source of Variation	SS	df	MS	F	P-value
Between Groups	1.226E-02	7	1.752E-03	5.855E+00	1.015E-04
Within Groups	1.197E-02	40	2.992E-04		
Total	2.423E-02	47			

The p-values are all less than the significant level of 0.05. Therefore, at all temperature levels, the BBR m-value is significantly different between mixtures. Tukey analysis is performed to detect specific difference between mixtures. The results are shown in Figure 5.23, Figure 5.24, and Figure 5.25. Significant pairwise difference are detected and the results of the pairwise comparison are different at different temperatures. The MnSP5 mixture consistently has higher m-value than the other mixtures.

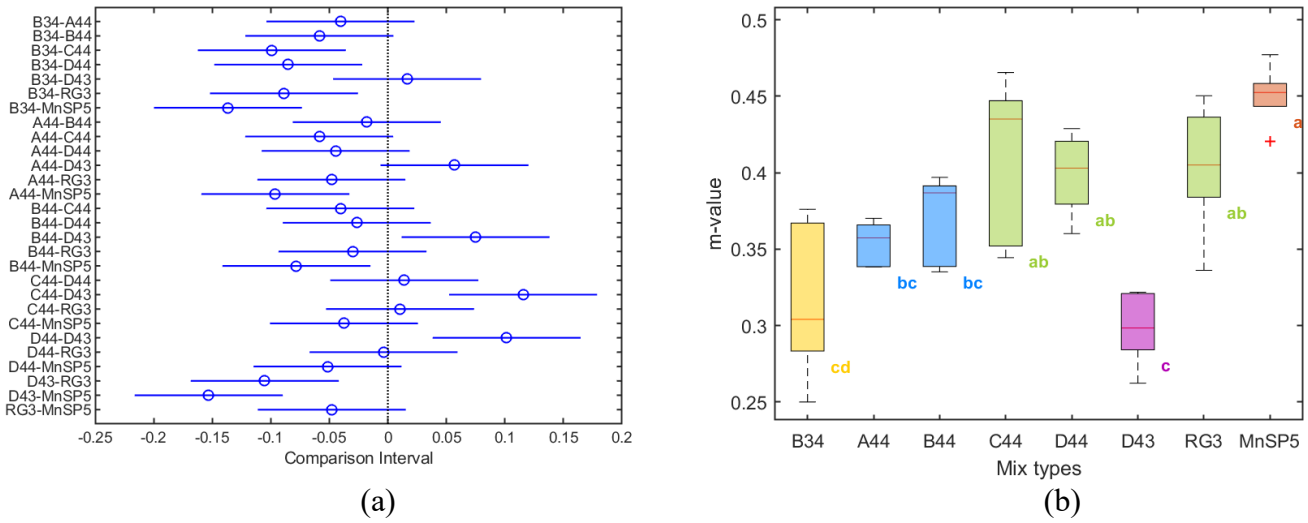

Figure 5.23: Tukey analysis of BBR m-value at 0°C. (a): confidence interval of the pairwise comparison. (b): boxplot of results with letter grouping.

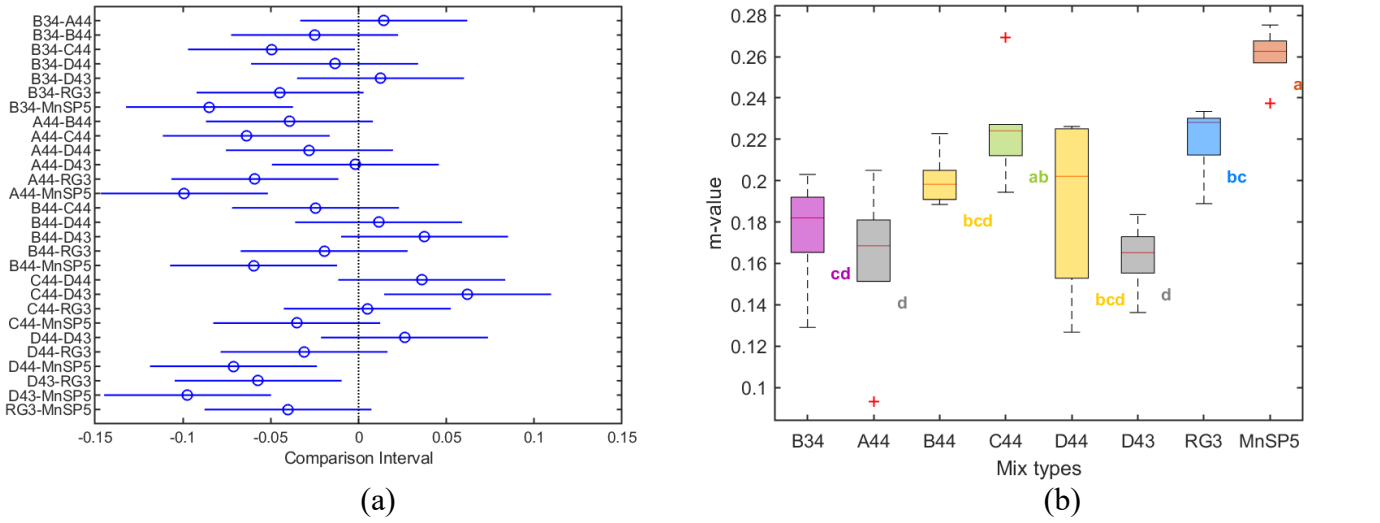

Figure 5.24: Tukey analysis of BBR m-value at -12°C. (a): confidence interval of the pairwise comparison. (b): boxplot of results with letter grouping.

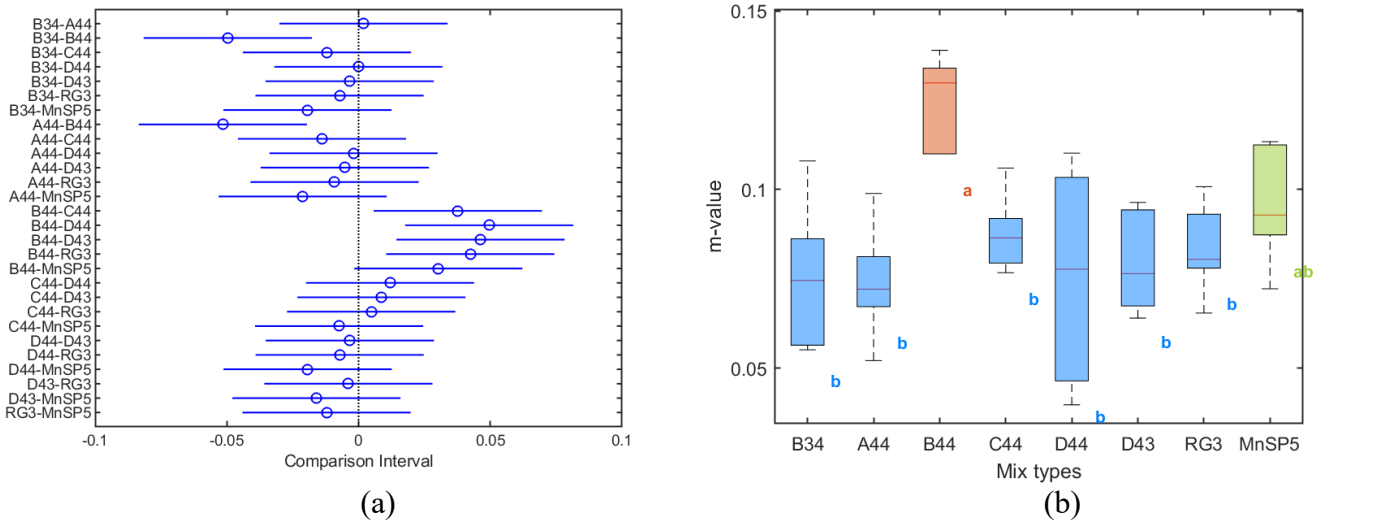

Figure 5.25: Tukey analysis of BBR m-value at -24°C. (a): confidence interval of the pairwise comparison. (b): boxplot of results with letter grouping.

5.5.2 Analysis of IDT Creep Stiffness Results

IDT creep stiffness results at 60s and 500s are analyzed by one-way ANOVA and the results are listed in Table 5.28 and Table 5.29.

Table 5.28: ANOVA analysis of IDT creep stiffness at 60s results at -12°C

Source of Variation	SS	df	MS	F	P-value
Between Groups	8.572E+01	8	1.072E+01	1.131E+01	7.144E-04
Within Groups	8.523E+00	9	9.471E-01		
Total	9.425E+01	17			

Table 5.29: ANOVA analysis of IDT creep stiffness at 500s results at -12°C

Source of Variation	SS	df	MS	F	P-value
Between Groups	2.688E+01	8	3.360E+00	1.939E+01	8.245E-05
Within Groups	1.559E+00	9	1.733E-01		
Total	2.844E+01	17			

The p-values of the creep stiffness results at 60s and 500s are less than the significant level of 0.05. Therefore, IDT creep stiffness at both 60s and 500s of mixtures have significant difference. Tukey analysis ise performed to further detect the specific difference between mixtures. The results of IDT creep stiffness at 60s and 500s are shown in Figure 5.26 and Figure 5.27, respectively. The results of 60s and 500s are relatively consistent. Mixture B34 has a significant higher creep stiffness, while MnSP5 has a significant lower creep stiffness. The rest mixtures do not have significant differences.

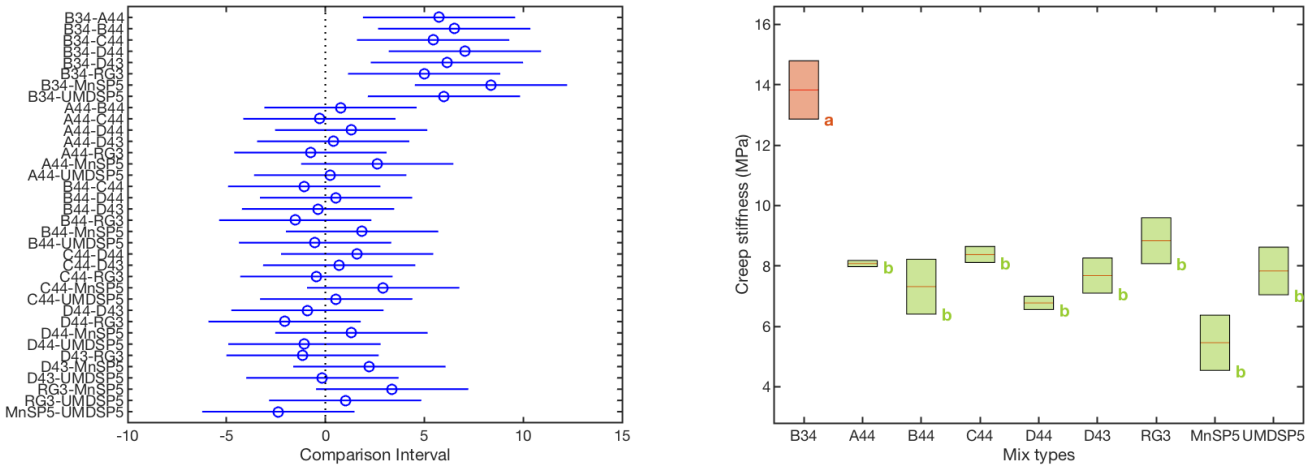

Figure 5.26: Tukey analysis of IDT creep stiffness at 60s at -12°C. (a): confidence interval of the pairwise comparison. (b): boxplot of results with letter grouping.

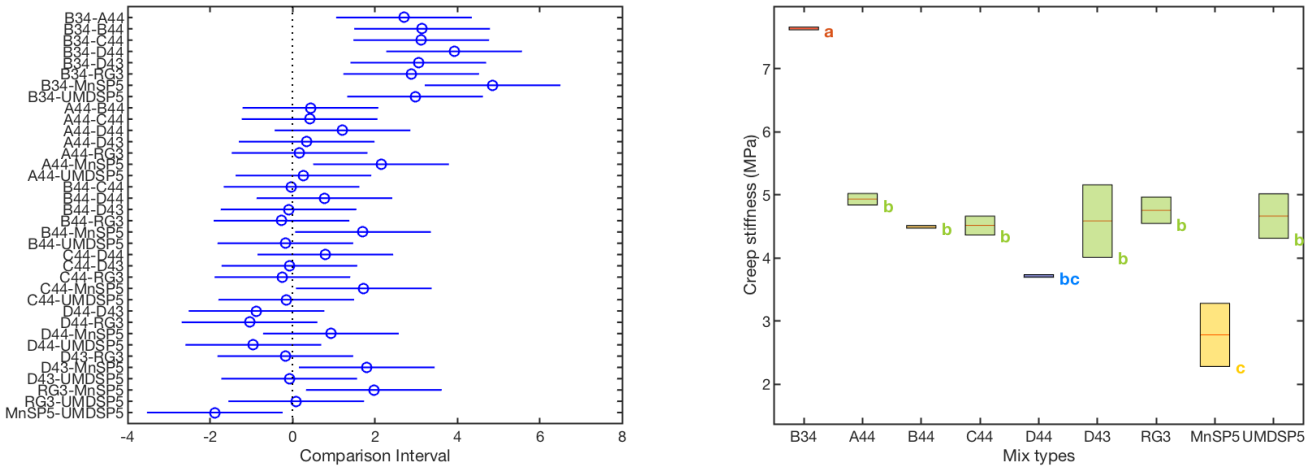

Figure 5.27: Tukey analysis of IDT creep stiffness at 500s at -12°C. (a): confidence interval of the pairwise comparison. (b): boxplot of results with letter grouping.

5.5.3 Analysis of IDT Dynamic Modulus Results

Table 5.30, Table 5.31, and Table 5.32 show the one-way ANOVA analysis of IDT E* (25Hz) results at -12, 6 and 24°C, respectively.

Table 5.30: ANOVA analysis of IDT E* (25Hz) results at -12°C

Source of Variation	SS	df	MS	F	P-value
Between Groups	1.017E+02	8	1.272E+01	2.599E+00	4.404E-02
Within Groups	8.808E+01	18	4.893E+00		
Total	1.898E+02	26			

Table 5.31: ANOVA analysis of IDT E* (25Hz) results at 6°C

Source of Variation	SS	df	MS	F	P-value
Between Groups	9.414E+01	8	1.177E+01	6.359E+00	5.616E-04
Within Groups	3.331E+01	18	1.851E+00		
Total	1.275E+02	26			

Table 5.32: ANOVA analysis of IDT E* (25Hz) results at 24°C

Source of Variation	SS	df	MS	F	P-value
Between Groups	1.135E+01	8	1.419E+00	2.981E+00	2.584E-02
Within Groups	8.568E+00	18	4.760E-01		
Total	1.992E+01	26			

The p-values of the results at the three different temperatures are all less than the significant level of 0.05. Therefore, at all temperature levels, the results of E* at 25Hz have significant difference between mixtures. Tukey analysis is performed to further detect the specific difference between mixtures. The results of the three temperature levels are shown in Figure 5.28, Figure 5.29, and Figure 5.30, respectively. Although ANOVA shows the p-value of E* at -12 °C is 0.044 which is less than 0.05, the Tukey analysis show no significant pairwise differences. Thus, for E* at -12°C there are no significant differences between mixtures. At 6 and 24°C, however, there are significant differences between mixtures.

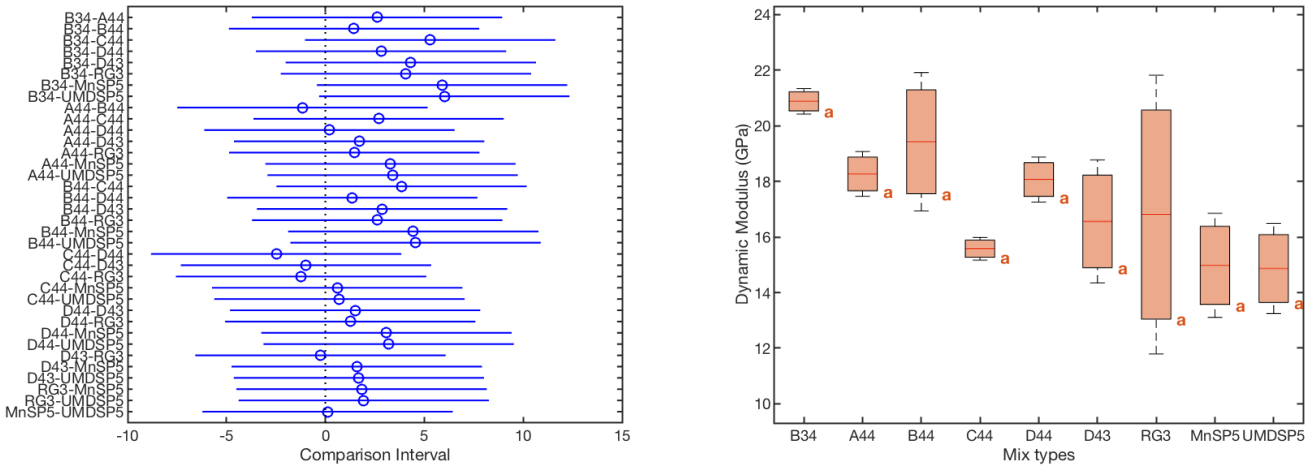

(a) (b)

Figure 5.28: Tukey analysis of IDT E* (25Hz) at -12°C. (a): confidence interval of the pairwise comparison. (b): boxplot of results with letter grouping.

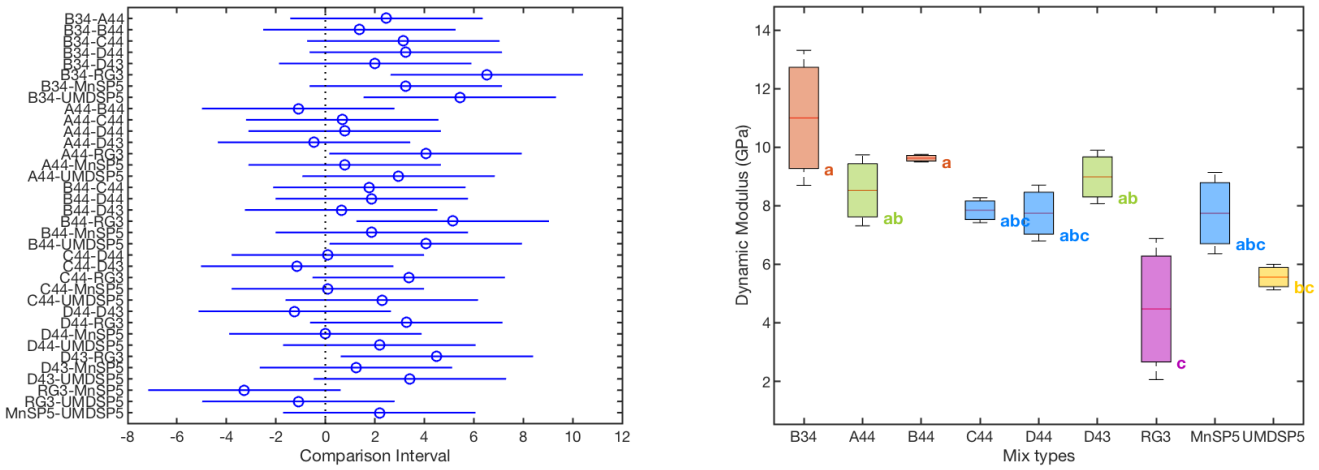

(a) (b)

Figure 5.29: Tukey analysis of IDT E* (25Hz) at 6°C. (a): confidence interval of the pairwise comparison. (b): boxplot of results with letter grouping.

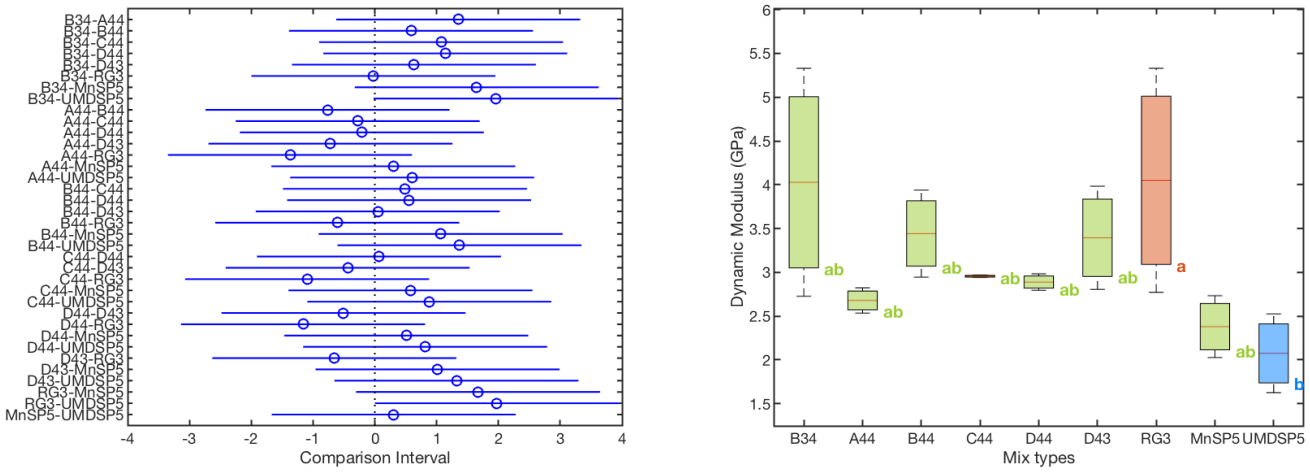

Figure 5.30: Tukey analysis of IDT E* (25Hz) results at 24 °C. (a): confidence interval of the pairwise comparison. (b): boxplot of results with letter grouping.

5.5.4 Analysis of SCB Fracture Results

The SCB fracture tests are performed at two temperatures. At the -21°C, all mixtures are tested, while at -12°C, only the high-density mixtures are tested. Table 5.33 and Table 5.34 show the ANOVA results of the fracture energy and toughness at -21°C. The results show both fracture energy and fracture toughness have a p-value that is larger than 0.05. Thus, we can conclude that there is no significant difference for the fracture properties at -21°C.

Table 5.33: ANOVA analysis of the SCB fracture energy results at -21°C

Source of Variation	SS	df	MS	F	P-value
Between Groups	9.447E-02	8	1.181E-02	3.052E+00	5.345E-02
Within Groups	6.964E-02	18	3.869E-03		
Total	1.641E-01	26			

Table 5.34: ANOVA analysis of the SCB fracture toughness results at -21°C

Source of Variation	SS	df	MS	F	P-value
Between Groups	1.079E-01	8	1.349E-02	1.675E+00	1.728E-01
Within Groups	1.449E-01	18	8.052E-03		
Total	2.528E-01	26			

Table 5.36 show the ANOVA results of fracture properties at -12°C, and the results are only for the three high-density mixtures. Since the p-value as shown in the tables are all larger than 0.05, we can conclude that there is no significant difference between the three high-density mixtures in terms of the fracture properties at this temperature. Therefore, there is no need for Tukey analysis.

Table 5.35: ANOVA analysis of the SCB fracture energy results at -12°C

Source of Variation	SS	df	MS	F	P-value
Between Groups	5.237E-02	2	2.619E-02	3.677E+00	9.069E-02
Within Groups	4.273E-02	6	7.121E-03		
Total	9.510E-02	8			

Table 5.36: ANOVA analysis of the SCB fracture toughness results at -12°C

Source of Variation	SS	df	MS	F	P-value
Between Groups	2.589E-02	2	1.294E-02	4.728E+00	5.849E-02
Within Groups	1.643E-02	6	2.738E-03		
Total	4.231E-02	8			

5.5.5 Analysis of BBR Failure Strength Results

Table 5.37, Table 5.38, and Table 5.39 show the one-way ANOVA analysis of BBR failure strength results at 0, -12 and -24°C, respectively.

Table 5.37: ANOVA analysis of BBR failure strength results at 0°C

Source of Variation	SS	df	MS	F	P-value
Between Groups	3.340E+01	7	4.772E+00	5.719E+00	1.251E-04
Within Groups	3.338E+01	40	8.344E-01		
Total	6.678E+01	47			

Table 5.38: ANOVA analysis of BBR failure strength results at -12°C

Source of Variation	SS	df	MS	F	P-value
Between Groups	1.452E+02	7	2.074E+01	9.720E+00	5.240E-07
Within Groups	8.535E+01	40	2.134E+00		
Total	2.305E+02	47			

Table 5.39: ANOVA analysis of BBR failure strength results at -24°C

Source of Variation	SS	df	MS	F	P-value
Between Groups	9.410E+01	7	1.344E+01	1.481E+01	2.412E-09
Within Groups	3.631E+01	40	9.078E-01		
Total	1.304E+02	47			

The p-values are less than the significant level of 0.05. Therefore, at all temperature levels, the results of failure strength have significant difference between mixtures. Tukey analysis is performed and the results are shown in Figure 5.31, Figure 5.32, and Figure 5.33, respectively.

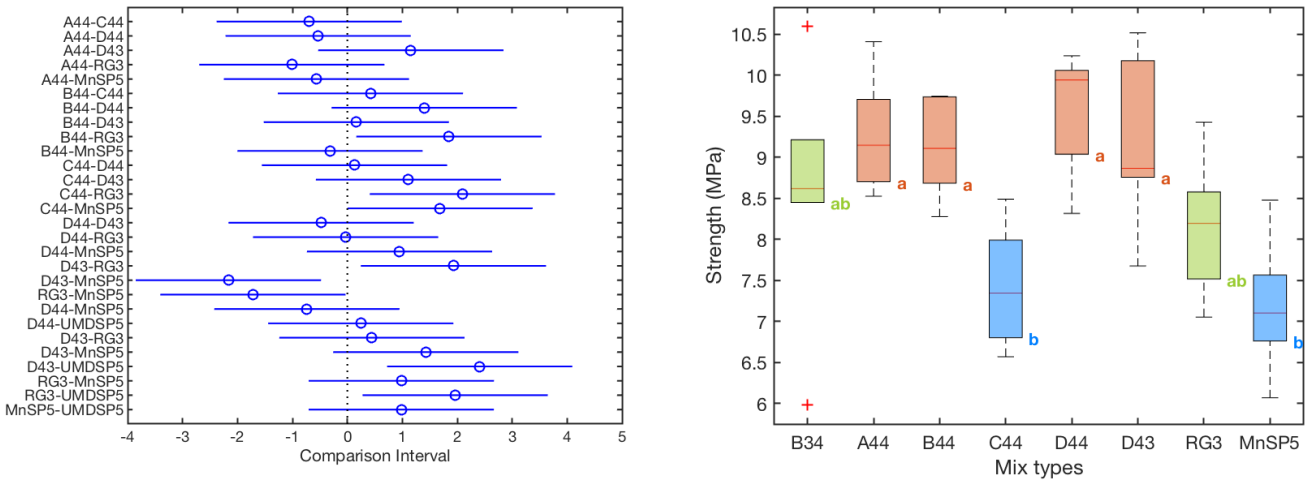

Figure 5.31: Tukey analysis of BBR failure strength at 0°C. (a): confidence interval of the pairwise comparison. (b): boxplot of results with letter grouping.

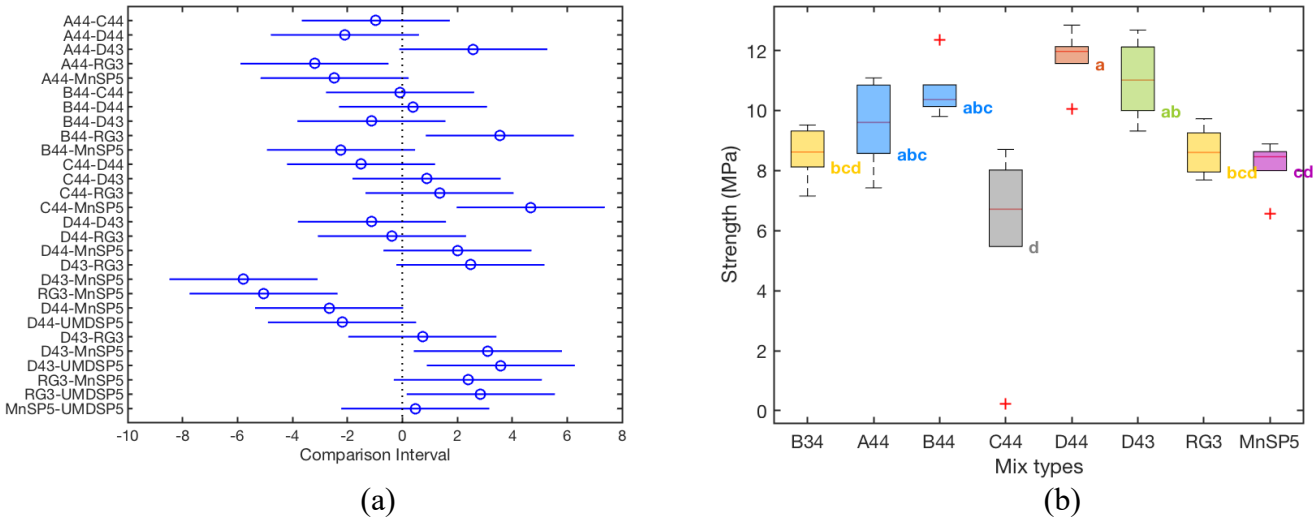

Figure 5.32: Tukey analysis of BBR failure strength at -12°C. (a): confidence interval of the pairwise comparison. (b): boxplot of results with letter grouping.

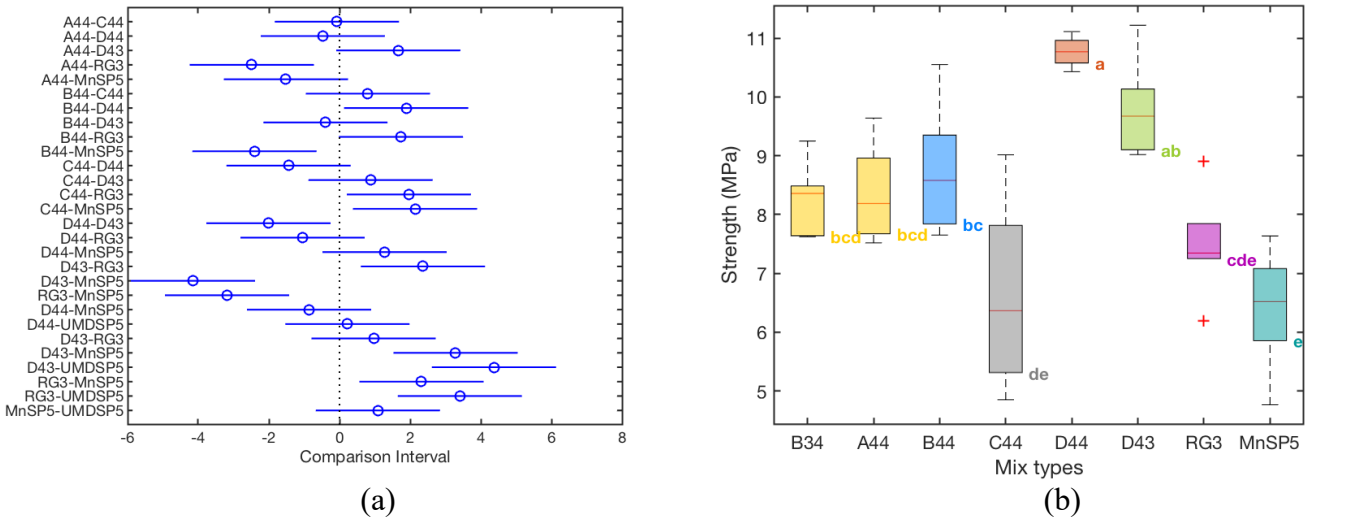

Figure 5.33: Tukey analysis of BBR failure strength at -24°C. (a): confidence interval of the pairwise comparison. (b): boxplot of results with letter grouping.

The rankings of the mixtures are relatively consistent at different temperatures. D44 is significantly larger than other mixtures, while C44 is significantly less than other mixtures at different temperatures.

5.5.6 Analysis of BBR Failure Strain Results

Table 5.40, Table 5.41, and Table 5.42: ANOVA analysis of BBR failure strain results at -24°C show the one-way ANOVA analysis of BBR failure strain results at 0, -12 and -24°C, respectively.

Table 5.40: ANOVA analysis of BBR failure strain results at 0°C

Source of Variation	SS	df	MS	F	P-value
Between Groups	2.005E+00	7	2.864E-01	4.018E+00	2.042E-03
Within Groups	2.851E+00	40	7.129E-02		
Total	4.857E+00	47			

Table 5.41: ANOVA analysis of BBR failure strain results at -12°C

Source of Variation	SS	df	MS	F	P-value
Between Groups	1.723E-01	7	2.461E-02	3.572E+00	4.465E-03
Within Groups	2.755E-01	40	6.889E-03		
Total	4.478E-01	47			

Table 5.42: ANOVA analysis of BBR failure strain results at -24°C

Source of Variation	SS	df	MS	F	P-value
Between Groups	1.112E-01	7	1.589E-02	7.832E-01	6.053E-01
Within Groups	8.116E-01	40	2.029E-02		
Total	9.229E-01	47			

The p-values are less than the significant level of 0.05, except for -24°C. Tukey analysis is performed for 0°C and -12°C and the results are shown in Figure 5.34 and Figure 5.35, respectively. D44 has a larger failure strain than other mixtures at all temperatures.

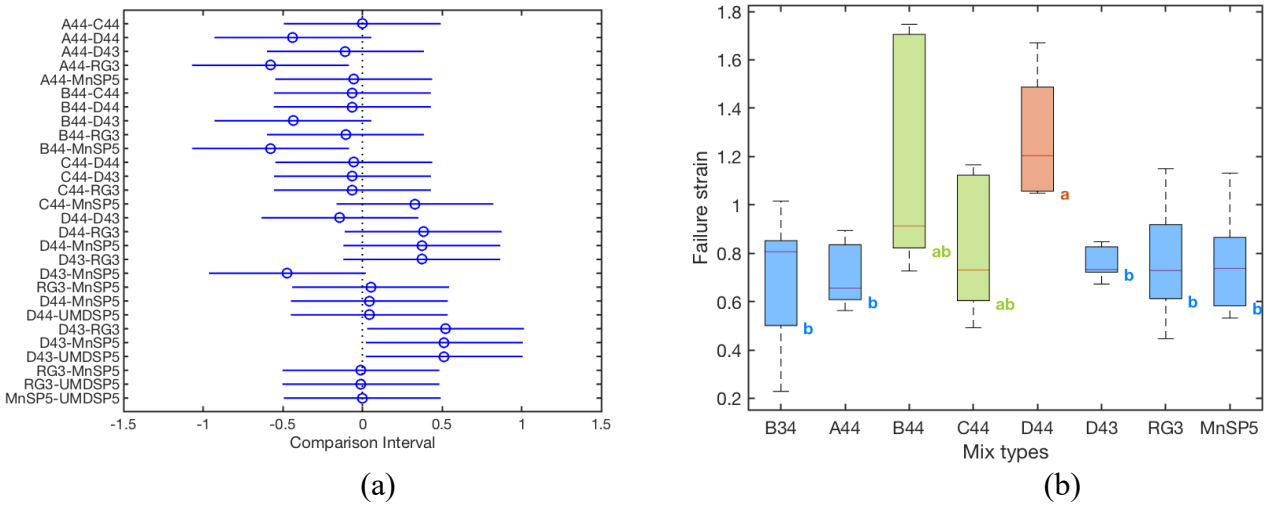

Figure 5.34: Tukey analysis of BBR failure strain at 0°C. (a): confidence interval of the pairwise comparison. (b): boxplot of results with letter grouping.

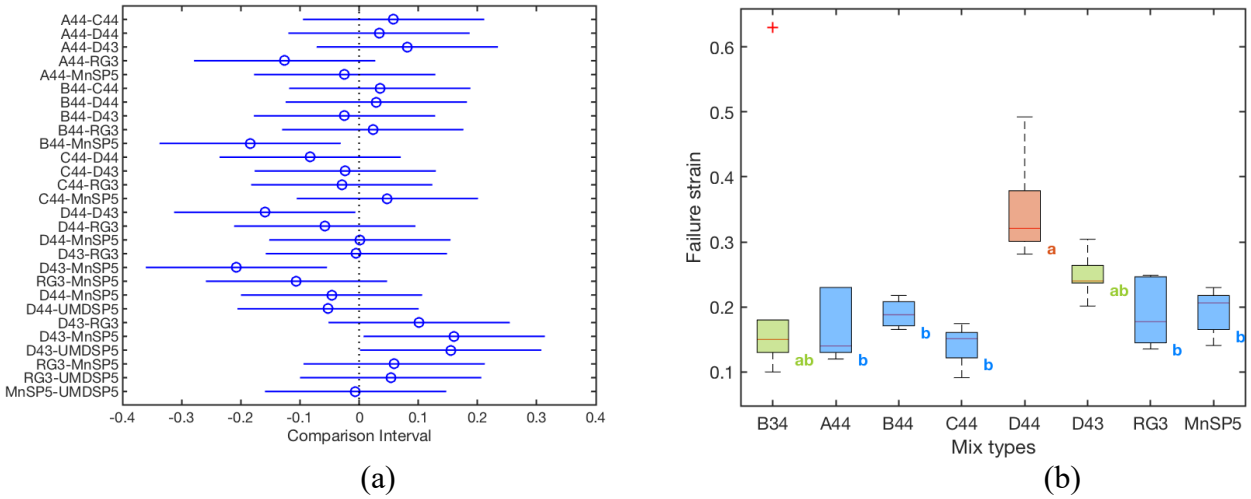

Figure 5.35: Tukey analysis of BBR failure strain results at -12 °C. (a): confidence interval of the pairwise comparison. (b): boxplot of results with letter grouping.

5.5.7 Analysis of Flow Number Results

An ANOVA test performed, as shown in Table 5.43, indicated that the difference of the FN results among the three mixtures were significant. Note that the FN results of all these mixtures were above the minimum average FN requirement of 50 for traffic level 3 to 10 million ESALs.

Table 5.43: Statistical analysis (ANOVA) of FN test results

Mix	Source of Variation	Sum of Squares	df	MS	F	P-value	F crit	Significantly Different
SP5 and RG3	*Between Variation*	2466568	1	2466568	8.376	*0.044*	7.708	Yes
	Within Variation	1177787	4	294447				
	Total Variation	3644355	5					
SP5 and Rep. SP5	*Between Variation*	776880.2	1	776880	32.454	*0.004*	7.708	Yes
	Within Variation	95748.67	4	23937				
	Total Variation	872628.8	5					

5.6 CORRELATION ANALYSIS

To further investigate the relationship between different mixture properties, correlation matrices were calculated based on Pearson's correlation. The interpretation for the values of the correlation coefficients is as the follows:

$\|r\| = 0$	No correlation
$0 < \|r\| < 0.19$	Very weak correlation
$0.2 < \|r\| < 0.39$	Weak correlation
$0.4 < \|r\| < 0.59$	Moderate correlation
$0.6 < \|r\| < 0.79$	Strong correlation
$0.8 < \|r\| < 0.99$	Very strong correlation
$\|r\| = 1$	Prefect correlation

The correlation analyses were performed on the mixture properties at two temperature levels, -12 °C and -24°C. The correlation matrices of the two temperature levels are listed in Table 5.44 and Table 5.45, respectively. Coefficients larger than 0.60 are highlighted in bold to show there is a strong correlation. The value of coefficients is also shown by the color of the cells.

Table 5.44: Correlation matrix for mixture properties at -12°C.

	1	*2*	*3*	*4*	*5*	*6*	*7*	*8*	*9*	*10*	*11*	*12*	*13*	*14*	*15*	*16*
1. BBR S @ 60s	1.00															
2. BBR m	-0.29	1.00														
3. IDT S @ 60s	0.46	-0.41	1.00													
4. IDT S @ 500s	0.56	-0.55	**0.98**	1.00												
5. BBR strength	0.08	-0.55	-0.24	-0.13	1.00											
6. BBR failure strain	-0.40	-0.30	-0.10	-0.11	**0.74**	1.00										
7. IDT E* @ 25Hz	**0.63**	**-0.62**	**0.63**	**0.68**	0.38	0.23	1.00									
8. IDT E* @ 0.01Hz	0.39	**-0.76**	**0.60**	**0.69**	0.55	0.46	**0.68**	1.00								
9. % AC	-0.46	-0.20	-0.44	-0.43	0.52	0.57	-0.30	-0.01	1.00							
10. G_{mm}	0.58	0.16	0.40	0.43	**-0.67**	**-0.85**	0.05	-0.05	**-0.88**	1.00						
11. G_{mb}	0.36	0.02	0.38	0.40	**-0.68**	**-0.84**	-0.08	-0.13	**-0.72**	**0.88**	1.00					
12. % Air Voids	-0.32	**0.66**	-0.17	-0.28	**-0.90**	**-0.71**	-0.49	**-0.80**	-0.26	0.34	0.44	1.00				
13. % VMA	**-0.76**	0.10	-0.58	**-0.63**	0.30	0.54	-0.50	-0.29	**0.91**	**-0.87**	**-0.69**	0.01	1.00			
14. P_{be}	**-0.60**	-0.16	-0.47	-0.48	**0.67**	**0.85**	-0.18	0.07	**0.88**	**-0.96**	**-0.85**	-0.43	**0.88**	1.00		
15. NMAS	0.12	0.57	0.22	0.14	**-0.90**	**-0.79**	-0.10	-0.43	**-0.71**	**0.73**	**0.62**	**0.80**	**-0.52**	**-0.81**	1.00	
16. N_{Design}	0.05	-0.03	0.01	0.03	-0.17	-0.37	0.31	-0.06	-0.48	0.29	0.40	0.32	-0.40	-0.40	0.40	1.00

Table 5.45: Correlation matrix for mixture properties at -24°C.

	1	*2*	*3*	*4*	*5*	*6*	*7*	*8*	*9*	*10*	*11*	*12*	*13*	*14*
1. BBR S @ 60s	1.00													
2. BBR m	**0.78**	1.00												
3. SCB G_f^*	-0.30	-0.05	1.00											
4. SCB K_{Ic}^*	-0.32	-0.49	0.29	1.00										
5. BBR strength	-0.22	-0.20	0.01	**0.84**	1.00									
6. BBR failure strain	-0.10	0.19	0.50	**0.62**	**0.70**	1.00								
7. % AC	-0.51	-0.30	0.59	0.46	0.50	0.43	1.00							
8. G_{mm}	**0.63**	0.31	-0.34	-0.43	**-0.67**	-0.53	**-0.88**	1.00						
9. G_{mb}	0.41	-0.06	-0.28	-0.26	**-0.62**	**-0.64**	**-0.72**	**0.88**	1.00					
10. % Air Voids	0.07	0.08	0.31	-0.56	**-0.86**	-0.41	-0.26	0.34	0.44	1.00				
11. % VMA	**-0.65**	-0.33	**0.66**	0.32	0.31	0.38	**0.91**	**-0.87**	**-0.69**	0.01	1.00			
12. P_{be}	**-0.62**	-0.31	0.39	0.53	**0.68**	0.54	**0.88**	**-0.96**	**-0.85**	-0.43	**0.88**	1.00		
13. NMAS	0.37	0.35	-0.03	**-0.68**	**-0.85**	-0.38	**-0.71**	**0.73**	**0.62**	**0.80**	**-0.52**	-0.81	1.00	
14. N_{Design}	0.51	0.23	-0.35	-0.10	-0.10	-0.05	-0.48	0.29	0.40	0.32	-0.40	-0.40	0.40	1.00

* Since the SCB tests at -24°C were not available, SCB tests results at a close temperature (-21°C) were used here.

5.7 CONCLUSIONS

In this chapter, we performed mechanical tests to compare the mechanical properties of high-density asphalt mixtures to the mechanical properties of conventional mixtures. We analyzed the results using statistical methods, such as ANOVA and Tukey analyses, to detect significant differences between different mixtures. In addition, we calculated correlations to identify highly correlated properties and design parameters.

Using one-way ANOVA, we found significant differences between mixtures for 20 of the 24 mechanical properties investigated. The exceptions are the SCB fracture energy, fracture toughness, the IDT E* at -12°C, and BBR failure strain at -24°C.

From the pairwise comparison based on Tukey analysis, we found that grouping varied significantly with test methods and test temperatures. However, we did not observe consistent trends in mixture properties. Therefore, we can conclude that the properties of high-density mixtures as a group are not significantly different compared to the conventional mixtures.

From correlations between volumetric properties, we found that the asphalt content, G_{mm}, G_{mb}, Air voids, VMA, and P_{be} are strongly correlated, with |r| values larger than 0.8. NAMS was strongly correlated with other volumetric properties, with |r| values ranging from 0.6 to 0.8. N_{design} had weak correlation with other volumetric properties, with |r| values less than 0.4

We observed strong correlations between rheological properties, such as BBR S, BBR m, and IDT S. We observed less significant correlations between failure properties. For example, SCB fracture energy has weak correlations with other fracture properties, such as fracture toughness, BBR failure strength and strain.

By running correlations between volumetric properties and mechanical properties, we found that air void ratio and asphalt content have strong correlations with rheological and failure properties. In particular, the air voids had an inverse correlation with BBR strength at both test temperatures. NMAS has stronger correlation with failure properties than asphalt content and air void ratio. However, N_{design} has weak correlations with most mechanical properties.

CHAPTER 6: SUMMARY, CONCLUSIONS, AND RECOMMENDATIONS

In this research effort, we investigated the compaction process of asphalt mixtures through a combined experimental and computational approach. The goal was to understand the main factors responsible for the success of a recently proposed Superpave 5 mix design method. First, we built a two-scale DEM model to simulate the compaction process of HMA. The computational model was anchored by a fluid dynamics-discrete element model, which is capable of capturing the motion of aggregates in the viscous binder. We then calibrated and validated the model using a series of experiments, which included a rheological test of the binder and a compaction test of the mixture. Finally, we obtained mechanical properties of high-density mixtures and compared them with mechanical properties of other mixtures used to build some of the MnROAD 2017 NRRA test sections.

First, we conducted a comprehensive literature review to document previous research efforts on the compaction of HMA and on the numerical modelling of the compaction process. We found that the current Superpave mix design relies on the assumption that traffic loading provides the final densification to the design air voids and N_{design} should be directly related to expected traffic level. This approach, however, results in asphalt mixtures that have less workability and for which the as-constructed air voids content can exceed 7%, significantly different from the design value of 4%. A number of researchers also questioned the assumption that the density of samples increases linearly with the log of the number of gyration in the SGC and indicates that the "locking point" represents the upper boundary for the linear relationship; after that, excessive aggregate break down happens and the relationship becomes nonlinear. Thus, they concluded that using the data beyond "locking point" would cause higher error in determining the N_{design}. They proposed using the "locking point" gyration number instead of N_{design}. However, numerous factors affect the "locking point," such as gradation, type of binder, aggregate type and size, which makes its use more difficult.

We also found that only a limited number of researchers used DEM to simulate the compaction process. In all cases, the model used was rather simplistic and the contact laws between particles were not realistic, which resulted in significant deviations of simulation results from experimental data.

In Chapter 3, we develop a two-scale DEM model to simulate the compaction process of asphalt mixtures using a new framework, which only models the coarse aggregates explicitly, while the effect of the fine aggregate matrix (FAM) is modelled by the inter-particle interaction law. In the DEM, the inter-particle contact law follows the Hertzian-Mindlin contact model, and the inter-particle non-contact law is derived from granular physics. We use the model to simulate a preliminary set of compaction experiments, which involve both unmodified and GNP-modified asphalt mixtures, and show that the model can capture reasonably well the overall compaction process.

In Chapter 4, we improved the model by using non-spherical particles (composite particle model) to simulate the compaction behavior of asphalt mixtures. The main idea was to simulate the behavior of fine aggregate mixtures using the rheology of granular-fluid systems, while simulating the motion of

coarse aggregate explicitly as composite particles. We then calibrated the fine-scale DEM using the angle of repose experiment, and subsequently used the model to determine the rheology of FAM. We then validated the model by simulating the compaction of three Superpave 5 asphalt mixtures for which experimental data is available. The comparison between experiments and simulations showed that the current DEM simulation with composite particle model could capture the overall effect of gradation of aggregates on the bulk part of the compaction curves. For the initial portion of the compaction curve, the simulation results deviated from the experiments, which can be attributed to the interlock between composite particles that hinders the particle rearrangement. We expect that simulation results can be improved by considering different levels of non-sphericity.

In Chapter 5, we prepared asphalt mixture specimens from loose mix and conducted a number of experiments to determine if there were significant differences between mechanical properties of high-density mixtures and the corresponding properties of other mixtures. We performed the following experiments: Bending Beam Rheometer (BBR) Creep and Strength, Indirect Tensile (IDT) Creep, Diametral Dynamic Modulus (E*), Semi-Circular Bending (SCB), Uniaxial Dynamic Modulus (E*), and Flow Number (FN). From the ANOVA and Tukey analysis, we found that grouping varied significantly with test methods and test temperatures. However, we did not observe consistent trends in mixture properties. Therefore, we concluded that the properties of high-density mixtures as a group were not significantly different compared to the properties of conventional mixtures.

The current research effort indicates that the two-scale DEM model can provide reasonable simulations of asphalt mixture compaction in a gyratory compactor. In particular, the FAM rheology and the level of non-sphericity of the coarse aggregates have a significant effect. However, DEM simulations require significant computational time. Therefore, it appears to be more feasible to perform laboratory testing on a large set of materials to develop relationships between commonly measured properties and FAM rheology and the shape of coarse aggregates. These relationships can then be used to select the materials and proportions required to develop mix designs for high-density asphalt mixtures.

The link between laboratory compaction and field compaction needs to be further investigated. For example, it is not clear if the field compaction properties of Superpave 5 asphalt mixtures are directly related to the increase in design air voids from 4% to 5%, or to the significant reduction in the design number of gyrations, or to a combination of both. To better understand this link, an extensive experimental campaign combined with field construction data needs to be performed, which would require detailed laboratory compaction data, such as compaction curves, and field density data at various stages of the compaction process for a large number of projects.

REFERENCES

AASHTO R 30. (2002). *Mixture Conditioning of Hot Mix Asphalt (HMA). Standard specifications for Transportation Materials and Methods of Sampling and Testing*. Washington, DC: American Association of State Highway and Transportation Officials (ASHTO).

AASHTO R 47. (2008). *Reducing Samples of Hot Mix Asphalt (HMA) to Testing Size. Standard Specifications for Transportation Materials and Methods of Sampling and Testing.* Washington, DC: American Association of State Highway and Transportation Officials (ASHTO).

AASHTO R 83. (2017). *Preparation of Cylindrical Performance Test Specimens Using the Superpave Gyrator Compactor (SGC). Standard Specifications for Transportation Materials and Methods of Sampling and Testing.* Washington, DC: American Association of State Highway and Transportation Officials (ASHTO).

AASHTO R 84. (2017). *Developing Dynamic Modulus Master Curves for Asphalt Mixtures Using the Asphalt Mixture Performance Tester (AMPT). Standard Specifications for Transportation Materials and Methods of Sampling and Testing.* Washington, DC: American Association of State Highway and Transportation Officials (ASHTO).

AASHTO R30. (2006). *Mixture Conditioning of Hot Mix Asphalt (HMA). Standard Specifications for Transportation Materials and Methods of Sampling and Testing*. Washington, DC: American Association of State Highway and Transportation Officials (ASHTO).

AASHTO R47. (2008). *Reducing Samples of Hot Mix Asphalt (HMA) to Testing Size. Standard Specifications for Transportation Materials and Methods of Sampling and Testing*. Washington, DC: American Association of State Highway and Transportation Officials (ASHTO).

AASHTO T 313-02. (2006). *Determining the Flexural Creep Stiffness of Asphalt Binder Using the Bending Beam Rheometer (BBR). Washington, DC: American Association of State Highway and Transportation Officials.*

AASHTO T 322-03. (2006). *Determining the Creep Compliance and Strength of Hot Mix Asphalt (HMA) Using the Indirect Tensile (IDT) Test Device*. Washington, DC: American Association of State Highway and Transportation Officials (AASHTO).

AASHTO T 378, (2017). *Determining the Dynamic Modulus and Flow Number for Asphalt Mixtures Using the Asphalt Mixture Performance Tester (AMPT). Standard Specifications for Transportation Materials and Methods of Sampling and Testing*. Washington, DC: American Association of State Highway and Transportation Officials (ASHTO).

AASHTO TP 125-(16). (2016). *Standard Method of Test for Determining the Flexural Creep Stiffness of Asphalt Mixtures Using the Bending Beam Rheometer (BBR).* Washington, DC: American Association of State Highway and Transportation Officials (ASHTO).

AASHTO TP105. (2013). *Standard Method of Test for Determining the Fracture Energy of Asphalt Mixtures Using the Semicircular Bend Geometry (SCB).* Washington, DC: American Association of State Highway and Transportation Officials (ASHTO).

AASHTO TP62-03. (2006). *Standard Method of Test for Determining Dynamic Modulus of Hot-Mix Asphalt Concrete Mixtures.* Washington DC: American Association of State Highway and Transportation Officials (ASHTO).

AASHTO.M 323. (2005). *Standard Practice for Superpave Volumetric Mix Design*. Washington, DC: American Association of State Highway and Transportation Officials (ASHTO).

Abbas, A., Masad, E., Papagiannakis, T. & Harman, T. (2007). Micromechanical modeling of the viscoelastic behavior of asphalt mixtures using the discrete-element method. *International Journal of Geomechanics, 7*(2):131–139, 2007.

Anderson, R. M., McGennis, R. B., Weng, O. T., & Kennedy, T. W. (2000). Sensitivity of mixture performance properties to changes in laboratory compaction using the Superpave gyratory compactor. *Association of Asphalt Paving Technologists Proc*., *69*, 01–33.

Anderson, R., Hall, K., & Huner, M. (2006). Mechanical mixture simulation devices for determining and calibrating internal angle of gyration in Superpave gyratory compactor. *Transportation Research Record: Journal of the Transportation Research Board, 1970,* 99–105.

Barker, G. C., & Mehta, A. (1993). Transient phenomena, self-diffusion, and orientational effects in vibrated powders. *Physical Review, E 47*(1), 184–88. doi:10.1103/PhysRevE.47.184.

Blankenship, P. B. (1993). Gyratory compaction characteristics: Relation to service densities of asphalt mixtures (Master's Thesis). University of Kentucky, Lexington,

Blankenship, P. B., Mahboub, K. C., & Huber, G. A. (1994). Rational method for laboratory compaction of hot-mix asphalt. *Transportation Research Record, 1454*(8), 144–153.

Bonaquist, R. & Christensen, D. W. (2005). Practical procedure for developing dynamic modulus master curves for pavement structural design. *Transportation Research Record: Journal of the Transportation Research Board, 1929,* 208–217.

Boyer, F, Guazzelli, E., & Pouliquen, O. (2011). Unifying suspension and granular rheology. *Physical Review Letters, 107*(18), 1–5. doi:10.1103/PhysRevLett.107.188301

Brcic, H. (2016). Investigation of the Rheological Properties of Asphalt Binder Containing Graphene Nanoplatelets (unpublished master's thesis). Norwegian University of Science and Technology, Trondheim, Norway.

Brown, E. R., & Buchanan, M. S. (1999). *NCHRP Research Results Digest (237): Superpave gyratory compaction guidelines.* Washington, DC United States . Transportation Research Board

Brown, E. R., Hainin, M. R., Cooley, A., & Hurley, G. (2004). *Relationship of Air Voids, Lift Thickness, and Permeability in Hot Mix Asphalt Pavements* (NCHRP Report 531). Retrieved from https://doi.org/10.17226/13777

Brown, E. R., Kandhal, P. S., Roberts, F. L., Kim, Y. R., Lee, D. Y., & Kennedy, T. W. (2009). *Hot Mix Asphalt Materials, Mixture Design, and Construction*. Lanham, MD: NAPA Research and Education Foundation.

Brown, E., Hanson, D., & Mallick, R. (1996). Evaluation of Superpave gyratory compaction of hot-mix asphalt. *Transportation Research Record: Journal of the Transportation Research Board, 1543*, 145–150.

Buttlar W. G., & Roque R. (1994). Development and evaluation of the Strategic Highway Research Program measurement and analysis system for indirect tensile testing at low temperatures. *Transportation Research Record, 1454*, 163-171.

Buttlar, W., & You, Z. 2001. Discrete element modeling of asphalt concrete: Microfabric approach. *Transportation Research Record, 1757*(1), 111–18. doi:10.3141/1757-13

Cassar, C., Nicolas, M. & Pouliquen, O. (2005). Submarine granular flows down inclined planes. *Physics of Fluids, 17*(10), 103301. doi:10.1063/1.2069864.

Chen, J., Huang, B., & Shu, X. (2012). Air-void distribution analysis of asphalt mixture using discrete element method. *Journal of Materials in Civil Engineering. 25*(October), 1375–1385. doi:10.1061/(ASCE)MT.1943-5533.0000661

Chen, J., Huang, B., Shu, X., & Hu, C. (2015). DEM simulation of laboratory compaction of asphalt mixtures using an open source code. *Journal of Materials in Civil Engineering, 27(3)*, 1–10. doi:10.1061/(ASCE)MT.1943-5533.0001069

Chen, J. (2011). *Discrete element method (DEM) analyses for hot-mix asphalt (HMA) mixture compaction (Doctoral Dissertation)*. Retrieved from: https://trace.tennessee.edu/utk_graddiss/957/

Christensen D. (1998). Analysis of creep data from Indirect Tension test on asphalt concrete. *Journal of the Association of Asphalt Paving Technologists, 67*, 458–477.

Falchetto, A. C., Marasteanu, M. O., Balmurugan, S., & Negulescu, I. I. (2014). Investigation of asphalt mixture strength at low temperatures with the Bending Beam Rheometer. *Road Materials and Pavement Design, 15*(S1), 28–44. doi.org/10.1080/14680629.2014.926618

Fiscina, J. E., Lumay, G., Ludewig, F., & Vandewalle, N. (2010). Compaction dynamics of wet granular assemblies. *Physical Review Letters, 105*(4), 1–4. doi:10.1103/PhysRevLett.105.048001

Foerster, S., Michel, F., Louge, Y., Chang, H., & Allia, K. (1994). Measurements of the collision properties of small spheres. *Physics of Fluids, 6*(3), 1108–15. doi:10.1063/1.868282

Forterre, Y., & Pouliquen, O. (2008). Flows of dense granular media. *Annual Review of Fluid Mechanics, 40*(1), 1–24. doi:10.1146/annurev.fluid.40.111406.102142

Georgiou, P., Sideris, L., & Loizos, A. (2016). Evaluation of the effects of gyratory and field compaction on asphalt mix internal structure. *Materials and Structures, 49*(1–2), 665–676.

Guler, M., Bosscher, P. J., & Plesha, M. E. (2004). A porous elasto-plastic compaction model for asphalt mixtures with parameter estimation algorithm. *Recent Advances in Materials Characterization and Modeling of Pavement Systems* 126–143. NY, US: American Society of Civil Engineers.

Haddock, J. E. (2015). *Superpave5: Constructing Asphalt Pavement with Road Air Voids Equal to Design Air Voids.* Retrieved from http://onlinepubs.trb.org/Onlinepubs/webinars/150910.pdf

Harman, T., Bukowski, J., Moutier, F., Huber, G., & McGennis, R. (2002). History and future challenges of gyratory compaction: 1939 to 2001. *Transportation Research Record: Journal of the Transportation Research Board, 1789*, 200–207.

Harmelink, D., Aschenbrener, T., & Shuler, S. (2007). Achieving 4% air voids in real pavements with Superpave. *Transportation Research Record: Journal of the Transportation Research Board, 2040*, 115–122.

Hekmatfar, A., McDaniel, R. S., Shah, A., & Haddock, J. E. (2015). *Optimizing Laboratory Mixture Design as It Relates to Field Compaction to Improve Asphalt Mixture Durability*. Retrieved from https://doi.org/10.5703/1288284316010

Hill, K. M. & Yohannes, B. (2011). Rheology of dense granular mixtures: Boundary pressures. *Physical Review Letters, 106*(5). 058302.

Hu, J., Liu, P., Wang, D., Oeser, M., & Tan, Y. (2016). Investigation on fatigue damage of asphalt mixture with different air-voids using microstructural analysis. *Construction and Building Materials, 125*, 936–945. https://doi.org/10.1016/j.conbuildmat.2016.08.138

Jin, C., Yang, X., & You, Z. (2017). Automated real aggregate modelling approach in discrete element method based on x-ray computed tomography images. *International Journal of Pavement Engineering 18* (9), 837–50. doi:10.1080/10298436.2015.1066006

Jop, P., Forterre, Y., & Pouliquen, O. (2006). A constitutive law for dense granular flows. *Nature, 441*(7094), 727–30. doi:10.1038/nature04801

Kassem, E., Masad, E., Lytton, R., & Chowdhury, A. (2011). Influence of air voids on mechanical properties of asphalt mixtures. *Road Materials and Pavement Design, 12*(3), 493–524.

Kiesgen de Richter, S., Hanotin, C., Marchal, P., Leclerc, S., Demeurie, F., & Louvet. N. (2015). Vibration-induced compaction of granular suspensions. *European Physical Journal, E 38(7), 74.* doi:10.1140/epje/i2015-15074-7

Kim, W., Olympia, P. E., Mahoney, J. P., & Walter, J. (2007). *An Assessment of WSDOT's Hot-Mix Asphalt Quality Control and Assurance Requirements*. Retrieved from https://www.wsdot.wa.gov/Research/Reports/500/517.2.htm

Kim, Y., Seo, Y., King, M., & Momen, M. (2004). Dynamic modulus testing of asphalt concrete in indirect tension mode. *Transportation Research Record, 1891*, 163–173.

Knight, J., Christopher, B., Fandrich, G., Lau, C. N., Jaeger, H. M. &. Nagel, S. R. (1995). Density relaxation in a vibration granular material*. Physical Review E,* 51(5), 3951-3963.

Koneru, S. (2006). *A thermodynamic approach for compaction of asphaltic composites* (Master thesis). Retrieved from http://hdl.handle.net/1969.1/ETD-TAMU-1147

Koneru, S. (2010). *Modeling Hot Mix Asphalt Compaction Using a Thermodynamics Based Compressible Viscoelastic Model within the Framework of Multiple Natural Configurations (Doctoral Dissertation)*. Retrieved from Texas A&M University Theses, Dissertations, and Records of Study (2002–).

Le, J.-L., Cannone Falchetto, A., & Marasteanu, M. O. (2013) Determination of strength distribution of quasibrittle structures from size effect analysis. *Mechanics of Materials, 66,* 79–87.

Le, J.-L., Marasteanu, M., & Turos, M. (2016). *Graphene Nanoplatelet (GNP) Reinforced Asphalt Mixtures: A Novel Multifunctional Pavement Material* (NCHRP-IDEA 173 Report). Washington, D.C., US: Transportation Research Board.

Leiva, F., & West, R. (2008). Analysis of hot-mix asphalt lab compactability using lab compaction parameters and mix characteristics. *Transportation Research Record: Journal of the Transportation Research Board, 2057*, 89–98.

Li, J., Cao, Y., Xia, C., Kou, B., Xiao, X., Fezzaa, K., & Wang, Y. (2014). Similarity of wet granular packing to gels. *Nature Communications, 5*, 5014. doi:10.1038/ncomms6014

Li, X. & Marasteanu, M. O. (2004). Evaluation of low temperature fracture resistance of asphalt mixtures using the semi-circular bend test. *Journal of the Association of Asphalt Paving Technologists, 73*, 401–426.

Lim, I. L., Johnson, I. W., & Choi, S. K. (1993). Stress intensity factor for semi-circular specimen under three-point bending. *Engineering Fracture Mechanics, 44*(3), 363–382.

Liu, Y., Dai, Q., & You, Z. (2009). Viscoelastic model for discrete element simulation of asphalt mixtures. *Journal of Engineering Mechanics, 135*(4), 324–33. doi:10.1061/(ASCE)0733-9399(2009)135:4(324)

Luding, S, Nicolas, M., & Pouliquen, O. (2000). A minimal model for flow dynamics: Compaction of granular media under vibration or shear. *Compaction of Soils, Granulates and Powders,* 3,241-247.

Lumay, G., Fiscina, J., Ludewig, F., & Vandewalle, N. (2013). Influence of cohesive forces on the macroscopic properties of granular assemblies. *AIP Conference Proceedings, 1542*, 995–998. doi:10.1063/1.4812101

Marasteanu, M., Falchetto, A. C., Turos, M., & Le, J. L. (2012). *Development of a Simple Test to Determine the Low Temperature Strength of Asphalt Mixtures and Binders* (No. NCHRP IDEA Project 151). Washington, D.C., US: Transportation Research Board.

Marasteanu, M., Zofka, A., Turos, M., Li, X., Velasquez, R., Li, X. … & McGraw, J. (2007). *National Pooled Fund Study 776 - Investigations of Low Temperature Cracking in Asphalt Pavements*. St. Paul, MN: Mn/DOT.

Masad, E., Koneru, S., Scarpas, T., Kassem, E., & Rajagopal, K. R. (2010). *Modeling of Hot-Mix Asphalt Compaction: A Thermodynamics-Based Compressible Viscoelastic Model.* (No. FHWA-HRT-10-065). Turner-Fairbank Highway Research Center.

McDaniel, R. S., & Levenberg, E. (2013). *Risk Management of Low Air Void Asphalt Concrete Mixtures.* Retrieved from https://docs.lib.purdue.edu/jtrp/1526/

McDaniel, R. S., Leahy, R. B., Huber, G. A., Moulthrop, J. S., & Ferragut, T. (2011). *The superpave mix design system: anatomy of a research program.* Washington, DC: The National Academies Press. https://doi.org/10.17226/22812.

Mehta, A, Barker, G. C., & Luck, J. M. (2004). Cooperativity in sandpiles: Statistics of bridge geometries. *Journal of Statistical Mechanics-Theory and Experiment*, (2004)P10014. doi:10.1088/1742-5468/2004/10/P10014

Mehta, A., & Barker, G. C. (1994). The dynamics of sand. *Reports on Progress in Physics, 57* (4), 383–416. doi:10.1088/0034-4885/57/4/002

Midi, G. D. R. (2004). On dense granular flows. *The European Physical Journal, E 365*, 1–26. doi:10.1140/epje/i2003-10153-0

Moutier, F. (1974). La presse a` cisaillement giratorie, mode`le de se´rie. *Bulletin Liaison Ponts Chausse´es, 74*, 137–148.

Nicolas, M., Duru, P. & Pouliquen, O. (2000). Compaction of a granular material under xyclic shear. *The European Physical Journal, E 314*(4), 7. doi:10.1007/s101890070001

Oehlert, G. W. (2000). *A First Course in Design and Analysis of Experiments*. New York, United States: W. H. Freeman.

Peterson, R., Mahboub, K., Anderson, R., Masad, E., & Tashman, L. (2003). Superpave®laboratory compaction versus field compaction. *Transportation Research Record: Journal of the Transportation Research Board, 1832*, 201–208.

Philippe, P., & Bideau, D. (2002). Compaction dynamics of a granular medium under vertical tapping. *Europhysics Letters (EPL), 60*, 677. doi:10.1209/epl/i2002-00362-7

Piepho, H.-P. (2004). An algorithm for a letter-based representation of all pairwise comparisons. *Journal of Computational and Graphical Statistics, 13*, 456–466.

Pine, W. J. (1997). *Superpave Gyratory Compaction and the Ndesign Table. Relatório.* Chicago, IL: Illinois Department of Transportation.

Poschel, T. & Schwager, T. (2005). *Computational Granular Dynamics: Models and Algorithms.* New York: Springer Science & Business Media.

Pouliquen, O., Belzons, M., & Nicolas, M. (2003). Fluctuating particle motion during shear induced granular compaction. *Physical Review Letters, 91*(1), 14301 doi:10.1103/PhysRevLett.91.014301.

Pouliquen, O., & Forterre, Y. (2001). Friction law for dense granular flows: Application to the motion of a mass down a rough inclined plane. *Journal of Fluid Mechanics, 453*(1998), 19. doi:10.1017/S0022112001006796

Pouliquen, O., Cassar, C., Jop, P., Forterre, Y., & Nicolas, M. (2006). Flow of dense granular material: Towards simple constitutive laws. *Journal of Statistical Mechanics: Theory and Experiment, 2006*(07), P07020.

Pouliquen, O., Belzons, M., & Nicolas, M. (2003). Fluctuating particle motion during shear induced granular compaction. *Physical Review Letters, 91*(1), 014301.

Prowell, B. D., & Brown, E. R. (2007). *Superpave mix design: Verifying gyration levels in the Ndesign table*. Washington, D.C., US: Transportation Research Board.

Roque R., Birgisson B., Zhang Z., Sangpetngam B., & Grant, T. (2002). *Implementation of SHRP Indirect Tension Tester to Migrate Cracking in Asphalt Pavements and Overlays.* (University of Florida, Final Report). Gainesville, FL: Florida Department of Transportation.

Roque R., & Buttlar, W. G. (1992). The development of a measurement and analysis system to accurately determine asphalt concrete properties using the Indirect Tensile mode. *Journal of the Association of Asphalt Paving Technologists, 61*, 304–328.

Stroup-Gardiner, M., Newcomb, D., Olson, R., & Teig, J. (1997). Traffic densification of asphalt concrete pavements. *Transportation Research Record: Journal of the Transportation Research Board, 1575,* 1–9.

Tashman, L. S., Masad, E., Peterson, B., & Saleh, H. (2000). *Internal Structure Analysis of Asphalt Mixes to Improve the Simulation of Superpave Gyratory Compaction to Field Conditions.* Pullman, WA: Washington State University.

ter Huerne, H. L. (2000). Possibilities for material characterization and FEM simulation of compaction process of asphalt pavement. *Heron, 45*(3), 237–52.

ter Huerne, H. L. (2004). *Compaction of asphalt road pavements using finite elements and critical state theory* (Doctoral Dissertation). Enschede, Netherlands: University of Twente.

Trulsson, M., Andreotti, B., & Claudin, P. (2012). Transition from the Viscous to inertial regime in dense suspensions. *Physical Review Letters, 109* (11), 1–6. doi:10.1103/PhysRevLett.109.118305

Vallerga, B. A., & Lovering, W. R. (1985). Evolution of the Hveem stabilometer method of designing asphalt paving mixtures. *Association of Asphalt Paving Technologists Proc., 54*, 243-265.

Vandewalle, N., Lumay, G., Ludewig, F., & Fiscina, J. E. (2012). How relative humidity affects random packing experiments. *Physical Review E - Statistical, Nonlinear, and Soft Matter Physics, 85*(3), 1–5. doi:10.1103/PhysRevE.85.031309

Vavrik, W., & Carpenter, S. (1998). Calculating air voids at specified number of gyrations in Superpave gyratory compactor. *Transportation Research Record: Journal of the Transportation Research Board, 1630,* 117–125.

Vivar, E. del P., & Haddock, J. E. (2006). *HMA pavement performance and durability*. West Lafayette, IN: Purdue University

Von Quintus, H. L. (1991). *Asphalt-Aggregate Mixture Analysis System: AAMAS.* Washington, DC United States: Transportation Research Board.

Wang, L., Zhang, B., Wang, D., & Yue, Z. (2006). Fundamental mechanics of asphalt compaction through FEM and DEM modeling. *Analysis of Aspahlt Pavement Materials and Systems,* Geo-Denver 2007 *,* 45–63.

Wang, Z., Dai, Q., Guo, S., Wang, R., Ye, M., & Yap, Y. K. (2017). Experimental investigation of physical properties and accelerated sunlight-healing performance of flake graphite and exfoliated graphite nanoplatelet modified asphalt materials. *Construction and Building Materials, 134*, 412–23. doi:10.1016/j.conbuildmat.2016.12.129

West, R., Moore, J., Jared, D., & Wu, P. (2007). Evaluating Georgia's compaction requirements for stone matrix asphalt mixtures. *Transportation Research Record: Journal of the Transportation Research Board, 2001,* 93–101.

White, T. D. (1985). Marshall procedure for design and quality control of asphalt mixtures. *Association of Asphalt Paving Technologists Proc., 54*, 265-284.

Wisconsin Asphalt Pavement Association. (2016). *2016 Asphalt Pavement Design Guide*. Retrieved from https://doi.org/10.4324/9780203223673_chapter_16

Wisconsin Highway Research Program (WHRP). (2016). *Research Proposal: Regressing Air Voids for Balanced HMA Mix Design Study* (Project ID: 0092-16-06). Retrieved from http://wisconsindot.gov/documents2/research/flex-ffy17-rfp-air-voids.pdf

Xia, K., & Chi, L. (2008). A viscoplastic foam model for prediction of asphalt pavement compaction. *Pavements and Materials: Characterization, Modeling, and Simulation*, *67,* 136–45.

Xie, H., Watson, D., & Brown, E. (2005). Evaluation of two compaction levels for designing stone matrix asphalt. *Transportation Research Record: Journal of the Transportation Research Board, 1929,* 149–156.

Yohannes, B. & Hill, K. M. (2010). Rheology of dense granular mixtures: Particle-size distributions, boundary conditions, and collisional time scales. *Physical Review E, 82*(6), 061301.

Yu, H., & Shen, H. (2012). *An Investigation of Dynamic Modulus and Flow Number of Asphalt Mixtures in Washington State*. Washington, DC: U.S. State Department of Transportation.

Zhang W., Drescher A., & Newcomb D. E. (1997). Viscoelastic analysis of diametral compression of asphalt concrete. *Journal of Engineering Mechanics, 123*(6), 596–603.

Zofka A., Marasteanu, M., Li, X., Clyne, T., & McGraw, J. (2005). Simple method to obtain asphalt binders low temperature properties from asphalt mixtures properties. *Journal of the Association of Asphalt Paving Technologists, 80*, 255–282.